Universidade Estadual de Campinas
Instituto de Física "Gleb Wataghin"

Damaris Tartarotti Maimone

Crystal lattice vibrations and their coupling with magnetic correlations and orbital ordering in MSb_2O_6 (M = Cu, Co)

Vibrações na rede cristalina e seu acoplamento com correlações magnéticas e ordenamento orbital em MSb_2O_6 (M = Cu, Co)

Campinas
2016

Damaris Tartarotti Maimone

Crystal lattice vibrations and their coupling with magnetic correlations and orbital ordering in MSb_2O_6 (M = Cu, Co)

Vibrações na rede cristalina e seu acoplamento com correlações magnéticas e ordenamento orbital em MSb_2O_6 (M = Cu, Co)

Dissertation presented to the "Gleb Wataghin" Institute of Physics at University of Campinas in partial fulfillment of the requirements for the degree of Master in Physics.

Dissertação apresentada ao Instituto de Física "Gleb Wataghin" da Universidade Estadual de Campinas como parte dos requisitos exigidos para a obtenção do título de Mestra em Física.

Advisor/Orientador: Prof. Dr. Eduardo Granado Monteiro da Silva

ESTE EXEMPLAR CORRESPONDE À VERSÃO FINAL DA TESE DE DOUTORADO DEFENDIDA PELA ALUNA DAMARIS TARTAROTTI MAIMONE E ORIENTADA PELO PROF. DR. EDUARDO GRANADO MONTEIRO DA SILVA.

Campinas
2016

Agência(s) de fomento e nº(s) de processo(s): CNPq, 132659/2015-8

Ficha catalográfica
Universidade Estadual de Campinas
Biblioteca do Instituto de Física Gleb Wataghin
Lucimeire de Oliveira Silva da Rocha - CRB 8/9174

M284c

Maimone, Damaris Tartarotti, 1992-
Crystal lattice vibrations and their coupling with magnetic correlations and orbital ordering in MSb2O6 (M = Cu, Co) / Damaris Tartarotti Maimone. – Campinas, SP : [s.n.], 2016.

Orientador: Eduardo Granado Monteiro da Silva.
Dissertação (mestrado) – Universidade Estadual de Campinas, Instituto de Física Gleb Wataghin.

1. Sistemas de spin de baixa dimensionalidade. 2. Espectroscopia Raman. 3. Acoplamento spin-fônon. I. Silva, Eduardo Granado Monteiro da,1974-. II. Universidade Estadual de Campinas. Instituto de Física Gleb Wataghin. III. Título.

Informações para Biblioteca Digital

Título em outro idioma: Vibrações na rede cristalina e seu acoplamento com correlações magnéticas e ordenamento orbital em MSb2O6 (M = Cu, Co)
Palavras-chave em inglês:
Low dimensional spin systems
Raman spectroscopy
Spin-phonon coupling
Área de concentração: Física
Titulação: Mestra em Física
Banca examinadora:
Eduardo Granado Monteiro da Silva [Orientador]
Eduardo Miranda
Roberto Luiz Moreira
Data de defesa: 05-12-2016
Programa de Pós-Graduação: Física

MEMBROS DA COMISSÃO JULGADORA DA DISSERTAÇÃO DE MESTRADO DE **DAMARIS TARTAROTTI MAIMONE – RA: 116513** APRESENTADA E APROVADA AO INSTITUTO DE FÍSICA “GLEB WATAGHIN”, DA UNIVERSIDADE ESTADUAL DE CAMPINAS, EM 05/12/2016.

COMISSÃO JULGADORA:

- Prof. Dr. Eduardo Granado Monteiro da Silva – (Orientador) – DEQ/IFGW/UNICAMP
- Prof. Dr. Eduardo Miranda – DFMC/IFGW/UNICAMP
- Prof. Dr. Roberto Luiz Moreira – DF/UFMG

A Ata de Defesa, assinada pelos membros da Comissão Examinadora, consta no processo de vida acadêmica da aluna.

CAMPINAS
2016

"Fall in love with some activity, and do it! Nobody ever figures out what life is all about, and it doesn't matter. Explore the world. Nearly everything is really interesting if you go into it deeply enough. Work as hard and as much as you want to on the things you like to do the best. "

Richard Feynman

"There is a time for everything, and a season for every activity under the heavens:
a time to be born and a time to die,
a time to plant and a time to uproot,
a time to kill and a time to heal,
a time to tear down and a time to build,
a time to weep and a time to laugh,
a time to mourn and a time to dance,
a time to scatter stones and a time to gather them,
a time to embrace and a time to refrain from embracing "

Ecclesiastes 3, 1-5

To my forever beloved parents and family.

Acknowledgments

When I look back on my masters period, joining the GPOMS (Grupo de Propriedades Ópticas e Magnéticas dos Sólidos - Optical and magnetic properties of solids) was definitely a right decision. I would like to express my gratitude to my supervisor Eduardo Granado Monteiro da Silva for his guidance and support as well as to our collaborator John J. Neumeier who has introduced us to the field of low dimensional spin systems, by providing us high quality samples $M\mathrm{Sb_2O_6}$ (M = Cu,Co) and helpful discussions. Further, I would like to thank other professors at our group Prof. Dr. Carlos Rettori, Prof. Dr. Pascoal Pagliuso, Prof. Dr. Cris Adriano and Prof. Dr. Ricardo Urbano, for motivating and providing good infrastructure for the students to perform their research. In addition, I would like to sincerely give thanks to the technicians Celso, Zairo, Sanclair for helping with the experimental work. Additionally, thanks to the secretary staff Rose, Valeria and Emilia and to the graduate program staff (CPG) Armando, Alessandra, Luciana, Miguel and Marcos Sérgio for their very important administrative efforts.

The high quality of the samples influences the quality of the experimental work. In this sense, I would like to thank Dr. Aaron Christian for his wonderful work.

Moreover, I would like to thank Prof. Dr. Carlos Manuel Giles Antunez de Mayolo and Prof. Dr. Jose Antonio Brum for their advices and encouragement to always seek for more. Many thanks to Katharina Fristch, Katrin Meyer-Kirschner and Klaus Habicht, for giving me the wonderful opportunity of participating in the Helmholtz-Zentrum Berlin summer program in 2015.

It is also my pleasure to thank my friends for all their support. Specially, many thanks to Guilherme, Luiz Filipe, Imara, José Renato, Kelin, Jiaguo Zhang, Luis Fernando, Ludwing, Debora, Luiz Guilherme, Laís, Patricia. Moreover, thanks to my friends at our group: Ulisses, Ali, Jean, Dina, Camilo. I am sincerely thankful to my cousin Christian, who has always helped me with English and text revision.

I would like to thank the funding agency CNPq for the financial support and the students association for their grants to participate in international events.

My final thanks are devoted to my parents Celio Maimone, Elisabeth Tartarotti and my

grandmother Amelia Martins Tartarotti for which I dedicate the accomplishment of this work. I would also like to thank my family Diva, Delio, Magda, Elma, Jairo, Rosangela, Nely, Pedro, Carlos, Josue, Elena, Haroldo, Alexandre. Their full support and love are unimaginable.

I would like to express my gratitude to the mentor of everything which blesses me everyday and for who I offer this work and honor, God.

Resumo

Os antiferromagnetos de baixa dimensionalidade $CuSb_2O_6$ e $CoSb_2O_6$ foram investigados com espectroscopia Raman polarizada. Foram obtidas informações sobre as propriedades magnéticas intrigantes e configurações orbitais. Pode-se fazer a atribuição dos modos fonônicos na fase alta simetria tetragonal para ambos compostos. Para o $CuSb_2O_6$, uma transição estrutural a $T_S = 397(3)$ K manifesta-se através da observação de um novo modo fonônico em ~ 670 cm^{-1} e por uma grande anomalia na frequência do modo em ~ 640 cm^{-1} na fase de baixa simetria monoclínica, evidenciando uma hibridização aumentada das cadeias lineares de Cu-O-O-Cu como resultado de ordenamento orbital dos elétrons $3d$ do Cu abaixo de T_S. Foi observada uma pronunciada forma de linha assimétrica Fano e comportamentos anômalos para a frequência e largura de linha como função da temperatura para o modo A_{1g} em ~ 515 cm^{-1} para o composto $CuSb_2O_6$, indicando um forte acoplamento deste modo com excitações eletrônicas (possivelmente orbitais). Finalmente, ambos os compostos apresentam anomalias de frequência na maioria dos fônons abaixo de ~ 100 K que foram interpretados em termos de acoplamento spin-fônon, produzindo informações pertinentes sobre as correlações de curto alcance de baixa dimensionalidade spin-spin. Demonstrou-se, portanto, que espectroscopia Raman fonônica é uma ferramenta valiosa para investigar magnetos de baixa-dimensionalidade.

Palavras-chave: sistemas de spin de baixa dimensionalidade, espectroscopia Raman, acoplamento spin-fônon.

Abstract

The low-dimensional antiferromagnets $CuSb_2O_6$ and $CoSb_2O_6$ were investigated by polarized phonon Raman spectroscopy, providing insights into their intriguing magnetic properties and orbital configurations. An assignment of the observed phonon modes in the high-symmetry tetragonal phase was performed for both compounds. For $CuSb_2O_6$, a structural transition at $T_S = 397(3)$ K is manifested by the observation of a new phonon mode at ~ 670 cm^{-1} and by a large frequency anomaly of a mode at ~ 640 cm^{-1} in the low-symmetry monoclinic phase, evidencing an enhanced hybridization of the Cu-O-O-Cu linear chains as a result of orbital ordering of Cu $3d$ electrons below T_S. Pronounced asymmetric Fano lineshape and anomalous frequency and linewidth behavior with temperature were observed for the ~ 515 cm^{-1} A_{1g} mode for $CuSb_2O_6$, indicating a strong coupling of this mode with electronic (possibly orbital) excitations. Finally, both compounds show frequency anomalies in most phonons below $\sim$ 100 K that were interpreted in terms of the spin-phonon coupling, yielding relevant information on the low-dimensional short-range spin-spin correlations. Phonon Raman spectroscopy is therefore demonstrated to be a valuable tool to investigate low-dimensional magnets.

Keywords: Low dimensional spin systems, Raman spectroscopy, spin-phonon coupling.

List of Figures

List of Tables

List of Abbreviations

AFM	-	Antiferromagnetism
MCE	-	Magnetocaloric effect
NMR	-	Nuclear magnetic resonance
CFE	-	Crystal field effects
$\mathbf{E_F}$	-	Fermi energy
DFT	-	Density Functional Theory
LDA	-	Local Density Approximation
GGA	-	Generalized Gradient Approximation
CCD	-	Charge Coupled Device
XRD	-	X-ray diffraction
e	-	electron's fundamental charge ($1.602\ 10^{-19}\ C$)
h	-	Planck's constant ($4.135\ 10^{-15}\ eVs$)
$\hbar$	-	Plack's contant over 2π ($6.582\ 10^{-16}\ eVs$)
k_B	-	Boltzmann Constant ($8.617\ 10^{-5}\ eVK^{-1}$)
m_{el}	-	Electron mass ($9.109\ 10^{-31}\ kg$)
μ_0	-	Permeability of free space ($4\pi 10^{-7}\ Hm^{-1}$)
μ_B	-	Bohr magneton ($9.274\ 10^{-24}\ Am^2$)

Contents

Chapter 1

Introduction

In this dissertation, we have experimentally studied the low-dimensional spin systems $M\mathrm{Sb_2O_6}$ M = (Cu,Co) through a spectroscopic technique. The main motivation of this work was to broaden and deepen the understanding of the magnetic correlations and its interaction with the lattice in low-dimensional spin systems. Moreover, the compounds investigated in this work were chosen to explore the effects of quantum magnetism. In particular, we investigated the low-dimensional magnetism with a microscopic technique, capable of providing information about the magnetic correlations between first neighbors.

The structure of this dissertation is as follows. In the introduction, we will give an overview of low dimensional magnetism, coming from the early beginning until nowadays. Then, we will present the specific problem carried out in this work. In Chapter 2, the theoretical background needed for this dissertation will be discussed, starting from magnetism in solids as well as quantum magnetism and the lattice dynamics are explained. In Chapter 3, the experimental technique employed in this work will be addressed. Chapter 4 and Chapter 5 are devoted to present the scientific case, results and discussions of the measurements for the compounds $\mathrm{CuSb_2O_6}$ and $\mathrm{CoSb_2O_6}$, respectively. Finally, Chapter 6 gives a summary on general aspects that have been highlighted in this dissertation as well as the conclusions and perspectives.

1.1 Low dimensional magnetism: State of the Art

The field of low-dimensional magnetism began in 1925, when Ernst Ising followed a suggestion of his professor Lenz to investigate the one-dimensional model that is now well known under his name [1]. In 1931, Hans Bethe [2] developed his method to find the exact quantum mechanical eigenstates of the antiferromagnetic (AFM) one-dimensional version of Heisenberg's model. For the first 40 years, this field of research was completely theoretical, and scientists were

attracted by the possibility of finding new physics without having to deal with the complexity of the three-dimensional model. During this period, they succeeded in extending the 1D case to the 2D case, in calculating thermal properties of these models, and many other progresses were achieved. Since these are many body systems with high symmetry, having Hamiltonians with translational and rotational invariance[3], and their eigenstates can be determined exactly, they keep attracting the interest of theoreticians.

In the end of 1960s and in the 1970s, it became apparent that a realization of one and two dimensional systems could be obtained in 3D bulk materials[4], where the magnetic coupling is anisotropic, being much stronger in one or two directions than in the remaining ones. Furthermore, bulk materials have a great advantage over 2D surfaces because they provide sufficient intensity for experiments of thermal and dynamical properties.

Nowadays, low-dimensional spin systems can have a wide variety of applications, as in the case of nanomagnets for quantum computer devices[3]. It is then possible to notice that in approximately 90 years, since the beginning of this field of research, we have come from a completely theoretical field to possible applications.

In addition, low-dimensional magnets represent the possibility to study ground and excited states of quantum models, the interplay between quantum and thermal fluctuations as well as new phases of matter like the spin liquids, for example. These compounds exhibit a wide variety of properties as a result of the complex interplay of different interactions, mainly ligand-fields and strong correlations effects. For these reasons, a considerable amount of research has been carried out in this field and it was recently enhanced by the discovery of high-Tc superconductors in layered cuprates[5]. According to the "Resonating Valence Bond"(RVB) state proposal, low dimensionality, magnetic frustration and low-spin can favor an insulating phase in a metal-insulator phase transition, making possible the appearance of superconductivity[5].

The dimensionality of the spins and its quantum number strongly determine the nature of ground states and elementary excitations. Low dimensional systems with geometrical frustration exhibit a wide variety of peculiar phenomena such as dimerization or spin-Peierls transition[6], formation of energy-gap, degenerated ground states, and many others. Since the on-site Coulomb repulsion in these compounds is much higher than the width of the energy band, the spin dynamics is expected to be closely related to the orbital, charge and lattice dynamics[7]. These systems are often found in transition-metal oxides, such as titanates, vanadates, cuprates and Cobalt oxides. This dissertation intends to contribute to the understanding of spin correlations, orbital order and their coupling with the lattice vibrations in a specific class of compounds, investigating the $CuSb_2O_6$ and $CoSb_2O_6$ with a spectroscopic probe, namely Raman spectroscopy.

1.2 Specific Problem: $CuSb_2O_6$ and $CoSb_2O_6$

Transition metal oxides with the chemical formula MB_2O_6, where M is a $3d$ transition metal and B is either Sb or Ta, are a very interesting class of compounds which display antiferromagnetism with reduced dimensionality [8, 9, 10, 6]. Their Néel temperatures are approximately 10K, but short-range order is observed well above this temperature. Broad peaks in their magnetic susceptibilities are indicative of local ordering. Other measurements such as heat capacity and Moessbauer spectroscopy can also indicate the low-dimensional behavior. In this dissertation, we will concentrate on two compounds that belong to this class, $CuSb_2O_6$ and $CoSb_2O_6$.

$CuSb_2O_6$ was first synthesized in 1940 [11]. This compound is a green colored insulator with gap size typical for cuprates. In contrast to the vast majority of cuprates with a quasi-planar Cu four-fold coordination, it exhibits a nearly octahedral local environment of oxygens around the Cu^{2+}. This compound crystallizes in a monoclinically distorted trirutile at room temperature, β-$CuSb_2O_6$ (Fig.1.1-a), with space group $P2_1/n$. Above $\sim$ 390 K, a second order phase transition takes place to a tetragonal $\alpha-CuSb_2O_6$, with space group $P4_2/mnm$. Although it presents a phase transition, the octahedral environment around the Cu ions remains nearly unaltered. The magnetic cation M^{2+} sublattice is that of the K_2NiF_4 structure type, which includes many classic examples of square lattices exhibiting 2D AFM [5].

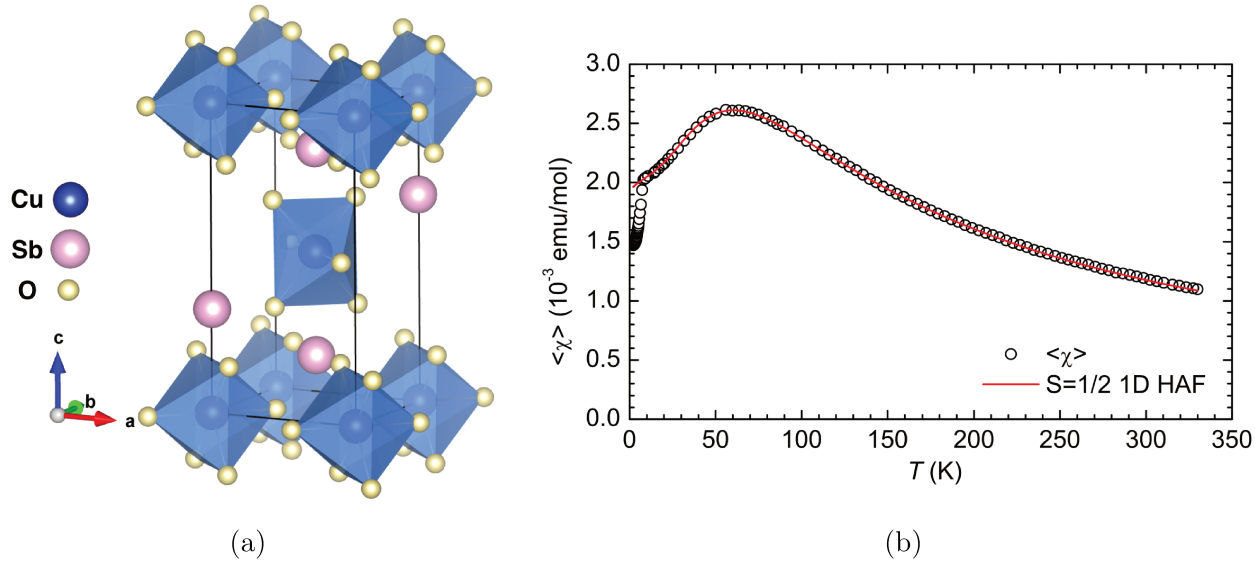

(a) (b)

Fig. 1.1: a) Crystal structure of the compound $CuSb_2O_6$ and b) its magnetic susceptibility [12] measured at 7kOe from 2K to 330K. Solid red line indicates a Bonner Fisher fit for $S = \frac{1}{2}$ Heisenberg antiferromagnet. [13]

However, magnetic susceptibility of polycrystalline $CuSb_2O_6$ can be well described considering a one-dimensional (1D) spin $S = \frac{1}{2}$ Heisenberg AFM model with $\frac{J}{k_B} = -94$ K and $\langle g \rangle = 2.11$, as shown in Fig.1.1-b). At $T_N \approx 8.5$ K, a kink in the susceptibility marks a crossover from one to three dimensional AFM behavior.

$CoSb_2O_6$ crystallizes in a tetragonal trirutile structure [14] with space group $P4_2/mnm$ (136), $a = 4.6495$Å and $c = 9.2763$Å, as shown in Fig.1.2-a). Magnetic susceptibility measurements are consistent with the two-dimensional antiferromagnetic Ising model for temperatures below ~ 80 K [14]. As shown in Fig.1.2-b), χ presents a maximum at ~ 35 K, indicating local magnetic order. It is also possible to notice a sharp drop in the magnetic susceptibility below $T_N = 13.45$ K, indicating a transition to long-range AFM order. On the other hand, anisotropic magnetocaloric measurements (MCE) seem to be more consistent with a one-dimensional magnetic behavior for this compound[15], and this is apparently the most widely accepted scenario at present. Thus, unambiguous identification of the magnetic structure associated with this compound has been challenging.

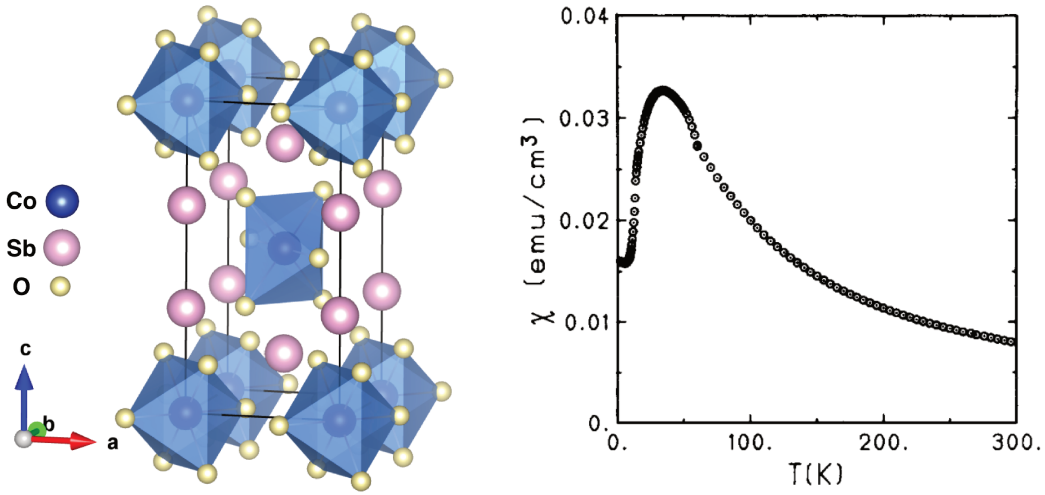

(a) (b)

Fig. 1.2: a) Crystal structure of the compound $CoSb_2O_6$ and b) its magnetic susceptibility [14] measured at 100G from 4K to 60K and at 5000G from 60K to 300K.

It is of interest to determine the consequences of the substitution of Cu per Co on the magnetic properties for the compounds MSb_2O_6. The anomalous low-dimensional behavior in the magnetic susceptibility remains an open question. In this work, we proposed to study these compounds microscopically, in order to probe the spin correlations between first neighbors and then verify the reduced dimensionality at low temperatures. A powerful tool for studying low-dimensional spin systems is Raman spectroscopy, which is sensitive to nearly all possible types

of collective excitations as well as the interplay among them.

Chapter 2

Theoretical Aspects

In this chapter, we shall give an overview of the theory used throughout this dissertation, coming from the magnetism in solids to the theoretical description of low-dimensional quantum spin systems. Moreover, this chapter is concerned with understanding the lattice dynamics of materials, and a description about ab-initio lattice dynamical calculations will be addressed as well.

2.1 Magnetism in Solids

Let us first consider the physics of isolated atoms and their interaction with an applied weak, uniform and static magnetic field ($\mathbf{B} = \nabla \times \mathbf{A}$). We can write the perturbed Hamiltonian of an atom under the application of a field as[1]:

$$\hat{\mathcal{H}} = \hat{\mathcal{H}}_0 + \mu_B(\mathbf{L} + g\mathbf{S}).\mathbf{B} + \frac{e^2}{8m_e}\sum_{i=1}^{Z}(\mathbf{B} \times \mathbf{r_i})^2 \tag{2.1}$$

where $\hat{\mathcal{H}}_0 = \sum_{i=1}^{Z}(\frac{p_i^2}{2m} + V_i)$ is the unperturbed Hamiltonian, which we assume that has known eigenstates and eigenvalues; $\mathbf{L}$ and $\mathbf{S}$ are the total angular momentum and total spin operators, respectively; $\mathbf{r_i}$ and $\mathbf{p_i}$ are the position and the momentum operators of the i^{th} electron in the atom.

The dominant perturbation to the original Hamiltonian $\hat{\mathcal{H}}_0$ is usually the second term in Eq.2.1, $\mu_B(\mathbf{L} + g\mathbf{S}).\mathbf{B}$, and it is known as the paramagnetic term. The third term is due to the diamagnetic moment.

In general, for a linear material, we define the magnetic susceptibility χ in the presence of

[1]The underlying theory is discussed in detail in ref. [16] and [17]

a magnetic field as $\chi = \frac{\mathbf{M}}{\mathbf{H}}$, where $\mathbf{M}$ is the magnetization (magnetic moment per volume), $\mathbf{H} = \mathbf{B}/\mu_0$ ($\mu_0 = 4\pi \times 10^{-7} Hm^{-1}$ is the permeability of free space), and $M = -\frac{\partial F}{\partial B}$, where F is the Helmholtz function.

Diamagnetism Consider the case of an atom with no unfilled electronic shells, so that the second term in Eq.2.1 can be ignored. Suppose $\mathbf{B}||\hat{z}$. The first order energy shift due to the diamagnetic term for a spherically symmetric atom is

$$\Delta E_0 = \frac{e^2 B^2}{12 m_e} \sum_{i=1}^{Z} \langle 0| \, r_i^2 \, |0\rangle \tag{2.2}$$

where $|0\rangle$ is the ground-state wave function. The magnetization is then

$$M = -\frac{\partial F}{\partial B} = -\frac{N}{V}\frac{\partial \Delta E_0}{\partial B} = -\frac{N e^2 B}{6 m_e V} \sum_{i=1}^{Z} \langle r_i^2 \rangle \tag{2.3}$$

which gives a magnetic susceptibility $\chi = \mu_0 M/B$ (assuming $\chi \ll 1$)

$$\chi = -\frac{N}{V}\frac{e^2 \mu_0}{6 m_e} \sum_{i=1}^{Z} \langle r_i^2 \rangle \tag{2.4}$$

known as the Larmor diamagnetic susceptibility[2]. We redefine $\sum_{i=1}^{Z} \langle r_i^2 \rangle \approx Z_{eff} r^2$, where Z_{eff} is the number of electrons in the outer shell of an ion and r is the ionic radius.

All materials show some degree of negative susceptibility (i.e., cases where the induced moment is opposite to the applied field[3]). In a classical viewpoint, an external magnetic field generates a back electromotive force, which opposes the magnetic field by Lenz's law, thus changing the magnetic dipole moment. Consequently, diamagnetism is present only when the substance is exposed to an applied magnetic field. This effect is generally weak.

Paramagnetism [4]

Now, we turn our attention to the second term of Eq.2.1, known as Zeeman term. So far, we have considered materials which contained no unpaired electrons, and thus the atoms or molecules had no magnetic moment unless a field was applied. Now, we will consider atoms that have unpaired electrons and thus have a non-zero magnetic moment. There are two distinguishable cases: if the shell has total angular momentum $J = L+S = 0$ or $J = L+S \neq 0$.

[2]It is also known as the core magnetic susceptibility.
[3]The prefix dia means across or against.
[4]The prefix para means with or along.

- **Van Vleck paramagnetism**

If J = 0, the first order perturbation theory $\langle 0|\,(\mathbf{L}+g\mathbf{S})\,|0\rangle$ is zero. Second order perturbation theory nevertheless predicts a magnetic susceptibility given by:

$$\chi = \frac{N}{V}\left(2\mu_B^2 \sum_n \frac{|\,\langle 0|\,(\mathbf{L}+g\mathbf{S})\,|n\rangle\,|^2}{E_n - E_0} - \frac{e^2\mu_0}{6m_e}\sum_i \langle r_i^2\rangle\right) \tag{2.5}$$

where the second term, already discussed, corresponds to the conventional Larmor diamagnetic susceptibility and the first term is positive (since $E_n > E_0$) and therefore favors an alignment of the magnetic moments parallel to the applied field. This term is known as the Van Vleck paramagnetic term, and it is temperature independent.

- **Curie paramagnetism**

If the shell has J $\neq$ 0, we have a non-zero first order term in the energy shift. In this case, the ground-state is (2J + 1)-fold degenerate at zero field, and we have to diagonalize a (2J + 1)-dimensional square matrix $\langle JLSJ_z|\,(\mathbf{L}+g\mathbf{S})\,|JLSJ_z'\rangle$. Wigner-Eckart theorem states that the matrix elements of any vector in the (2J + 1)-dimensional space of eigenstates of $\mathbf{J^2}$ and $\mathbf{J_z}$ with a given value of $\mathbf{J}$ are proportional to the matrix elements of $\mathbf{J}$:

$$\langle JLSJ_z|\,(\mathbf{L}+g\mathbf{S})\,|JLSJ_z'\rangle = g(JLS)\,\langle JLSJ_z|\,\mathbf{J}\,|JLSJ_z'\rangle \tag{2.6}$$

The coefficient g(JLS) does not depend on J_z, and since the matrix is already diagonal in the states of J_z, and the (2J+1)-fold degenerate ground-state is therefore split into states with definite values of J_z whose energies are uniformly separated by $g(JLS)\mu_B H$. The ground-state (2J+1) degenerate in zero field are diagonal in J, L, and S and thus one can write $(\mathbf{L}+g\mathbf{S}) = g(JLS)\mathbf{J}$. Moreover, if the splitting between the zero-field atomic ground-state multiplet and the first excited multiplet is large compared with k_BT, then only the (2J + 1) states in the ground-state will contribute appreciably to the free energy.

Second-order perturbation theory applied in the Hamiltonian (Eq.2.1), gives:

$$\Delta E_n = \mu_B\mathbf{B}.\,\langle n|\,\mathbf{L}+g\mathbf{S}\,|n\rangle + \sum_{n'\neq n}\frac{\langle n|\,\mu_B\mathbf{B}.(\mathbf{L}+g\mathbf{S})\,|n'\rangle}{E_n - E_{n'}} + \frac{e^2B^2}{12m_e}\sum_{i=1}^{Z}\langle 0|\,(r_i^2)\,|0\rangle) \tag{2.7}$$

The first term in Eq.2.7 is expressing the energy $E = -\vec{\mu}.\vec{B}$ of the interaction of the field with a magnetic moment that is proportional to the angular momentum of the ion, $\mu = -g(JLS)\mu_B\mathbf{J}$. Due to the fact that the zero-field ground-state is degenerate, it is not possible

to calculate the magnetic susceptibility by equating the free energy to the ground-state energy as we did previously for the non-degenerate shells with J = 0. Considering that only the lowest states are thermally excited with appreciable probability, it is possible to calculate the free energy in the canonical ensemble and obtain the susceptibility:

$$\chi = \frac{1}{3}\frac{N}{V}\frac{\mu_B^2 p_{eff}^2}{k_B T} = \frac{C}{T} \tag{2.8}$$

where C is a constant knows as Curie constant, $p_{eff} = g(JLS)\sqrt{J(J+1)}$ is the effective moment and g(JLS) is the Lande g-factor given by:

$$g(JLS) = \frac{3}{2} + \frac{1}{2}\frac{S(S+1) - L(L+1)}{J(J+1)} \tag{2.9}$$

The Curie's dependence of the magnetic susceptibility leads to $\chi \propto 1/T$. Room temperature paramagnetic susceptibilities are of the order of 10^{-2} to 10^{-3} and its contribution completely dominates the diamagnetic one. On the other hand, there are some conditions for the validity of the Curie's law: $k_B T \gg \hbar\mu_B B$; the magnetic interaction between ions cannot be appreciable; the J multiplet lying above the ground-state can not be close in energy. Indeed, the rare-earth's magnetism in an insulating solid are well described by treating them as isolated atoms, as one can notice from Table 2.1.

Ion	Shell	S	L	J	Term	Calculated p	p_{exp}
Ce^{3+}	$4f^1$	1/2	3	5/2	$^2F_{5/2}$	2.54	2.51
Pr^{3+}	$4f^2$	1	5	4	$^3H_4$	3.58	3.56
Nd^{3+}	$4f^3$	3/2	6	9/2	$^4I_{9/2}$	3.62	3.3-3.7
Pm^{3+}	$4f^4$	2	6	4	$^5I_4$	2.68	-
Sm^{3+}	$4f^5$	5/2	5	5/2	$^6I_{5/2}$	0.85	1.74
Eu^{3+}	$4f^6$	3	3	0	$^7F_0$	0.0	3.4
Gd^{3+}	$4f^7$	7/2	0	7/2	$^8S_{7/2}$	7.94	7.98
Tb^{3+}	$4f^8$	3	3	6	$^7F_6$	9.72	9.77
Dy^{3+}	$4f^9$	5/2	5	15/2	$^6H_{15/2}$	10.63	10.63
Ho^{3+}	$4f^{10}$	2	6	8	$^5I_8$	10.60	10.4
Er^{3+}	$4f^{11}$	3/2	6	15/2	$^4I_{15/2}$	9.59	9.5
Tm^{3+}	$4f^{12}$	1	5	6	$^3H_6$	7.57	7.61
Yb^{3+}	$4f^{13}$	1/2	3	7/2	$^2F_{7/2}$	4.53	4.5
Lu^{3+}	$4f^{14}$	0	0	0	$^1S_0$	0.0	0.0

Tab. 2.1: The value of the effective moment obtained by the measured magnetic susceptibility (Eq.2.8) compared with the calculated one $p = p_{eff}/\mu_B = g_J\sqrt{J(J+1)}$ using Hund's rules predictions.

In contrast, this is not the case for the transition metal ions. For these ions, although the Curie Weiss' law works fine, the value of the effective moment p_{eff} given by Eq.2.8 is not correct. To obtain the correct value, one has to assume that although S is still given by Hund's law, the value of L must be 0, and hence J = S. This effect is known as the *quenching of the orbital angular moment*. Table 2.2 demonstrates a much better degree of agreement when considering the orbital quenching. This is a consequence of the fact that in these materials, the crystal field effects, which will be discussed in the next section, are much higher than the spin-orbit coupling. This is due to the fact that spin-orbit coupling is proportional to $\propto Z^4$ and therefore they are enhanced in the rare-earths, and additionally, their orbitals are much less extended away from the nucleus so that the crystal field effects are much less important than Hund's third rule.

Ion	Shell	S	L	J	Term	Calculated p_1	p_{exp}	Calculated p_2
Ti^{3+}, Va^{4+}	$3d^1$	1/2	2	3/2	$^2D_{3/2}$	1.55	1.70	1.73
V^{3+}	$3d^2$	1	3	2	$^3F_2$	1.63	2.61	2.83
Cr^{3+}, Va^{2+}	$3d^3$	3/2	3	3/2	$^4F_{3/2}$	0.77	3.85	3.87
Mn^{3+}, Cr^{2+}	$3d^4$	2	2	0	$^5D_0$	0	4.82	4.9
Fe^{3+} , Mn^{2+}	$3d^5$	5/2	0	5/2	$^6S_{5/2}$	5.92	5.82	5.92
Fe^{2+}	$3d^6$	2	2	4	$^5D_4$	6.7	5.36	4.9
Co^{2+}	$3d^7$	3/2	3	9/2	$^4F_{9/2}$	6.63	4.9	3.87
Ni^{2+}	$3d^8$	1	3	4	$^3F_4$	5.59	3.12	2.83
Cu^{2+}	$3d^9$	1/2	2	5/2	$^2D_{5/2}$	3.55	1.83	1.73
Zn^{2+}	$3d^{10}$	0	0	0	$^1S_0$	0	0	0

Tab. 2.2: Magnetic ground-state for transition metal 3d ions, demonstrating that the value of the effective moment calculated by Hund's prediction (p_1) does not agree with the experimental value. Better results are obtained assuming orbital quenching, p_2.

2.1.1 Crystal Field effects

So far, we have deduced many magnetic properties without considering interactions between atoms. Now, we will take into account the interactions between an atom and its environment, considering a direct magnetic interaction between an atom in a crystal and its neighboring atoms.

In order to understand the effect of the local environment due to the crystal on the energy levels of an atom, let us first review the shapes of the s, p and d atomic orbitals, which are the most important for this work. The angular dependences of the electron density of the atomic orbitals are shown in Fig. 2.1.

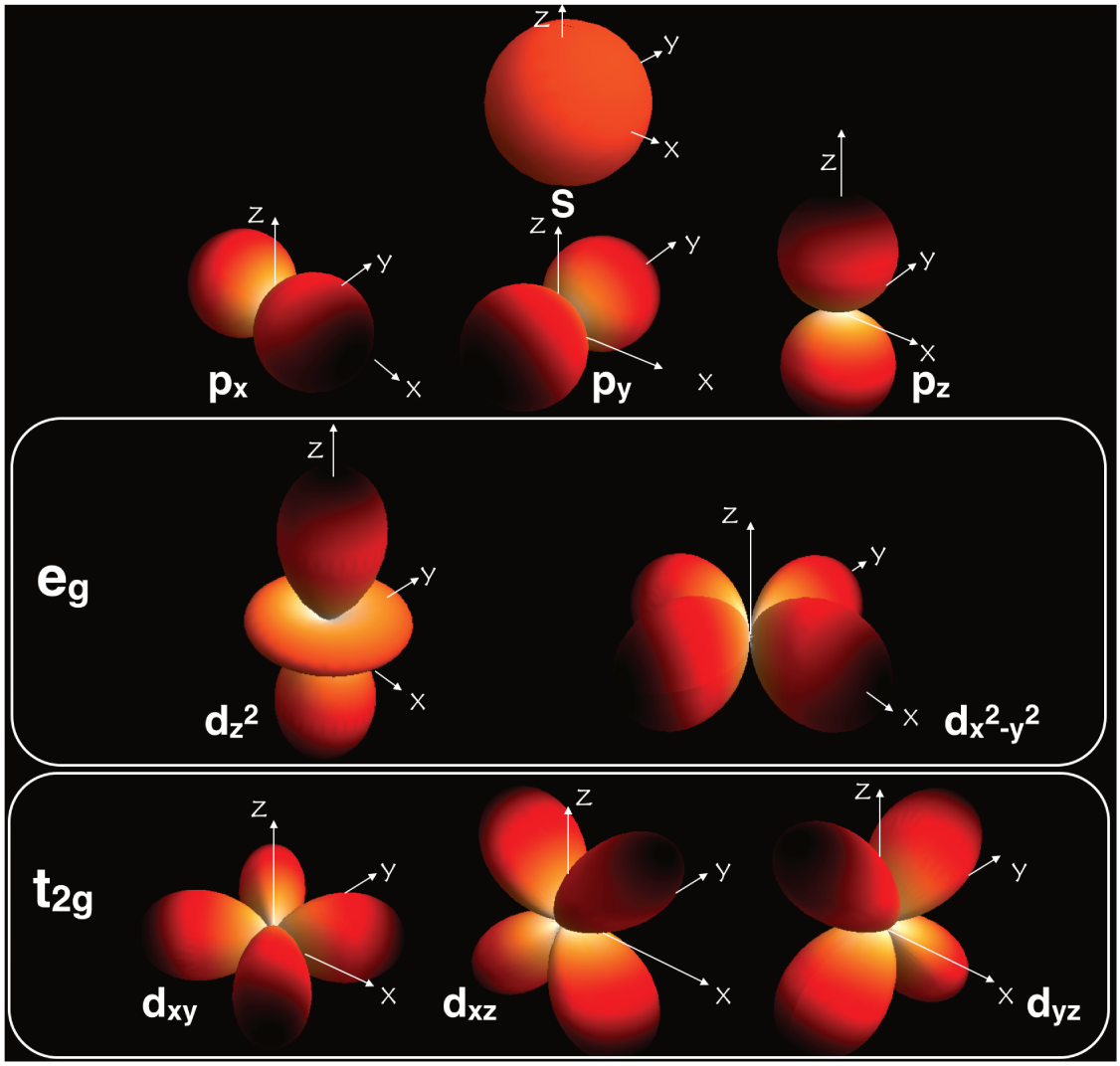

Fig. 2.1: Angular distribution of the electron density of the s, p and d orbitals. The d orbitals are divided into two classes: d_{z^2} (or often referred to as $d_{3z^2-r^2}$) and $d_{x^2-y^2}$ orbitals are called the e_g level, and the d_{xy}, d_{xz} and d_{yz} are grouped in the t_{2g} level.[18]

The crystal field is an electric field coming from the neighboring atoms in the lattice, and its effects depend crucially on the symmetry of the local environment. Two common cases that occur in nature are the octahedral and tetrahedral environments, where a metal sits in the center of the polygon with atoms such as oxygen in its corners. Diagrams of these local environments are shown in Fig.2.2.

The d-orbitals are divided into two classes: the e_g orbitals, which point along the x, y and z axes and the t_{2g} orbitals, which point in a direction in between these axes. One can understand the effect of the local environment in the orbitals by referring to Fig.2.3. This Figure shows a projection of the $xy-plane$ of the octahedral environment. In the center, there are the d

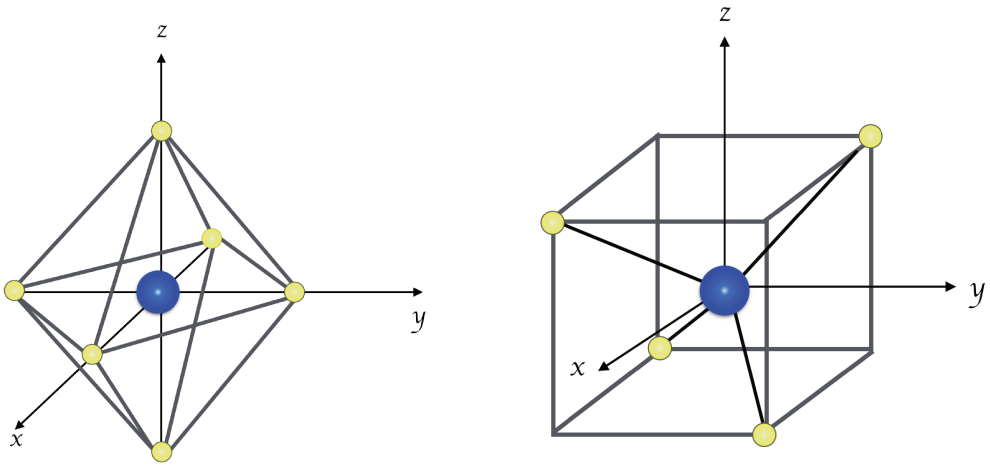

(a) (b)

Fig. 2.2: a- Octahedral and b- tetrahedral environments. A metal sits in the center of the polygon, and an atom such as oxygen sits in each corner. The octahedral environment is very common for many transition metal oxides, such as the ones studied in this work.

orbitals (Fig.2.3 a- shows a d_{xy} orbital, which belongs to the t_{2g} class, and Fig.2.3 b- shows a $d_{x^2-y^2}$ orbital, which belongs to the e_g class). In the corners, there are the oxygen's p orbital.

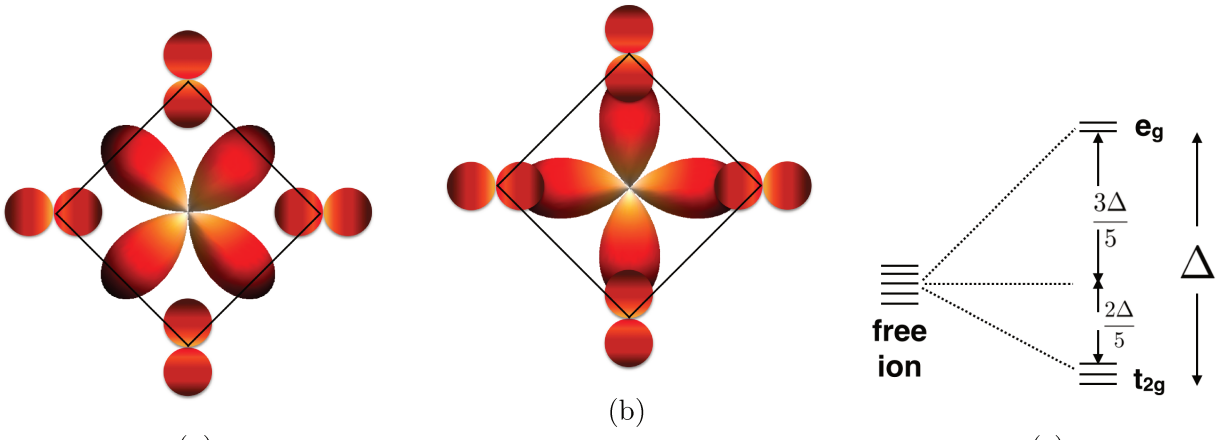

(a) (b) (c)

Fig. 2.3: The crystal field effect represented in a projection of the xy-plane of an octahedron. a- The t_{2g} orbital is lowered in energy compared to the b- e_g orbital, due to an electrostatic interaction. Therefore, the e_g and t_{2g} orbitals split in energy c-.

The crystal field effect is largely produced by the p orbitals on the neighboring atoms. It is possible to notice that there's a higher overlap between the $d_{x^2-y^2}$ and the neighboring p

orbitals than the d_{xy} orbital, and hence, there is a higher electrostatic energy. In this type of environment, it is possible to notice that all the orbitals which point along the axes will be enhanced in energy. Therefore, the five d orbitals will split, as shown in Fig.2.3-c). If the local environment was tetrahedral, the opposite would occur, and the e_g orbitals would be lowered in energy, while the t_{2g} orbitals would be raised.

To fill the d shell of a transition metal ion, one has to start filling the lowest levels before filling the highest ones. Nevertheless, the precise order to fill the shells will depend on the competition between the crystal field energy and the cost of putting two electrons in the same orbital, i.e. the pairing energy. If the crystal field is lower than the pairing energy, the electrons will tend to singly occupy each orbital - weak field case (high-spin). If, instead, the crystal field is higher than the the pairing energy, than the electrons will tend to first occupy each orbital before filling the enhanced orbitals - high field case (low-spin). As an example, let's consider the Co^{2+} ions.

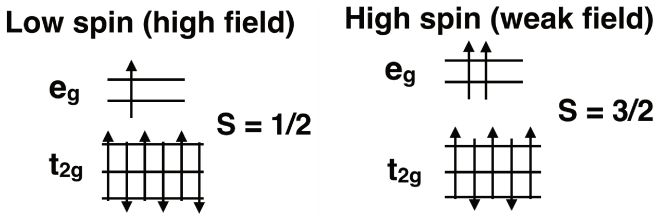

Fig. 2.4: Electronic configurations for the Co^{2+} ions in the a- low spin and b- high spin cases.

The Co^{2+} has a $3d^7$ shell. In the strong field case, six electrons are filling the t_{2g} orbitals, and there's one electron lying unpaired in the e_g orbital. Hence, the system has a S = 1/2 state. In the weak field case, one has to fill each orbital once, filling the highest energy levels. Therefore, this order leads to three unpaired electrons, two lying in the e_g orbital and one lying in the t_{2g} orbital - the system has S = 3/2. For the Cu^{2+} ion, both high spin and low spin cases lead to one single unpaired electron lying in the e_g orbital, and then S = 1/2.

Jahn-Teller Effect So far, all we have done was to work out the symmetry of the local environment and deduce the effects on the electronic structure and therefore understand the magnetic properties. However, sometimes, the opposite way around is also important, i.e. the magnetic properties can have its influence on the symmetry of the local environment as well. Sometimes it is energetically favorable for an octahedron to distort in order to save electronic energy. This phenomena is known as Jahn-Teller effect[19], and for instance, we will consider the simplest static case. Fig.2.5 shows a pictorial view of this effect for Cu^{2+}.

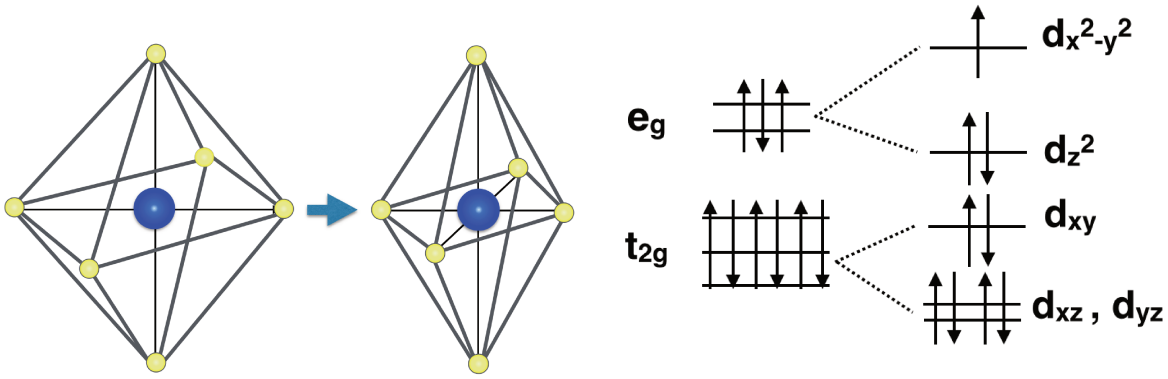

(a) (b)

Fig. 2.5: Static Jahn-Teller effect for Cu^{2+} ion ($3d^9$).a) An octahedron can spontaneously distort, b) thus splitting the t_{2g} and e_g orbitals.

The $3d^9$ electronic configuration of this ion gives three electrons in the two degenerate e_g orbitals, as explained above. This leads to a doubly degenerate electronic ground-state. Such environments distort along the z axis, which has the effect of removing the orbital and electronic degeneracies and lowering the overall energy, as shown in Fig.2.5. The distortion normally takes the form of elongating the bonds to the ligands lying along the z axis, but it occasionally occurs as a shortening of these bonds instead. When such an elongation occurs, the effect is to lower the electrostatic repulsion between the electronic density in orbitals with a z component, thus lowering the energy of the system.

2.1.2 Magnetic Interactions

There are many different types of magnetic interactions that can allow the magnetic moments in a solid to communicate.

Magnetic Dipolar Interaction

The first expected interaction is the direct dipolar interaction energy of two magnetic dipoles μ_1 and μ_2 separated by a distance $\mathbf{r}$:

$$E = \frac{1}{r^3}[\mu_1.\mu_2 - 3(\mu_1.\hat{\mathbf{r}})(\mu_2.\hat{\mathbf{r}})] \tag{2.10}$$

We can estimate the order of magnitude of this effect for two moments each of $\mu \approx g\mu_B$ separated by 1 Å to be E $\sim 10^{-4}$ eV, equivalent to 1 K, and hence this interaction is too weak to account for ordering in most magnetic materials which order at higher temperatures.

Exchange Interaction

The electrostatic energy differences between atomic states are typically of the order of sub eV, and therefore they play an important role in the magnetism. Exchange interactions are electrostatic interactions. For instance, let us first consider a simple model of two electrons. The effective Hamiltonian is:

$$\hat{\mathcal{H}}_{1,2}^{spin} = -2J\mathbf{S_1}.\mathbf{S_2}, J = \frac{E_s - E_t}{2} \tag{2.11}$$

where s and t stands for singlet and triplet, respectively; J is the exchange constant. If $J > 0$, then $E_s > E_t$ and the triplet state S = 1 is favored (spins are oriented parallel). If, instead, $J < 0$, $E_s < E_t$ and the singlet state S = 0 is favored (spins are antiparallel). There exists many types of exchange interactions:

- Direct exchange arises from the interaction of electrons on neighboring magnetic atoms, occuring without the need for an intermediary. In many cases, direct exchange does not play an important role on the observed magnetic properties, because there is no sufficient overlap between neighboring electron densities.

- Superexchange occurs when the interaction between magnetic ions occurs via a non-magnetic ion which is placed in between them. This type of interaction favors antiferromagnetic order.

- Ruderman, Kittel, Kasuya and Yosida (RKKY) or itinerant is an indirect exchange between magnetic ions which is mediated by conduction electrons in metals.

- Double exchange occurs in metals which shows mixed valency. This type of interaction favors ferromagnetic order.

- Dzyaloshinsky-Moriya is an anisotropic interaction where the spin-orbit coupling couples an excited state of one ion with the ground-state of another ion.

2.1.3 Antiferromagnetic order

Different types of magnetic ground-states can be produced by the interactions presented previously, including ferromagnets, where all the spins are aligned in parallel, and antiferromagnets, where all the spins are antiparallel and many others. Here we will concentrate on the antiferromagnetic order, which is the most relevant one for this work.

Eq.2.11 describes the spin Hamiltonian of a two-spins system. However, real systems are usually many-body systems, and inspired by this Hamiltonian, we generalize that interactions

similar to Eq.2.11 apply for all neighboring atoms and hence we write the Heisenberg Hamiltonian [5]:

$$\hat{\mathcal{H}}^{spin} = -\sum_{ij} J_{ij}\mathbf{S_i}.\mathbf{S_j} \tag{2.12}$$

where J_{ij} is the exchange constant between spin in the i^{th} and j^{th} sites (the factor of 2 is not present to avoid double counting). As stated previously, $J > 0$ favors the parallel alignment of the spins, i.e. ferromagnetism and $J < 0$ favors an antiparallel alignment of the magnetic moments, i.e. antiferromagnetism. Often, these systems can be considered as two interpenetrating sublattices, one in which the magnetic moments point up, and the other one where the magnetic moments point down, as shown in Fig.2.6.

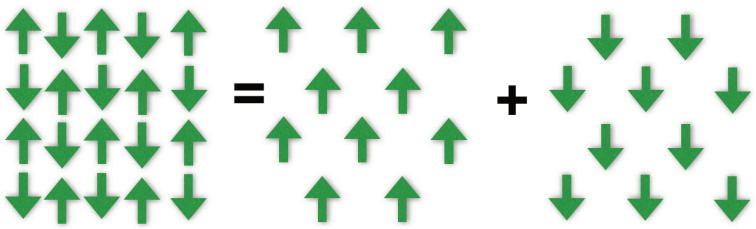

Fig. 2.6: Two interpenetrating sublattices that form an antiferromagnet.

An earliest attempt to describe antiferromagnetic systems was worked out by P. Weiss and it is known as molecular field theory. Although there are more sophisticated calculations nowadays, the molecular field provides a good starting point to perform corrections to the Curie law. The molecular field on each sublattice is given by:

$$\begin{aligned} B_+ &= -|\lambda|M_- \\ B_- &= -|\lambda|M_+ \end{aligned} \tag{2.13}$$

where λ is the molecular field constant and it parametrizes the strength of the molecular field dependence with magnetization. For an antiferromagnet, $\lambda < 0$. Considering the sublattices to be equivalent, i.e. $|M_+| = |M_-| \equiv M$, one can obtain the magnetization value:

$$M = M_S B_J\Big(\frac{g_J \mu_B J|\lambda|M}{k_B T}\Big) \tag{2.14}$$

where M_S is the saturated magnetization and B_J is the molecular field. The transition

[5]The Heisenberg Hamiltonian can be derived from the Hubbard model. We will treat it the next section.

temperature, often called the Neel temperature T_N, is given by:

$$T_N = \frac{g_J \mu_B (J+1)|\lambda| M_S}{3 k_B T} \tag{2.15}$$

For temperatures above T_N, the effect of a weak applied magnetic field can be calculated and the result yields to:

$$\chi = \lim_{B \to 0} \frac{\mu_0 M}{B} \propto \frac{1}{T + T_N} \propto \frac{1}{T - \theta} \tag{2.16}$$

which is known as the Curie-Weiss law. The sign of θ defines if the material is a paramagnet, a ferromagnet or an antiferromagnet. A summary for the magnetic susceptibilities for a paramagnet, a ferromagnet and an antiferromagnet is shown in Fig.2.7.

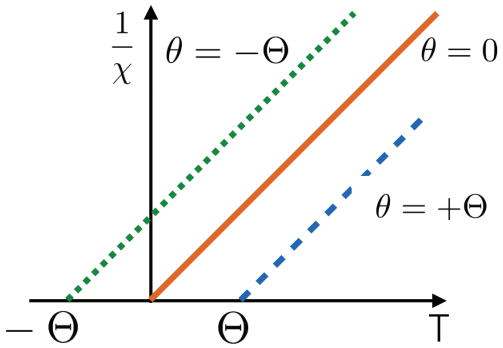

Fig. 2.7: Curie Weiss law for three cases: $\theta = 0$ for a paramagnet, $\theta = T_C$ for a ferromagnet and $\theta = -T_N$ for an antiferromagnet.

2.1.4 Hubbard and Heisenberg models

From 1963 to 1967, the physicist John Hubbard presented a simplified model to treat electrons from the d and f bands of transition metal ions and rare-earths[20, 21, 22, 23, 24, 25]. These bands are less extended away from the nucleus than the s and p bands. Thus, electrons are more strongly bound to the ions and further, the electron-electron interaction plays an important role. Therefore, the free electron model does not provide a proper description for the d and f bands. Let us consider a lattice of N sites, where there are N_e electrons which are feeling the crystal lattice potential and a Coulomb interaction. Let us consider a static lattice, and take into account the electronic degrees of freedom[6].

The Hamiltonian which describes this system is given by:

[6]This is the Born-Oppenheimer approximation[26], which decouples the ionic dynamics from the electron dynamics by stating that the ions are much heavier than the electrons.

$$\hat{\mathcal{H}} = \sum_{i=1}^{N_e} \Big(\frac{\vec{P_i}^2}{2m} + V(\vec{r_i}) \Big) + \frac{1}{2} \sum_{\substack{i,j=1 \\ j \neq i}}^{N_e} U(\vec{r_i}, \vec{r_j}) \tag{2.17}$$

where $\vec{P_i}^2/2m$ is the kinetic energy of each electron, $V(\vec{r})$ is the periodic lattice potential and $U(\vec{r}, \vec{r'}) = \frac{e^2}{|\vec{r} - \vec{r'}|}$ is the Coulomb repulsion potential. This Hamiltonian takes the following second quantized form:

$$\hat{\mathcal{H}} = \sum_{\sigma=\uparrow,\downarrow} \int d^3r \hat{\Psi}^\dagger_\sigma(\vec{r}) \Big[\frac{\vec{P}^2}{2m} + V(\vec{r}) \Big] \hat{\Psi}_\sigma(\vec{r}) + \frac{1}{2} \sum_{\sigma,\sigma'=\uparrow,\downarrow} \iint d^3r d^3r' \hat{\Psi}^\dagger_\sigma(\vec{r}) \hat{\Psi}^\dagger_{\sigma'}(\vec{r'}) U(\vec{r}, \vec{r'}) \hat{\Psi}_{\sigma'}(\vec{r'}) \hat{\Psi}_\sigma(\vec{r}) \tag{2.18}$$

where $\hat{\Psi}^\dagger_\sigma(\vec{r})$ and $\hat{\Psi}_\sigma(\vec{r})$ are the field operators which create and annihilate an electron with spin σ at the positions $\vec{r}, \vec{r'}$. The fields operators are written in terms of the Wannier function[7], $\Phi_\alpha(\vec{r} - \vec{R_j})$:

$$\hat{\Psi}^\dagger_\sigma(\vec{r}) = \sum_{j=1}^{N} \sum_{\alpha} \Phi^*_\alpha(\vec{r} - \vec{R_j}) c^\dagger_{\alpha j,\sigma} \tag{2.19}$$

where α is the band index, $\vec{R_j}$ is the j^{th} site's position vector and $c^\dagger_{\alpha j,\sigma}$ is the operator which creates an electron with spin σ at the site j and band α. The operator $c_{\alpha,j,\sigma}$ satisfies the Fermions commutation relations. Substituting Eq.2.19 in the Hamiltonian described by Eq.2.18, one can obtain:

$$\hat{\mathcal{H}} = \sum_{i,j=1}^{N} \sum_{\alpha,\sigma} t^\alpha_{ij} c^\dagger_{\alpha i,\sigma} c_{\alpha j,\sigma} + \frac{1}{2} \sum_{\alpha,\beta,\gamma,\delta} \sum_{i,j,k,l} \sum_{\sigma,\sigma'} U^{\alpha\beta\gamma\delta}_{ijkl} c^\dagger_{\alpha i,\sigma} c^\dagger_{\beta j,\sigma'} c_{\gamma k,\sigma'} c_{\delta l,\sigma} \tag{2.20}$$

where

$$t^\alpha_{ij} = \int d^3r \Phi^*_\alpha(\vec{r} - \vec{R_i}) \Big[\frac{\vec{P}^2}{2m} + V(\vec{r}) \Big] \Phi_\alpha(\vec{r} - \vec{R_j}) \tag{2.21}$$

is the hopping integral and represents the Tight Binding part of the Hamiltonian. This term means that the electrons can hop/tunnel between the sites in the lattice: if t^α_{ij} is very large, the tunneling probability is very high. The second term in Eq.2.20 represents the

[7]Deeper insight on Wannier function can be found in reference [17]

$$U_{ijkl}^{\alpha\beta\gamma\delta} = \iint d^3r d^3r' \Phi_\alpha^*(\vec{r} - \vec{R_i}) \Phi_\beta^*(\vec{r'} - \vec{R_j}) \frac{e^2}{|\vec{r} - \vec{r'}|} \Phi_\gamma(\vec{r'} - \vec{R_k}) \Phi_\delta(\vec{r} - \vec{R_l}) \tag{2.22}$$

which is known as the Coulomb integral. Let us make some approximations:

- We will consider a non-degenerate orbital per site, for simplicity. Then, we can neglect the bands indexes α, β, γ and δ;
- We will assume that the density of probability of finding electrons at a certain position is higher around the sites. This approximation is great for the d and f bands, and this means that the hopping integrals are significative for first nearest neighbors ($t_{ij} = -t$ for first neighbors and $t_{ij} = 0$ otherwise);
- We will simplify inserting only an intra-site electrons repulsion, i.e. the dominant term in the Coulomb integrals is the one where $i = j = k = l$ and the others can be neglected.

In this way, the Hamiltonian takes the form:

$$\hat{\mathcal{H}} = -t \sum_{i=1}^{N} \sum_{\vec{\delta}} \sum_{\sigma} c_{i\sigma}^\dagger c_{i+\vec{\delta}\sigma} + \frac{U}{2} \sum_{j=1}^{N} \sum_{\sigma,\sigma'} c_{j\sigma}^\dagger c_{j\sigma'}^\dagger c_{j\sigma'} c_{j\sigma} \tag{2.23}$$

and by using the Fermionic commutation relations, one arrive at a Hamiltonian:

$$\hat{\mathcal{H}} = -t \sum_{i=1}^{N} \sum_{\vec{\delta}} \sum_{\sigma=\uparrow,\downarrow} c_{i\sigma}^\dagger c_{i+\vec{\delta}\sigma} + U \sum_{i=1}^{N} \hat{n_{i\uparrow}} \hat{n_{i\downarrow}} = \hat{\mathcal{H}}_0 + \hat{\mathcal{H}}_1 \tag{2.24}$$

known as the Hubbard Hamiltonian. The vectors $\vec{\delta}$ connect neighboring sites. For a one-dimensional system, we have:

$$\hat{\mathcal{H}} = -t \sum_{i=1}^{N} \sum_{\sigma=\uparrow,\downarrow} (c_{i\sigma}^\dagger c_{(i+1)\sigma} + h.c.) + U \sum_{i=1}^{N} \hat{n}_{i\uparrow} \hat{n}_{i\downarrow} \tag{2.25}$$

where h.c. denotes the Hermitian conjugate of the previous term. Let us analyze some limits of this model:

- Non-interacting (U = 0): we discussed it corresponds to a Tight Binding band. If the number of electrons is less than two times the number of sites, the band is half filled and this is a metallic system.

- If the interactions are so high that $\frac{U}{t} \to \infty$, then $\hat{\mathcal{H}} = \hat{\mathcal{H}}_1$, double occupied sites are forbidden and the only possibilities are empty or single occupied sites. Moreover, if the number of electrons is equal to the number of sites, i.e., there are only single occupied sites, then since the repulsion approaches infinity, electrons can not move in the lattice, and the system is therefore an insulating;

- For single occupied systems, if $\frac{t}{U} \to \infty$, the system is metallic.

For a spin-$\frac{1}{2}$ system, there are 2^{N_e} possible states, which accounts for different spins configuration. If we consider strong U, this degeneration is broken by the hopping term, which can be calculated to second order perturbation theory:

$$H^{(2)}_{\alpha\beta} = \sum_n \frac{\langle\alpha| H_0 |n\rangle \langle n| H_0 |\beta\rangle}{E_0 - E_n} \tag{2.26}$$

where α and β represent any states. The n states are generated by the application of the hopping hamiltonian in the $|\sigma_i..\sigma_N\rangle$ single occupied subspace, and therefore they correspond to the annihilation of an electron at one site and creation in the neighboring site. The E_N energy is U and $E_0 = 0$. Therefore:

$$H^{(2)}_{\alpha\beta} = -\frac{1}{U} \sum_n \langle\alpha| H_0 |n\rangle \langle n| H_0 |\beta\rangle \tag{2.27}$$

The summation can now be extended to all the Hilbert space $|m\rangle$, since for all the non double occupied states, the matrix element $\langle m| H_0 |\beta\rangle = 0$.

$$\begin{aligned} H_{\alpha\beta} &= -\frac{1}{U} \sum_m \langle\alpha| H_0 |m\rangle \langle m| H_0 |\beta\rangle \\ &= -\frac{1}{U} \sum_m \langle\alpha| H_0^2 |m\rangle \end{aligned} \tag{2.28}$$

Thus, let's calculate H_0^2:

$$H_0^2 = t^2 \sum_{\substack{i\delta\sigma \\ j\delta\sigma'}} (c^\dagger_{i\sigma} c_{i+\delta,\sigma} + c^\dagger_{i+\delta,\sigma} c_{i\sigma})(c^\dagger_{j\sigma'} c_{j+\rho,\sigma'} + c^\dagger_{j+\rho,\sigma'} c_{j\sigma'}) \tag{2.29}$$

There will be terms: $c^\dagger_{i\sigma} c_{i+\delta,\sigma} c^\dagger_{j\sigma'} c_{j+\rho,\sigma'}$. These terms will not vanish in the single occupied state only if:

$$\begin{cases} i = j + \vec{\rho} \\ i + \vec{\delta} = j \end{cases} \tag{2.30}$$

Then, by performing some calculations, one can realize that:

$$H^{(2)} = \frac{4t^2}{U} \sum_{<ij>} \vec{S}_i.\vec{S}_j = -\sum_{<ij>} J\vec{S}_i.\vec{S}_j \tag{2.31}$$

where $S_i = \frac{1}{2}\sum_{\alpha\beta} c^{\dagger}_{i\alpha}\vec{\sigma}_{\alpha\beta}c_{i\beta}$. One can notice that this is the Heisenberg Hamiltonian (Eq.2.12), with

$$J = -\frac{4t^2}{U} \tag{2.32}$$

If $J < 0$, the system tends to antiferromagnetic order, and this indicates that the semi-filled Hubbard model tends to this type of order[27].

In the next section, we shall give an overview of low-dimensional quantum spin systems, since it is the case of the materials studied in this dissertation and study Eq.2.25 in greater detail.

2.2 Low-Dimensional Quantum Magnetism

There are no experimental realization of exact low-dimensional magnetic materials. In practical cases, however, a theoretical description of ideal systems provides a good starting point to understand experimental results of quasi one-dimensional magnets. Before presenting a theoretical description of a 1D antiferromagnetic system, let us introduce the Mermin-Wagner–Berenzski theorem[28]:

"An infinite d dimensional lattice of localized spins cannot have long-range order (LRO) at any finite temperature for $d < 3$ if the effective exchange interactions are isotropic and of finite range ".

In order to understand the coverage of this theorem, we will make several annotations:

- Even in the isotropic Heisenberg model, low-dimensional ferromagnets exhibit LRO at T = 0, but antiferromagnets do not;
- When the interactions are of infinite range, for example, the dipolar interaction discussed above, it is possible to find a critical temperature even in low-dimensionality;
- Anisotropic interactions can lead to LRO at finite temperatures;
- Square and hexagonal lattices present a ground-state with LRO for $S \geq 1$[29, 30];
- There is a ground-state with LRO for Heisenberg 3D for spin $\geq \frac{1}{2}$. [31]

2.2.1 One-Dimensional Magnetism

As pointed out in the first chapter, in this dissertation we will study the spin-$\frac{1}{2}$ chain $CuSb_2O_6$, and therefore we will concentrate our analysis on this magnetic ground-state.

Spin-$\frac{1}{2}$ chain

Let us consider a 1D spin-$\frac{1}{2}$ chain. On each site, there is a spin $S_i = \sigma_i/2$ where σ_i are the Pauli matrices. The three spin components obey the commutation relations:

$$[S^\alpha, S^\beta] = i\epsilon_{\alpha\beta\gamma}S^\gamma \tag{2.33}$$

where $\epsilon_{\alpha\beta\gamma}$ is the totally anti-symmetric tensor. The spins operators in different sites should commute. Assuming that the spins interact only with their first neighbors described by the Hamiltonian[8]:

$$H = \sum_i J_{xy}(S^x_{i+1}S^x_i + S^y_{i+1}S^y_i) + J_z S^z_{i+1}S^z_i \tag{2.34}$$

In this Hamiltonian, we have kept the rotation in the xy-plane, and chosen different exchange couplings for the xy-plane and the z direction. This model is known as XXZ Hamiltonian. If $J_z = J_{xy}$ the interactions between spins is invariant by rotation and this is the Heisenberg Hamiltonian. If J is positive, the energy is going to be minimum when neighboring spins point in opposite directions, i.e., $J > 0$ favors antiferromagnetic order, as pointed out before. $J < 0$ favor ferromagnetic ordering of the spins. Working with spin operators is complicated because of their commutation relations. Nevertheless, there are some mappings which are useful to treat spin problems. In the first one, we can relate the creation and annihilation spin operators to bosonic operators[21]: $S^+ \to b^\dagger$ e $S^- \to b$. In order to have the right commutation relation, the spin operator S^z must be the bosonic density: $S^z = b^\dagger b - \frac{1}{2}$. In this way, spins on different sites commute, as it should be. However, the Fock space in one site is extremely large for bosons, since the third commutation relation for bosons allows an arbitrary large number of bosons.

[8] Deeper insight can be found in ref [32]

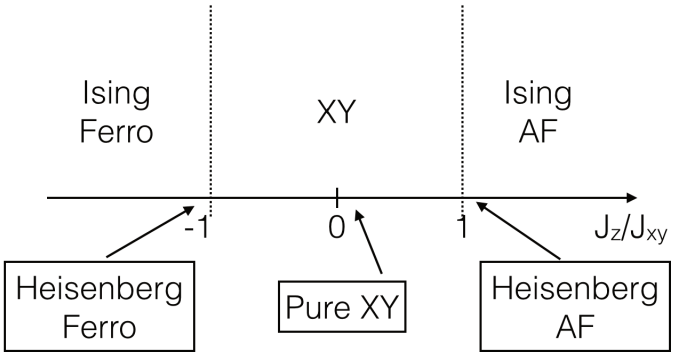

Fig. 2.8: Regimes for a spin-$\frac{1}{2}$ chain as a function of $\frac{J_z}{J_{xy}}$.

To restrict the Fock space to only two allowed states for spins-$\frac{1}{2}$, we must introduce one constraint, stating that more than one boson in the same site is forbidden. This view of the problem is known as "hard core boson". This constraint introduces a complication to this problem, and in oder to get rid of this hard core constraint, it would be convenient to use Pauli principle to enforce the lowering of the Fock space and then use another mapping which is known as spinless Fermions. Thereby, if we use: $S^+ \rightarrow c^\dagger$ e $S^z = c^\dagger c - \frac{1}{2}$, where c are fermions, the commutation relation in each site are obeyed. Unfortunately, this is not so simple. In fact, if we consider different sites, the spins should behave as bosons, not fermions, because they should commute, not anti-commute. Thus we have to introduce phase factors, so that the spins on different sites commute, without changing the local commutation relations in each site. The solution to this is known as Jordan-Wigner transformation[22]. The mapping is therefore: $S_i^+ \rightarrow c_i^\dagger e^{i\pi \sum_{j=-\infty}^{i-1} c_j^\dagger c_j}$ e $S^z = c_i^\dagger c_i - \frac{1}{2}$. The XXZ Hamiltonian is then:

$$H = \frac{J_{xy}}{2} \sum_i [c_{i+1}^\dagger c_i + h.c.] + J_z \sum_i (c_{i+1}^\dagger c_i - 1/2) \tag{2.35}$$

Shifting the Fermions momentum by π, the Hamiltonian gets:

$$H = -t \sum_i [c_{i+1}^\dagger c_i + h.c.] + V \sum_i (c_{i+1}^\dagger c_i - 1/2) \tag{2.36}$$

This is an itinerant fermions model, where the first term is the kinetic energy (Tight Binding Hamiltonian model -TBM), that states that Fermions can hop between neighboring sites with a matrix element t. These Fermions also suffer a nearest neighbors interaction V.

One remarkable fact about the one-dimensional magnetic systems is that all the excitations are collective. In Heisenberg chains, the excitations are described as spinons without mass

$S = \frac{1}{2}$. According to the Lieb-Schultz-Mattis theorem, for a half-integer spin chain an excitation spectrum is either gapless or degenerate [33]. Spinons present a dispersion relation which is given by $\hbar\omega = \pi|Jsen(qa)|$ [34], where a is the lattice constant and q is the wave vector, measured along the chain. This equation is the lower curve in Fig.2.9. The ground-state is gapless, because when $q \to 0$ (long wavelength limit), $\omega \to 0$. The upper curve comes from the fact that neutron diffraction experiments involve a change of spin of one and so it implies a creation or annihilation of a pair os spinons. Therefore, experimental data show a continuum of excitations between the lower and upper curves.

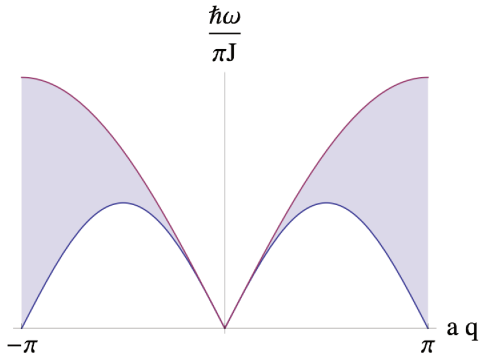

Fig. 2.9: The spinon continuum spectrum for the spin-$\frac{1}{2}$ antiferromagnetic chain. [34]

In contrast, for an integer spin chain, Haldane made the conjecture that its spin excitation spectrum is gapped [35].

- **Spin-Peierls transition**

Although spin-$\frac{1}{2}$ chains are gapless, they are susceptible to an instability which can open up a gap. This transition is known as spin-Peierls[36]. A coupling between the one-dimensional electronic structure and the three-dimensional lattice vibrations, i.e. the phonons, is the driving force to this transition. Thus, it is expected that materials which present this transition present spin-phonon coupling, which occurs when the exchange couplings are modulated by a modification of the bonding length between the spins. In the spinless fermions problem, this corresponds to a a modulation of the hopping parameters. The Hamiltonian which describes this transition is:

$$\hat{\mathcal{H}}^{total} = \sum_i J(u_i, u_{i+1})\vec{S}_{i+1}.\vec{S}_i + \hat{\mathcal{H}}_{phonons}(u) \tag{2.37}$$

where $\hat{\mathcal{H}}$ is a Hamiltonian describing the energetic cost of making deformations u_i to the lattice. Although the the spin system is one-dimensional, the phonons can be three-dimensional, which is often the case.

Before the transition temperature from short range order to long range order, an elastic distortion results in dimerization, as shown in Fig.2.10.

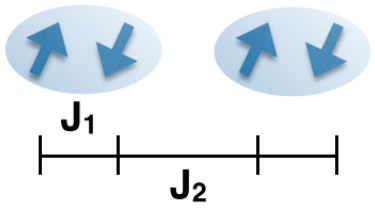

Fig. 2.10: Alternated chain of spins, with strong and weak bonds, representing the lattice dimerization. The strong bonds confine the spin pairs (dimers) to singlet states.

Thus, there will be two unequal alternating constants. When the dimerization is strong enough, as the temperature decreases, the system gets confined into singlets and there is an opening of the gap, corresponding to the gap between singlet states and triplet states in the dimers. The gap magnitude in each material is related to the degree of dimerization in the lattice. The signature of this transition is a kink in the magnetic susceptibility. Both compounds studied in this dissertation are believed to present spin-Peierls transitions[6, 37], as pointed out in the Introduction, and therefore, one can expect to observe spin-phonon coupling in these materials.

2.3 Lattice Dynamics

Let us now study the second part of Eq. 2.37. In order to understand crystallinity behavior that incorporates temperature as a variable, one needs to understand the crystal dynamics.

2.3.1 The harmonic approximation

Let $u_{j,\alpha}$ denote the component of the displacement vector $\alpha = x, y, z$ of the j^{th} atom from its equilibrium position. The energy can be expressed as a Taylor expansion:

$$E = E_0 + \frac{1}{2} \sum_{\substack{j,j' \\ \alpha,\alpha''}} \frac{\partial^2 E}{\partial u_{\alpha,j} \partial u_{\alpha',j'}} u_{\alpha,j} u_{\alpha',j'} + \frac{1}{n!} ... \tag{2.38}$$

where E_0 is the equilibrium lattice energy, which is the energy with all the atoms at rest. There is no first order term because all residual forces are zero. The second order term is called the harmonic energy. All higher order terms are classed together as the anharmonic energy. In the harmonic approximation, we neglect all the anharmonic terms.

Let us consider a one-dimensional example with an arbitrary number of atoms where it is allowed to extend the interactions beyond nearest neighbors. The energy is now written as [38]:

$$E_J = \frac{1}{2}\sum_{n,j'} K_{j,j',n}(u_{j,0} - u_{j,n})^2 \tag{2.39}$$

where K is the force constant, the sum over j' is along the atoms in different unit cells and n denotes which unit cell it is, and the sum over n includes the reference unit cell (labelled as n = 0). The force on the atom is given by:

$$F_J = -\frac{\partial E_j}{\partial u_{j,0}} = -\sum_{n,j'} K_{j,j',n}(u_{j,0} - u_{j',n}) = m_j \frac{\partial^2 u_{j,0}}{\partial t^2} \tag{2.40}$$

The solution of the harmonic equation of motion is a sinusoidal wave including the sum over all possible modes. A wave with wave vector k and frequency ω_k will cause an atom to be displaced according to the ansatz:

$$u_{j,n} = \sum_{\nu} \tilde{u}_{j,\nu} e^{i(kna-\omega_\nu t)} = \sum_{\nu} A_\nu m_j^{-1/2} e_{j,\nu} e^{i(kna-\omega_\nu t)} \tag{2.41}$$

where $\tilde{u}_{j,\nu}$ is the amplitude, a is the length of the unit cell, na is the position of the n^{th} atom, ν labels the mode (in a 1D system, there are as many modes as atoms in the unit cell), A_ν is a scale factor which is temperature dependent and $e_{j,\nu}$ are normalized variables which contains information about the relative displacements of the atoms due to the wave. Substituting the wave equation into the force equation, one can see that, for each value of ν:

$$-m_j^{1/2} e_{j,\nu} \omega_\nu^2 = -\sum_{n,j'} K_{j,j',n}(m_k^{1/2} e_{j,\nu} - m_{j'}^{1/2} e_{j',\nu} e^{ikna}) \tag{2.42}$$

We can generalize the results in a matrix form. If we define the N × 1 matrix $\mathbf{e}_\nu$ as formed from different components $e_{j,\nu}$, then:

$$\mathbf{e}_\nu \omega_\nu^2 = \mathbf{D} \times \mathbf{e} \tag{2.43}$$

where the N × N matrix $\mathbf{D}$, which is called the dynamical matrix, has components

$$D_{j,j'} = (m_j m_{j'})^{-1/2} \sum_n K_{j,j',n}(\delta_{j,j'} - e^{ikna}) \tag{2.44}$$

It is also possible to form a matrix $\mathbf{\Omega}$ with components $\omega_{\nu,\nu'} = \omega_\nu^2 \delta_{\nu,\nu'}$. Thus, $\mathbf{\Omega}$ is a diagonal matrix whose components are the squares of the vibrational angular frequencies. The problem can now be written as:

$$\mathbf{e} \times \mathbf{\Omega} = \mathbf{D} \times \mathbf{e} \Rightarrow \mathbf{\Omega} = \mathbf{e^{-1}} \times \mathbf{D} \times \mathbf{e} \tag{2.45}$$

This is an eigenvalue problem: the components of matrix $\mathbf{\Omega}$ are the eigenvalues of $\mathbf{D}$ and $\mathbf{e}$ contains the eigenvectors. This problem was optimized to be solved by performing calculations with a computer. The task is to set up the dynamical matrix using individual interatomic force constants, and then find its eigenvalues to get the mode frequencies. The mathematical formalism described here can be extended for calculations on three-dimensional systems. The term ikna in the exponential needs to be replaced by a i$\mathbf{k}$.$\mathbf{r}$ where $\mathbf{r}$ is the vector between the reference unit cell and its neighbor unit cell, and $\mathbf{k}$ is the 3D wave vector. Now, the three components of the displacement vector has to be taken into account, and therefore each component of the dynamical matrix will be replaced by a 3×3 matrix representing the combinations of the components of each pair of displacements. Indeed, the frequency matrix $\mathbf{\Omega}$ and the eigenvector matrix $\mathbf{e}$ will become 3N $\times$ 3N matrices.

2.3.2 Quantization of lattice vibrations

Previously, we have investigated how the vibrations are distributed along the crystal, but so far, we have not calculated the amplitudes of the vibrations. As one can expect, the vibration amplitude will strongly depend on temperature, and the proper treatment incorporates quantum mechanics. The harmonic vibrations can be quantized in the same way that the electromagnetic field is quantized into photons. The fundamental quanta of lattice vibrations are the so called phonons. The zero point energy, i.e. the ground-state energy is equal to $E_0 = \frac{1}{2}\hbar\omega$, and its corresponding motions at T = 0K are called the zero point motions. The mean energy of each vibrational mode is given by $E = \hbar\omega[\frac{1}{2} + n(\omega, T)]$, where $n(\omega, T)$ is the number of phonons, often called as the phonon number.

Let us now develop the phonon hamiltonian in the harmonic approximation. Any wave causes the atoms in the unit cell to be displaced by amounts given by the mode eigenvector $\mathbf{e}(\mathbf{k},\nu)$. Within the harmonic approximation, the eigenvectors will not depend on temperature. However, we expect the resultant atomic displacement to depend on temperature. We therefore

write the contribution of all normal modes to the displacement of the j^{th} atom in the l^{th} unit cell:

$$\mathbf{u}(jl) = \frac{1}{\sqrt{Nm_j}} \sum_{\mathbf{k},\nu} \mathbf{e}(j,\mathbf{k},\nu) e^{i\mathbf{k}.\mathbf{r}(jl)} Q(\mathbf{k},\nu) \tag{2.46}$$

where $\mathbf{r}$ denotes the atom position, $Q(\mathbf{k},\nu)$ is called the normal mode coordinate and subsumes the time and temperature dependence of the wave. The time dependence of Q is written as $\dot{Q}(\mathbf{k},\nu) = -i\omega(\mathbf{k},\nu)Q(\mathbf{k},\nu)$. By deriving Eq. 2.46 and substituting the value of $\dot{Q}(\mathbf{k},\nu)$, its possible to calculate velocity of an atom, and it is given by:

$$\dot{\mathbf{u}}(jl) = \frac{-i}{\sqrt{Nm_j}} \sum_{\mathbf{k},\nu} \omega(\mathbf{k},\nu) e^{i\mathbf{k}.\mathbf{r}(jl)} Q(\mathbf{k},\nu) \tag{2.47}$$

The kinetic energy of the atom will be given by $\frac{1}{2}m_j|\dot{\mathbf{u}}(jl)|^2$, and the total kinetic energy of the crystal can be obtained by summing over all atoms:

$$\begin{aligned} \frac{1}{2}\sum_{j,l} m_j|\dot{\mathbf{u}}(jl)|^2 = \frac{1}{2N}\sum_{j,l}\sum_{\substack{\mathbf{k},\mathbf{k}'\\ \nu,\nu'}} \omega(\mathbf{k},\nu)\omega(\mathbf{k}',\nu')\mathbf{e}(j,\mathbf{k},\nu).e^*(j,\mathbf{k}',\nu') \\ \times e^{i(\mathbf{k}-\mathbf{k}').\mathbf{r}(jl)} Q(\mathbf{k},\nu)Q^*(\mathbf{k}',\nu') \end{aligned} \tag{2.48}$$

By using the definition of the Delta function, its possible to notice that the sum over l does not vanish only if $\mathbf{k} = \mathbf{k}'$. Furthermore, by using the eigenvectors $\mathbf{e}$ normalization condition, the kinetic energy can be simplified to:

$$\frac{1}{2}\sum_{j,l} m_j|\dot{\mathbf{u}}(jl)|^2 = \frac{1}{2}\sum_{\mathbf{k},\nu} \omega^2(\mathbf{k},\nu)|Q(\mathbf{k},\nu)|^2 \tag{2.49}$$

Obviously, the the total phonon energy is the sum of the kinetic contribution and the vibrational potential energy. In order to derive an expression for the potential energy, one has to consider the dynamical matrix, but for instance, we will state that the average vibrational potential energy is equal to the average of the kinetic term. Therefore, the phonon vibrational energy is:

$$E = \sum_{\mathbf{k},\nu} = \omega^2(\mathbf{k},\nu)\left\langle \left| Q(\mathbf{k},\nu) \right|^2 \right\rangle = \sum_{\mathbf{k},\nu} \hbar\omega(\mathbf{k},\nu)\Big(n(\omega(\mathbf{k},\nu),T) + \frac{1}{2}\Big) \tag{2.50}$$

The number of phonons in thermal equilibrium is given by the Bose-Einstein distribution, derived from the partition function for phonons. In the high temperature limit, where

$k_BT > \hbar\omega$, it is possible to expand the thermodynamic funtion as powers of $\hbar\omega/k_BT$, and $\langle \mid Q^2(\mathbf{k},\nu) \mid^2 \rangle = \frac{k_BT}{\omega^2(\mathbf{k},\nu)}$. The Hamiltonian of the crystal, in terms of the individual vibrations, is given by:

$$\hat{\mathcal{H}}^{vib} = \frac{1}{2}\sum_{jl} m_j|\dot{\mathbf{u}}(jl)|^2 + \frac{1}{2}\sum_{j,lj',l'} \frac{\partial^2 E}{\partial \mathbf{u}(jl).\partial \mathbf{u}(j'l')}\mathbf{u}(jl).\mathbf{u}(j'l') \tag{2.51}$$

From the analysis done above, it is possible to notice that the Hamiltonian can be written as:

$$\hat{\mathcal{H}}^{vib} = \frac{1}{2}\sum_{\mathbf{k},\nu} \dot{Q}(\mathbf{k},\nu)\dot{Q}(-\mathbf{k},\nu) + \frac{1}{2}\sum_{\mathbf{k},\nu} \omega^2(\mathbf{k},\nu)Q(\mathbf{k},\nu)Q(-\mathbf{k},\nu) \tag{2.52}$$

2.3.3 Anharmonic interactions

The basic harmonic theory has proven to be successful to provide an understanding of some phenomena regarding the interaction between light and matter. However, some phenomena can not be explained within this approximation, for example, the temperature dependence of phonon frequencies, thermal expansion, thermal conductivity etc. Let us now modify the harmonic model in order to have a better understanding. The anharmonic terms in Eq.2.38 does not have an exact solution. An approximation that can be made is to consider that the anharmonic terms are small compared to the harmonic ones, and thus they simply modify the harmonic picture. This is the so called quasiharmonic approximation, in which the anharmonic interactions are assumed to give rise to changes in the phonon frequencies due to the change in the material structure. Moreover, the phonon frequencies can be modified through other effects such as direct interaction between different phonons, the latter being known as the renormalized phonon theory.

Our approach will be to expand the anharmonic terms in the Hamiltonian of Eq.2.52:

$$\begin{aligned}\hat{\mathcal{H}}^{vib} = &\frac{1}{2}\sum_{\mathbf{k},\nu} \dot{Q}(\mathbf{k},\nu)\dot{Q}(-\mathbf{k},\nu) + \frac{1}{2}\sum_{\mathbf{k},\nu} \omega^2(\mathbf{k},\nu)Q(\mathbf{k},\nu)Q(-\mathbf{k},\nu) \\ &+\frac{1}{3!}\sum_{\substack{\mathbf{k},\mathbf{k}',\mathbf{k}'' \\ \nu,\nu',\nu''}} \alpha^{(3)}_{\substack{\mathbf{k},\mathbf{k}',\mathbf{k}'' \\ \nu,\nu',\nu''}} Q(\mathbf{k},\nu)Q(\mathbf{k}',\nu')Q(\mathbf{k}'',\nu'')\Delta(\mathbf{k}+\mathbf{k}'+\mathbf{k}'') \\ &+\frac{1}{4!}\sum_{\substack{\mathbf{k},\mathbf{k}',\mathbf{k}'',\mathbf{k}''' \\ \nu,\nu',\nu'',\nu'''}} \ldots\end{aligned} \tag{2.53}$$

The α coefficients are related to the n^{th} derivative of the energy. Moreover, $\Delta(\mathbf{K})$ is related to a conservation law:

$$\Delta(\mathbf{K}) = \begin{cases} 1, & \text{if } \mathbf{K} = \mathbf{G} \\ 0, & \text{if } \mathbf{K} \neq \mathbf{G} \end{cases} \tag{2.54}$$

where $\mathbf{G}$ is the reciprocal lattice vector. It is possible to show, using the second quantization formalism, that the anharmonic terms have a physical interpretation which is related to collisions between phonons which lead to change in the frequencies as well as creation and annihilation of phonons. The third order anharmonic event is depicted in Fig.2.11. In the case shown in the left, the phonon spontaneously decays into two others and in the other case, two phonons merge to form a third one.

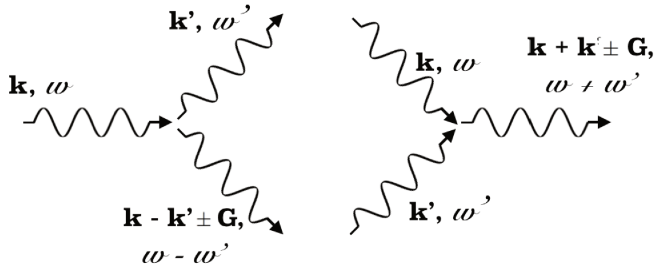

Fig. 2.11: Feynman diagram representing phonon collisions in third-order anharmonic interaction. In the left, one phonon spontaneously decays into two others conserving the energy. In the right, two phonons merge and form a third.

In the processes depicted in Fig.2.11, the phonons are sketched in a way that suggests that the motions either side of the interactions are in the same direction. Nevertheless, the wave vector conservation law implies a change in the overall wave vector by addition or subtraction of a reciprocal lattice vector; and therefore the flow of energy can be changed, even reversed by anharmonic interactions. We have shown here the third order processes, but there are also the fourth order interactions which can also give a significant contribution to the energy of the crystals. Furthermore, we can assert the fact that the anharmonic events can be pictured as a change in the wave vectors and energies, and even creation and annihilation of phonons, means that the phonons have a lifetime. Therefore, the vibrations can be described as a sinusoidal function multiplied by an exponential decay to represent the finite lifetime. In this way, the Fourier transform will be the convolution of a Dirac delta function at the vibrational frequency of an exponential function, which is a Lorentzian function. This means that the a measurement of an anharmonic peak width in an experiment (see Chapter 3) with high resolution will give

the inverse of the phonon lifetime. The width of this peak will increase on heating, since more phonons will emerge and therefore the probability of collisions and the process shown in Fig.2.11 will increase. This effect is called phonon broadening.

Thermal Expansion

The volume thermal expansion coefficient β can be written as:

$$\beta = \frac{1}{V}\Big(\frac{\partial V}{\partial T}\Big)_P = K_T\Big(\frac{\partial P}{\partial T}\Big)_V \tag{2.55}$$

where K_T is the isothermal compressibility. Pressure is given by the derivative of the free energy with respect to V, i.e. $P = -\big(\frac{\partial F}{\partial V}\big)_T$. The free energy in the high temperature limit is: $F = E + k_BT\sum_j ln(\frac{\hbar\omega}{k_BT})$, where E is the lattice energy. Therefore, the pressure is $P = -\frac{\partial E}{\partial V} - k_BT\sum_j \frac{1}{\omega_j}\frac{\partial \omega_j}{\partial V}$. We now calculate β:

$$\beta = -K_Tk_B\sum_j \frac{1}{\omega_j}\frac{\partial \omega_j}{\partial V} \tag{2.56}$$

Let us now define the Grueneisen parameter:

$$\gamma_j = -\frac{V}{\omega_j}\frac{\partial \omega_j}{\partial V} = -\frac{\partial ln\omega_j}{\partial lnV} \tag{2.57}$$

and the Grueneisen parameter will be positive for the usual case where a mode frequency increases as the volume decreases. The thermal expansion equation gets:

$$\beta = \frac{K_Tk_B}{V}\sum_j \gamma_j = \frac{3K_TR\gamma}{V} \tag{2.58}$$

where γ is defined as the sum over the $3N_A$ individual parameters.

The phonon frequency change due to the thermal expansion can approximated by Grueneisen law, expressed by:

$$\Big(\frac{\Delta\omega}{\omega}\Big) = -\gamma\Big(\frac{\Delta V}{V}\Big) \tag{2.59}$$

Note that this law is applicable to crystal lattices which expand isotropically.

Temperature dependence of phonon frequencies

It is not possible to solve the Hamiltonian Eq.2.53 exactly, and then we will look for a quasi-harmonic approximate solution, which retains the main features of the harmonic model. We will assume that the temperature dependence of the phonon frequencies are only due to

the dependence on the force constants with volume, i.e. will depend only on the crystal volume dependence with temperature. In our approximation, we will consider the second and the fourth term in the Hamiltonian Eq.2.53, neglecting the kinetic and the third term. We will now neglect the fluctuations and use a mean-field approach:

$$\begin{aligned} Q(\mathbf{k}'',\nu'')Q(\mathbf{k}''',\nu''') &\rightarrow \langle Q(\mathbf{k}'',\nu'')Q(\mathbf{k}''',\nu''')\rangle \\ &\approx \frac{k_B T}{\omega^2(\mathbf{k}'',\nu'')}\delta_{\mathbf{k}'',-\mathbf{k}'''}\delta_{\nu'',\nu'''} \end{aligned} \tag{2.60}$$

where we have also assumed that we can work with the high-temperature limit, and the delta in the $\mathbf{k}$ wave vector is expressing the conservation law and the delta in the ν express the orthogonality condition. The Hamiltonian gets:

$$\hat{\mathcal{H}} = \frac{1}{2}\sum_{\mathbf{k},\nu}\omega^2(\mathbf{k},\nu)Q(\mathbf{k},\nu)Q(-\mathbf{k},\nu) + \frac{k_B T}{4}\sum_{\substack{\mathbf{k},\mathbf{k}''\\ \nu,\nu''}}\alpha^{(4)}_{\substack{\mathbf{k},-\mathbf{k},\mathbf{k}'',-\mathbf{k}''\\ \nu,\nu,\nu'',\nu''}}\frac{Q(\mathbf{k},\nu)Q(-\mathbf{k},\nu)}{\omega^2(\mathbf{k}'',\nu'')} \tag{2.61}$$

There are six ways of selecting independent pairs for the second term, and this is why it has been multiplied by six.

$$\begin{aligned} \hat{\mathcal{H}} &= \frac{1}{2}\sum_{\mathbf{k},\nu}\left(\omega^2(\mathbf{k},\nu) + \frac{k_B T}{2}\sum_{\substack{\mathbf{k},\mathbf{k}''\\ \nu,\nu''}}\frac{\alpha^{(4)}_{\substack{\mathbf{k},-\mathbf{k},\mathbf{k}'',-\mathbf{k}''\\ \nu,\nu,\nu'',\nu''}}}{\omega^2(\mathbf{k}'',\nu'')}\right)\times Q(\mathbf{k},\nu)Q(-\mathbf{k},\nu) \\ &= \frac{1}{2}\sum_{\mathbf{k},\nu}\tilde{\omega}^2(\mathbf{k},\nu)Q(\mathbf{k},\nu)Q(-\mathbf{k},\nu) \end{aligned} \tag{2.62}$$

from where we take the renormalized phonon frequencies:

$$\tilde{\omega}^2(\mathbf{k},\nu) = \omega^2(\mathbf{k},\nu) + \frac{k_B T}{2}\sum_{\mathbf{k}'',\nu''}\frac{\alpha^{(4)}_{\substack{\mathbf{k},-\mathbf{k},\mathbf{k}'',-\mathbf{k}''\\ \nu,\nu,\nu'',\nu''}}}{\omega^2(\mathbf{k}',\nu')} \tag{2.63}$$

This gives a temperature dependence to all phonons. If the coefficients are positive, the phonon frequencies will increase with temperature. Nevertheless, the effects of the thermal expansion usually causes a decrease in the phonon frequency since the force constants decrease as bonds increase in length, and this effect usually dominates. In the next Chapter (Section 3.2), we will address a calculation for the phonon frequency dependence with temperature which

takes into account other effects such as magnetic coupling with the phonons.

2.3.4 Ab-initio lattice dynamical calculations

In order to investigate theoretically systems as complicated as molecular crystals, it is necessary to model the interactions and it has to be as accurately as possible at the same time as being computationally doable. The simplest approach is to use empirical potentials, but they are limited and inadequate for calculating dynamical properties. Modeling interactions with no *a priori* knowledge of empirical potentials require the usage of the sophisticated ab-initio calculations, which attempt to solve the Schroedinger's equation governing the dynamics of electrons. The methodology for such calculations is the density functional theory (DFT)[39], which will be described below. By solving the electronic structure of the system, a deeper understanding of the system's behavior including thermodynamical properties can be obtained via simulation. Within the ab-initio [9]lattice dynamical calculation, it is possible to determine the symmetry of the lattice vibrations, i.e. how are the atomic motions at certain vibration and it is also possible to obtain a simulation of the Raman spectra.

In principle, it is possible to obtain the ground state of a system by solving the quantum mechanical wave equation governing the dynamics:

$$\hat{\mathcal{H}}\Psi(\{r_i\},\{R_I\}) = E\Psi(\{r_i\},\{R_I\}) \tag{2.64}$$

where now $\Psi(\{r_i\},\{R_I\})$ is the many electron wavefunction, where r_i denotes the electrons position and R_I denotes the nuclei positions. The Hamiltonian is therefore

$$\hat{\mathcal{H}} = T_n + V_{nn} + T_e + V_{ee} + V_{en} \tag{2.65}$$

where T stands for kinetic energy, V for Coulomb potential energy, e for electrons, n for nuclei and the electron-electron, nuclei-nuclei and electron-nuclei interactions are being represented by V_{ee}, V_{nn} and V_{en}, respectively. This is a very complicated problem, since we are dealing with a many body system. To solve this equation, one first needs to make the Born-Oppenheimer approximation[26], i.e. the electron's and atomic nuclei's dynamics can be decoupled, since the atomic nuclei is much heavier than the electrons. As a result of this approximation, one can neglect the kinetic term T_n. Then, one has $\Psi(\{r_i\},\{R_I\}) = \Psi(\{r_i\})\Psi(\{R_I\})$. This is still a complicated problem, and it is not possible to solve this equation for two reasons: one mole of a solid contains N $\sim 10^{28}$ electrons, since the many electron wavefunction contains 3N degrees of freedom, this is intractable; moreover, the electron-electron interaction results in

[9]Ab-initio: from first principles.

correlated electronic motions. Thus, one has to look for approximations that transform this in a numerical tractable solution.

We now start the density functional theory approach and we define the electron density

$$n(r) = N \int d^3r_2 ... \int d^3r_N \Psi^*(\mathbf{r_1}, \mathbf{r_2}, ...\mathbf{r_N})\Psi(\mathbf{r_1}, \mathbf{r_2}, ...\mathbf{r_N}) \tag{2.66}$$

The electron density in DFT is the central variable rather than the many-body wave function, and this reduces the 3N variables to only 3 variables. Another approximation that we use is the Hartree approximation, where the initial ansatz is to write the wavefunction as: $\Psi(\mathbf{r_1}, \mathbf{r_2}, ...\mathbf{r_N}) = \psi_1(\mathbf{r_1})\psi_2(\mathbf{r_2})...\psi_N(\mathbf{r_N})$, which means that electrons are treated as being independent and only interacting via the mean-field Coulomb potential. Therefore, we redefine the electron density in terms of the individual electron wave functions $n(\mathbf{r}) = 2\sum_i \psi_i^*(\mathbf{r})\psi_i(\mathbf{r})$. We consider here the Hohenberg-Kohn-Sham formulation of DFT [40, 41], and it is based upon two remarkable theorems:

- **First theorem**: For any system of interacting particles in an external potential, the ground state energy is a unique functional of the electron density $n(\mathbf{r}) : E = E[n(\mathbf{r})]$;
- **Second theorem**: The density that minimizes the total energy is the exact ground state density.

Kohn and Sham put forward a new structure for the energy functional, and the functional is split into 3 parts:

$$E[n(\mathbf{r})] = T_e[n(\mathbf{r})] + E_H[n(\mathbf{r})] + E_{xc}[n(\mathbf{r})] \tag{2.67}$$

where $T_e[n(\mathbf{r})]$ is the kinetic energy functional for a fictitious system of non-interacting electrons producing the same density $[n(\mathbf{r})]$. $E_H[n(\mathbf{r})]$ is called the Hartree [42] energy and it arises from the mutual Coulomb repulsion of all electrons ($E_H[n(\mathbf{r})] = \frac{1}{2}\int\int \frac{n(\mathbf{r})n(\mathbf{r'})}{|r-r'|} d^3r d^3r'$) and E_{xc} is the exchange correlation functional. The first and second terms in the functional equation are known, but the third is unknown, and hence we need to approximate it. A number of approximations to the exchange-correlation functional have been derived by researchers, including the Local Density Approximation (LDA)[43] which express the E_{xc} in terms of a density of a uniform electron gas and the Generalized Gradient Approximation (GGA)[44], which takes into account $n(\mathbf{r})$ inhomogeneities by including the gradient of the electron density. The correlated nature of the electrons within a solid is not the only obstacle to solving the Schroedinger's equations for a condensed matter system: for solids, there are effectively an

infinite number of electrons. One must appeal to Bloch's theorem[17], which states that the wave function of an electron within a periodic potential is:

$$\psi_{j,k}(\mathbf{r}) = u_j e^{i\mathbf{k}.\mathbf{r}} \tag{2.68}$$

where $u_j(\mathbf{r})$ is a functional that possesses the periodicity of the potential: $u_j(\mathbf{r}) = \sum_G c_j e^{i\mathbf{G}.\mathbf{r}}$ where G are the reciprocal lattice vectors $\mathbf{G}.\mathbf{R} = e\pi m$, where m is an integer, $\mathbf{R}$ is the real space lattice vectors and c_j is an expansion coefficient. Therefore,

$$\Psi_{j,\mathbf{k}} = \sum_{\mathbf{G}} c_j e^{i(\mathbf{k}+\mathbf{G}).\mathbf{r}} \tag{2.69}$$

The net effect of Block's theorem is to change the problem of an infinite number of electrons to one of considering only the number of electrons in the unit cell (or half of it, depending if the spins are degenerate or not) at a finite number of k-points chosen as to the Brillouin point Zone. Numerically, this means that we have defined an energy cutoff $E_{cutoff} = \frac{\hbar^2}{2m}|\mathbf{k}+\mathbf{G}|^2$.

Although it was possible to solve the Kohn-Sham equations when expanding the wave functions in terms of plane waves, an all-electron calculation including core and valence electrons, along with the Coulomb potential of the nuclei would still be forbidden when using a set of plane waves. This happens because the tightly bound core orbitals and highly oscillatory nature of valence electrons demand a very high value for E_{cutoff}. We now introduce the pseudo-potential approximation: the core and ionic potential are removed and replaced by a pseudo-potential which acts on a set of pseudo-wave functions. Current DFT codes provide a library of pseudo-potentials for each element in the periodic table.

Once the electron density is determined, it is possible to calculate the force acting on the ions, and then it is possible to move along each ion and the ionic ground state can be calculated. It is also possible to displace the ions from the ionic ground state and determine the force on the other ions, thus obtaining dynamical matrices and vibrational frequencies.

Chapter 3

Experimental Techniques

In this chapter, we will review the theoretical basis of Raman scattering on phonons and its applications to study magnetic systems via the spin-phonon coupling. Finally, the experimental setup will be outlined.

3.1 Phononic Raman Scattering

In 1928, Sir Chandrasekhra Venkata Raman discovered a phenomenon which nowadays carries his name. In 1930, Sir Raman won the Nobel prize for his discovery[45]. Back then, Sir Raman used the sunlight as the excitation source, a telescope as the collector and his eyes as a detector. Considerable progress on instrumentation has been achieved since then. A typical Raman scattering process is schematically shown in Fig.3.1-a): a laser with a well defined wavelength $\omega_i, \mathbf{k_i}$ and a polarization P_i comes and excites a sample. The light is scattered by the sample with a wavelength $\omega_f, \mathbf{k_f}$ and polarization P_f and its intensity as a function of the frequency change, i.e. its spectral density is measured with a detector. Since the wavelength of the light is in the visible region of the electromagnetic spectrum, and therefore it is much longer than the interatomic spacings, Raman spectroscopy can only measure phonons with wave vectors close to zero. The scattered light consists of a component of the Rayleigh scattering, which is an elastic contribution, the Stokes ($\omega_f < \omega_i$) component and the anti-Stokes component ($\omega_f > \omega_i$), as shown in Fig.3.1-b).

The Stokes component corresponds to phonon emission, while the anti-Stokes correspond to phonon absorption. An anti-Stokes process will only be present if there are phonons present in the material before the light is incident. Therefore, the probability that an anti-Stokes process occur at cryogenics temperatures is low. In contrast, the Stokes process does not require a phonon to be present and thus can occur at any temperature.

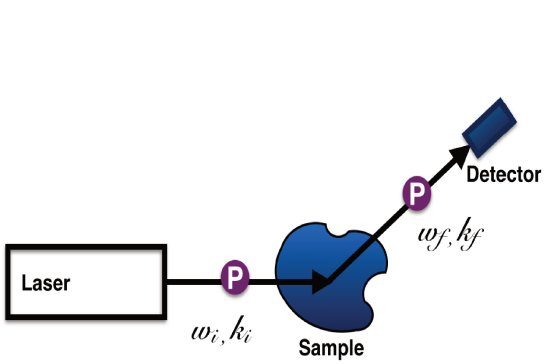

(a)

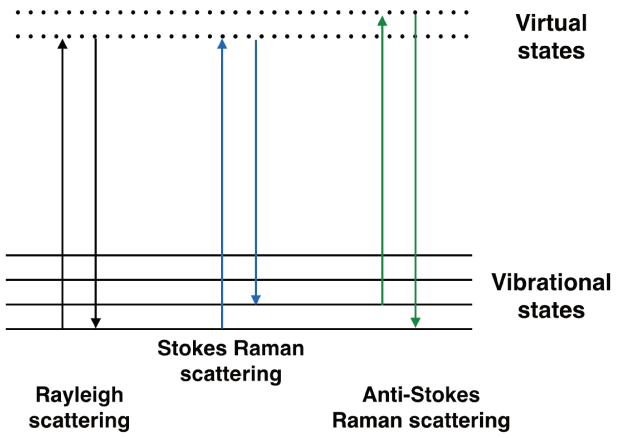

(b)

Fig. 3.1: a) Schematic view of a scattering process. b) Diagram showing the elastic or Rayleigh scattering ($\omega_i = \omega_s$), the Stokes component ($\omega_f < \omega_i$), and the anti-Stokes component ($\omega_f > \omega_i$).

The incoming electromagnetic wave will interact with the sample, so let us consider the response relation between the materials polarization and the external electric field:

$$P(\omega, r) = \chi(\omega) E(\omega, r) \tag{3.1}$$

where $\chi(\omega)$ is the electric susceptibility tensor. The spectral density from light scattering is given by the fluctuation-dissipation theorem[46]:

$$\rho(\mathbf{q}, \omega) \sim \int \langle \delta\chi^*(\mathbf{q}, t) \delta\chi(\mathbf{q}, 0) \rangle \, e^{i\omega t} dt \tag{3.2}$$

where $\mathbf{q} = \mathbf{k_i} - \mathbf{k_f}$ and $\omega = \omega_i - \omega_f$ are the wave vector transfer and number. In solids, the fluctuations of the electric susceptibility tensor originate from two sources. One is the density fluctuations which leads to a continuum scattering and the other is due to internal degrees of freedom like phonons, magnons. The latter ones lead to peaks in the spectral density at frequencies corresponding to the energy of these excitations. In order to calculate the transition electric susceptibility we have to consider the Hamiltonian which describes the coupling of electrons to a radiation field described by a vector potential $\mathbf{A}$ [1].

This Hamiltonian is written as:

$$\hat{\mathcal{H}}^{e^- - light} = \hat{\mathcal{H}_{\mathcal{A}}} + \hat{\mathcal{H}_{\mathcal{A}\mathcal{A}}} \tag{3.3}$$

[1]We are following ref. [46]

where

$$\hat{\mathcal{H}}_{AA} = \frac{e^2}{2mc^2} \sum_{\mathbf{k_i},\omega_i} \sum_{\mathbf{k_f},\omega_f} N(-\mathbf{k_i} + \mathbf{k_f}) \mathbf{A}(\mathbf{k_i}, \omega_i).A^*(\mathbf{k_f}, \omega_f) \tag{3.4}$$

and

$$\hat{\mathcal{H}}_{A} = \frac{e}{mc} \sum_{\mathbf{k_i},\omega_i} \mathbf{p}(-\mathbf{k_i}).\mathbf{A}(\mathbf{k_i}, \omega_i) \tag{3.5}$$

where $\mathbf{A}(\mathbf{k_i}, \omega_i)$ and $\mathbf{A}^*(\mathbf{k_f}, \omega_f)$ are the amplitudes of the Fourier components of the potential vector of the incident and scattered photons, and where:

$$\begin{aligned} N(-\mathbf{k_i} + \mathbf{k_f}) &= \sum_j e^{i(\mathbf{k_i}-\mathbf{k_f}).\mathbf{r_j}} \\ \mathbf{p}(-\mathbf{k_i} + \mathbf{k_f}) &= \sum_j e^{i(\mathbf{k_i}-\mathbf{k_f}).\mathbf{r_j}} \mathbf{p_j} \end{aligned} \tag{3.6}$$

where $\mathbf{r_j}$ and $\mathbf{p_j}$ are the position and momentum operators of the j^{th} electron. $N(-\mathbf{k_i} + \mathbf{k_f})$ and $\mathbf{p}(-\mathbf{k_i} + \mathbf{k_f})$ are the Fourier transform of the many-particle number and momentum operators.

The contribution of the electrons to the transition electric susceptibility involves a two photon process, where the incident photon is destroyed and the scattered photon is created. The differential cross-section in terms of the matrix elements of the transition susceptibility operator is:

$$\frac{d^2\sigma}{d\Omega d\omega_f} = \left(\frac{\omega_f}{c}\right)^4 \frac{\omega_i}{\omega_f} V^2 \sum_{i,f} P(E_i) \delta\{\frac{(E_i - E_f)}{\hbar} - \omega\}.|\hat{e_f}.\left\langle f\right| \delta\chi_{\mu\nu} \left|i\right\rangle .\hat{e_i}|^2 \tag{3.7}$$

where

$$\begin{aligned} \left\langle f\right| \delta\chi_{\mu\nu} \left|i\right\rangle = \frac{e^2}{m^2\omega_f^2 V}\{-m \left\langle f\right| N(-\mathbf{k_i} + \mathbf{k_i}) \left|i\right\rangle\} + \sum_b [\frac{\left\langle f\right| p_\mu(\mathbf{k_f}) \left|b\right\rangle \left\langle b\right| p_\nu(-\mathbf{k_i}) \left|i\right\rangle}{E_b - E_i - \hbar\omega_i} \\ + \frac{\left\langle f\right| p_\nu(-\mathbf{k_i}) \left|b\right\rangle \left\langle b\right| p_\mu(\mathbf{k_f}) \left|i\right\rangle}{E_b - E_i + \hbar\omega_f}] \end{aligned} \tag{3.8}$$

where $\left|i\right\rangle, \left|f\right\rangle \left|b\right\rangle$ represents the initial, final and intermediate states, and V is the scattering volume. In order to calculate the matrix elements in Eq.3.8, one has to separate the electronic and ionic motions as well as the electronic single particle and collective coordinates in adiabatic approximations. Its non-zero components are determined by symmetry properties of the three

eigenstates.

Scattering by one phonon in adiabatic approximation

Inelastic light scattering by electronic excitations and by lattice vibrations are described by the last term in Eq.3.8, and it involves the electron-radiation interaction. Light scattering by electronic excitations is given by this term when the initial and final states have the same phonon occupation number and differ by their electronic states. Light scattering by lattice vibrations are represented by this term when they differ only by their phonon occupation numbers. One phonon scattering arises from third order time-dependent perturbation theory rather than a direct photon-phonon interactions, because of a large difference of the photon energy ($\hbar \approx 1.5 - 2.5eV$) and the phonon energy ($< 100meV$). The scattering process can be described by the Feynman diagram depicted in Fig.3.2 and the process includes three virtual electronic transitions:

- 1) A photon comes and excites an electron-hole pair via the electron-photon coupling, and the photon is annihilated;
- 2) The electron-phonon interaction causes a transition of the electron or hole to a virtual state. It is going to be an electron if it is a Stokes process and a hole if it is anti-stokes;
- 3) The transition to the electronic ground-state occurs via the recombination of the electron-hole pair from the virtual state with the creation of a scattered phonon.

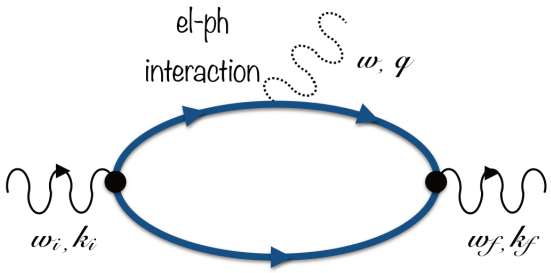

Fig. 3.2: Feynman diagram of the first order phonon scattering, representing 1-3 electronic transitions. The conservation of momentum gives: $\mathbf{k_i} = \mathbf{k_f} + \mathbf{q}$, and thus we see that $|\mathbf{q}|$ is maximum for a back-scattering geometry. Therefore $q \approx |\mathbf{k} - (-\mathbf{k})| \approx 2\frac{n\omega}{c} \approx 10^7 m^{-1}$. This is very small compared to the size of the Brillouin zone a typical crystal ($\sim 10^{10}\ m^{-1}$) and therefore inelastic visible light scattering can only probe small wave vector phonons.

The Hamiltonian $\hat{\mathcal{H}}_A$ represents the electron-photon first and thirds steps in the description of the scattered process. The Hamiltonian $\hat{\mathcal{H}}_{AA}$ is the contribution of the electron-phonon

interaction, which occur by their coupling differentiating in the two different ways described above: phonons coupling to electronic states with the same occupancy, and phonons coupling to occupied and unoccupied states. We have briefly talked about selection rules. Eq.3.7 requires that:

$$\hat{e}_f . \langle f | \delta\chi_{\mu\nu} | i \rangle . \hat{e}_i \neq 0 \tag{3.9}$$

and this determines the selection rules on the polarizations of the incident and scattered light.

3.2 Spin-phonon coupling

The question we try to address in this section is how can one obtain information about the magnetic correlations with Raman spectroscopy through the investigation of phonons. In magnetic materials, the temperature dependence of the frequency of the α-phonon is expressed by[2]:

$$\omega_\alpha(T) - \omega_\alpha(T_0) = \Delta\omega_\alpha(T) = (\Delta\omega_\alpha)_{thermal} + (\Delta\omega_\alpha)_{anhar} + (\Delta\omega_\alpha)_{ren} + (\Delta\omega_\alpha)_{s-p} \tag{3.10}$$

The first term in Eq.3.10 is the thermal expansion (explained in Chapter 2, Section 2.3). The second term is the anharmonic contribution at a constant volume. The third term refers to a renormalization of the electronic states at a critical temperature. Finally, the spin-phonon contribution is caused by the modulation of the spin coupling energy, as highlighted in the previous Chapter - Subsection 2.2.1. This contribution was first studied by Baltensperger and Helman for the specific case of EuO[48]. Let us study this interaction, assuming that the magnetic Hamiltonian is the Heisenberg one - Eq.2.31. We consider here any exchange mechanism where the exchange integral can be modulated by atomic displacements, thus excluding couplings via delocalized electrons. The exchange integral depends on the spatial positions of the magnetic ions i and j, as well as the positions of any ion which is sitting on the integral path between the two magnetic ions. Let us expand J_{ij} in terms of the nuclear position of a given ion k[3]:

$$\Delta J_{ij}(\mathbf{u_k}) = [\mathbf{u_k}.\vec{\nabla}_k]J_{ij} + \frac{1}{2!}[\mathbf{u_k}.\vec{\nabla}_k]^2 J_{ij} + ... \tag{3.11}$$

[2]We are following ref. [47]

where $\mathbf{u_k}$ is the displacement vector with respect to the equilibrium position of the k ion at a given temperature. Let us write the displacement vector $\mathbf{u_k}$ as a static component, which accounts for a change of the equilibrium displacements with temperature, and a dynamical component, which accounts for the fluctuation of the equilibrium positions due to the vibrations:

$$\mathbf{u_k} = \mathbf{u_k^0} + \mathbf{u_k}(t) \tag{3.12}$$

where $\mathbf{u_k^0}$ and $\mathbf{u_k}$(t) are the static and dynamical components. Now, Eq.3.11 can be separated in static and dynamical contributions:

$$\Delta J_{ij}(\mathbf{u_k}(t)) = [\mathbf{u_k^0}.\vec{\nabla}_k]J_{ij} + \frac{1}{2}[\mathbf{u_k^0}.\vec{\nabla}_k]^2 J_{ij} + \frac{1}{2}[\mathbf{u_k}(t).\vec{\nabla}_k]^2 J_{ij} + ... \tag{3.13}$$

Static terms on the right-side of this equation give origin to an accommodation on the equilibrium position of some ions around the spin order temperature, which is known as the exchange striction. This effect will be taken into account in the term $(\Delta\omega_\alpha)_{thermal}$. On the other hand, the dynamical term will be responsible for the spin-phonon coupling. The change in the exchange integral due to harmonic displacements is given by:

$$\Delta J_{ij}(t) = \frac{1}{2}\sum_k [\mathbf{u_k}(t).\vec{\nabla}_k]^2 J_{ij} \tag{3.14}$$

where the sum is over all atoms in the crystal. Therefore, the variation in the exchange energy(Eq.2.31) due to the vibration will be:

$$\begin{aligned} \Delta\hat{\mathcal{H}}^{spin-phonon} &= -\frac{1}{2}\sum_{i,j>i}\sum_k [\mathbf{u_k}(t).\vec{\nabla}_k]^2 J_{ij} \langle \mathbf{S_i}.\mathbf{S_j}\rangle \\ &= -\frac{1}{2}\Big(\sum_k [\mathbf{u_k}(t).\vec{\nabla}_k]^2\Big)\Big(\sum_{i,j>i} J_{ij}\langle \mathbf{S_i}.\mathbf{S_j}\rangle\Big) \end{aligned} \tag{3.15}$$

Since this equation involves quadratic terms of the ionic displacements, one can write:

$$\Delta\hat{\mathcal{H}}^{spin-phonon} = \frac{1}{2}\sum_k \mathbf{u_k}(t)\mathbf{D_k}^{spin}\mathbf{u_k}(t) \tag{3.16}$$

where $\mathbf{D_k}^{spin}$ is a 3×3 tensor, whose components are the second derivatives of the integral exchange J_{ij} times de spin correlation function summed over the magnetic ions:

[3]We are assuming adiabatic approximation.

$$(\mathbf{D_k}^{spin})_{l,m} = -\sum_{i,j>i} \frac{\partial^2 J_{ij}}{\partial(u_k)_l \partial(u_k)_m} \langle \mathbf{S_i}.\mathbf{S_j} \rangle \tag{3.17}$$

It is possible to notice that there will be a change in the magnetic energy and a change in the elastic energy, as well as a change in the eigenfrequencies of some phonons. Indeed, by referring to Eq.2.39, the elastic potential of the ions can be written as:

$$U^{elastic} = \frac{1}{2} \sum_{k,k'} \mathbf{u_k}(t) \mathbf{D_{k,k'}}^{elastic} \mathbf{u'_k}(t) \tag{3.18}$$

and we write

$$\begin{aligned} \mathbf{D_{k,k'}}^{elastic} &= \delta_{k,k'} \sum_{k''} \Phi_{k,k''} + \Phi_{k,k'} \\ (\Phi_{k,k'})_{l,m} &= \frac{\partial^2 \phi_{k,k'}}{\partial(r_{k,k'})_l \partial(r_{k,k'})_m} \end{aligned} \tag{3.19}$$

where $\phi_{k,k'}$ is the potential energy between the k and k' ions, and $(r_{k,k'})_l$ is the l^{th} component of the position vector between the two ions k and k'. Then, the harmonic potential is given by:

$$\begin{aligned} U^{harm} &= U^{elastic} + \Delta\hat{\mathcal{H}}^{spin-phonon} = \\ &= \frac{1}{2} \sum_{k} \mathbf{u_k}(t) (\mathbf{D_{k,k'}}^{elastic} + \mathbf{D_k}^{spin}) \mathbf{u_k}(t) + \frac{1}{2} \sum_{k,k' \neq k} \mathbf{u_k}(t) \mathbf{D_{k,k'}}^{elastic} \mathbf{u'_k}(t) \end{aligned} \tag{3.20}$$

Since the $\mathbf{D_k}^{spin}$ tensor elements are composed by terms which are proportional to $\langle \mathbf{S_i}.\mathbf{S_j} \rangle$, this tensor vanishes for temperatures well above the ordering temperature. Thus, we expect that the frequencies of some phonon modes, which participates in the magnetic coupling, deviate for $T < T_C$. If the value of $\hat{\mathcal{H}}^{spin-phonon}$ is negative for $T < T_C$, this phonon will be contributing to the stabilization of magnetic coupling. The mean potential energy and the kinetic energy of this phonon will be reduced, and this is a softening. Therefore:

- phonon softening $\Leftrightarrow$ magnetic ordering stabilization by the vibration;
- phonon hardening $\Leftrightarrow$ magnetic ordering destabilization by the vibration.

The correction to Eq.2.40 due to the spin-phonon coupling will give a new motion equation for the k ion which is given by:

$$M_k \ddot{\mathbf{u}}_\mathbf{k} = -\vec{\nabla}_k U^{harm} = -\sum_{k' \neq k} (\mathbf{D}^{elastic}_{k,k'} + \delta_{k',k} \mathbf{D_k}^{spin}) \mathbf{u_{k'}} \tag{3.21}$$

we look for plane wave solutions:

$$\mathbf{u_k}(t) = \epsilon_k e^{i(\mathbf{KR}-\omega t)} \tag{3.22}$$

where $\mathbf{R}$ are the Brillouin lattice vectors, and ϵ_k are vectors which are identical for atoms which occupy the same point in different unit cells, i.e. $\epsilon_k = \epsilon_{k'}$ for $\mathbf{r_k} = \mathbf{r_{k'}} + \mathbf{R}$. Let N be the number of ions per unit cell, we then have to solve the set of 3N equations:

$$M_k\omega^2\epsilon_k = \sum_{k''=1}^{N} (\mathbf{D_{k,k''}}^{elastic}(\mathbf{K}) + \delta_{k'',k}\mathbf{D_k}^{spin})\epsilon_{k''} \tag{3.23}$$

where

$$\mathbf{D^{elastic}_{k,k''}}(\mathbf{K}) \equiv \sum_{\mathbf{R}} \mathbf{D}^{elastic}_{k,k'(\mathbf{R},k'')} \tag{3.24}$$

In these equations, the index k" denotes an ion inside the unit cell, and therefore it can vary from 1 to N, and l' indicates any other ion inside the crystal, thus $k' = k'(\mathbf{R}, k'')$. Let us compact Eq.3.23:

$$(\mathbf{D}^{elastic} + \mathbf{D}^{spin})\epsilon = \omega^2\epsilon \tag{3.25}$$

where the vector ϵ is composed by the vectors ϵ_k, $\mathbf{D}^{elastic}$ and $\mathbf{D}^{spin}$ are composed by the tensors $\frac{1}{M_k}\mathbf{D_{k,k''}}^{elastic}(\mathbf{K})$ and $\frac{1}{M_k}\mathbf{D_k}^{spin}$. Diagonalizing the tensor $\mathbf{D}^{elastic} + \mathbf{D}^{spin}$, one can obtain its eigenvalues, which are the square of the frequencies and its eigenvectors, i.e. the normal vibrational modes at the center of the Brillouin zone.

It is possible to separate the spin term contribution, considering that it is much weaker than the one from the elastic term. From Eq.3.23, one can obtain:

$$\omega_\alpha^2 = \hat{\epsilon}_\alpha \mathbf{D}^{elastic}\hat{\epsilon}_\alpha + \hat{\epsilon}_\alpha \mathbf{D}^{spin}\hat{\epsilon}_\alpha \tag{3.26}$$

where $\hat{\epsilon}_\alpha.\hat{\epsilon}_\alpha = 1$. Therefore, the change in the phonon frequency due to the spin-phonon coupling will be:

$$\Delta\omega_\alpha^{spin-phonon} = \frac{1}{2\omega_\alpha}\hat{\epsilon}_\alpha \mathbf{D}^{spin}\hat{\epsilon}_\alpha \tag{3.27}$$

It is therefore possible to obtain quantitative information about the magnetic correlations through the investigation of the phonon frequency as a function of temperature.

3.3 Experimental Setup

Fig,3.3 illustrates schematically the experimental setup for Raman Spectroscopy. The experimental setup is mounted on an optical table made up of granite, in order to avoid vibrations instabilities. Conventional Raman spectroscopy makes use of a continuum laser in visible light as the excitation source. Ar/Kr laser are widely used for that since they provide a significant number of possible wavelengths in the visible spectrum, and have high power. In particular, for this work, we used a wavelength of 487.99 nm, which is a blue line. The Ar laser emission is mostly in the blue and green line, while the Kr provides red and yellow wavelengths. Unfortunately, one drawback of this type of lasers is the presence of plasma lines, which arises from atomic transitions of the gases. This effect can be reduced by putting a pre-monochromator and an iris diaphragm. The pre-monochromator is also used in order to select an extremely fine wavelength, and it consists of a diffraction grating which disperses the non wished light coming in. The iris diaphragm will stop the unwished dispersed light. For polarized Raman spectroscopy, a polarization rotator is added just after the pre-monochromator. After that, the beam goes through a path consisting of mirrors and the beam needs to be focused on the sample: that is achieved by placing a lens with focus length of $f = 10$cm. The focused beam is incident on the sample with a spot size of ~ 200 μm in a quasi-backscattering geometry - the angle between the Poyinting vectors of incident and scattered beams is $\sim 160^\circ \pm 15^\circ$. The laser power on the sample is ~ 10 mW. The scattered light coming from the sample is captured by a commercial camera lens ($f = 8$ cm) which focus and send the beam into the spectrometer. For polarized Raman spectroscopy, a polarizer is placed in front of the spectrometer.

A schematic view of the Jobin Yvon spectrometer T64000 is depicted in Fig.3.4. The spectrometer can work on three different configurations: simple, double subtractive and triple additive. We used the double subtractive mode, where the first stage consists of two diffracting gratings with 1800 lines/mm which act as a filter, removing the elastic signal. The first slit width is ($S_1 = 200$ μm). The second slit is large ($S_2 = 2000$ μm). The third slit width is $S_3 = 100$ μm. The third grating disperses the filtered beam directly to an area detector-Charge coupled device (CCD) with 512×256 pixels, which is cooled with liquid Nitrogen. The signal is processed with the Software LabSpec.

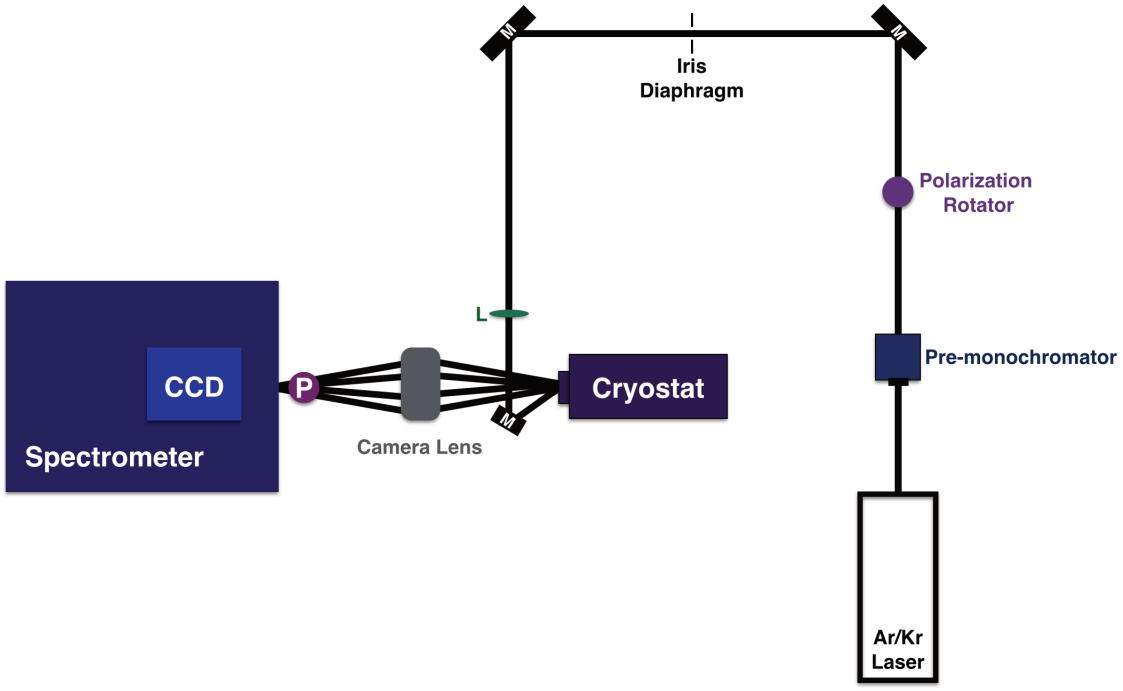

Fig. 3.3: Schematic experimental setup for Raman spectroscopy. M stands for mirror, L for lens and P for polarizer.

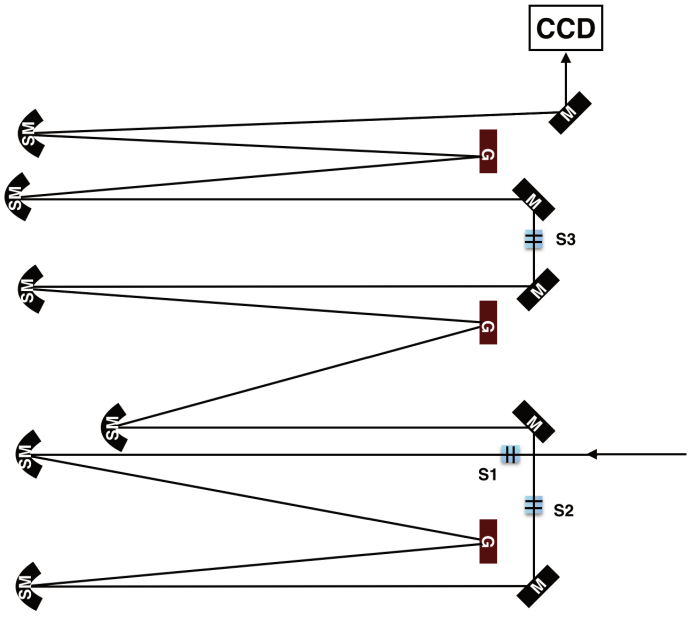

Fig. 3.4: Schematic view of the triple spectrometer. SM stands for spherical mirror, G is grating, M-mirror, S-slit.

Optical measurements are conducted on the sample placed in a closed-cycle helium cryostat (Advanced Research Systems). The sample space allows for optical access via an optical window. A copper finger is used for mounting the sample holder. The sample is glued on the evacuated cold finger with a Silver paint, in order to obtain a great thermal contact. A vacuum of the about 10^{-5} Torr is obtained with a turbomolecular pump (Edwards). The temperature is measured by a calibrated silicon diode sensor (accuracy of $\pm$ 12 mK) and controlled by a 100 Ω resistance heater anchored in the cold finger.

Chapter 4

Spin-$\frac{1}{2}$ chain $CuSb_2O_6$

This chapter presents a Raman scattering study of the layered Copper oxide $CuSb_2O_6$. This compound is a prototype of a low dimensional spin system which presents a spin-Peierls transition. Extensive theoretical and experimental studies have been performed in order to understand its unusual magnetic behavior. Firstly, an introduction to the scientific study will be presented. A preliminary characterization with X-ray diffraction was performed to determine the sample orientation and it has confirmed the presence of twinning and bicrystallinity. Further, our Raman scattering results will be discussed. Polarized Raman spectroscopy was used to determine the symmetry of the phonon modes. Most interestingly, the temperature dependence and lattice dynamical calculations are presented and its association with the magnetic properties will be addressed in a possible scenario for interpretations.

4.1 Crystal structure and magnetic properties

$CuSb_2O_6$ has a monoclinic trirutile crystal structure of space group $P2_1/n$ with lattice parameters $a = 4.6349$ Å, $b = 4.6370$ Å, $c = 9.2931$ Å and $\beta = 91.124^{\circ}$[49]. At $T \approx 390$ K, a second order phase transition from monoclinic β-$CuSb_2O_6$ to tetragonal α-$CuSb_2O_6$ takes place. The Cu^{2+} ions sits in the center of the octahedra with oxygens in their corners, as in Fig.2.2. Above ~ 390 K, dynamic Jahn-Teller effect is possibly realized in the tetragonal phase leading to fast dynamic exchange between the two different possibilities for elongation, resulting in average compressed octahedra. Below the phase transition, Jahn-Teller effect is leading to a CuO_6 elongated octahedra[12]. This structural phase transition is accompanied by a formation of crystallographic twins, which will be discussed in Section 4.3.1.

The spin-$\frac{1}{2}$ Cu^{2+} ions form a square lattice in the ab-plane and another Cu^{2+} ion is sitting in the center of the unit cell, and forming a square lattice with the same ion from neighboring

unit cells. The magnetic ion's outer 9 electrons are in the 3d shell, such that there is one unpaired electron lying in the e_g orbital. The angular momentum is quenched and therefore it has a moment composed only by spin $S = \frac{1}{2}$. Magnetic susceptibility on powder samples have confirmed it by fitting the experimental high temperature susceptibility with the Curie-Weiss law, obtaining $p_{eff} = 1.758\mu_B$[50], close to the expected value from Tab.2.2.

The magnetic cation sublattice is that of the K_2NiF_4, which includes many examples of square lattices exhibiting 2D antiferromagnetism, including La_2CuO_4. Surprisingly, as pointed out in the Introduction, this system presents a magnetic susceptibility which fits extremely well over a large temperature range to a Heisenberg $S = \frac{1}{2}$ 1D Bonner Fisher fit, with an exchange constant ranging from -86 K to -98 K [51, 52, 49, 53, 54]. Moreover, low temperature susceptibility measurements show a sharp drop at $T_N \approx 8.5$ K, indicating a transition to long range AFM order. This transition is believed to occur as a result of the dimerization of the spins, known as spin Peierls transition, which is caused by the coupling of one-dimensional Jordan-Wigner transformed fermions with the three-dimensional phonons. Thus, the contrast of the 2D lattice and the 1D magnetic behavior in this compound has been inferred as a result of an unusual orbital ordering, as better explained in the next Subsection 4.1.1.

The coupling strengths have been investigated[50] in β-$CuSb_2O_6$ by calculating the spin correlation interaction energies of two adjacent spins. A strong antiferromagnetic coupling is predicted to be along the [1 1 0] direction, i.e. the superexchange pathway is along the Cu-O-O-Cu bond, where the bond angle is 180°, as shown in Fig.4.1. The nearest neighbor interaction at z=0.5 is relatively smaller, and the Cu-O-Cu bond angle is close to 90°. The interchain-to-intrachain coupling ratio was estimated at 2×10^{-3}.

The reports on magnetic structure and magnetic susceptibility anisotropy are controversial. Neutron diffraction experiments revealed a long-range ordered magnetic structure at low temperatures with a magnetic propagation vector (1/2,0,1/2)[51, 53, 54] and a small ordered magnetic moment of $\sim 0.5\mu_B$ per Cu, suggesting that quantum fluctuations are present. Magnetic moments are aligned into ferromagnetic lines along the b-axis, and antiparallel along a and c-axis. Different orientations of magnetic moments with respect to crystal axes are reported in the literature. Another neutron powder diffraction study [51] has revealed spins to be in the ab-plane, but were not able to distinguish between collinear alignment of the spins at z=0 and z=0.5 and canted spins. Single crystal neutron diffraction studies have proposed magnetic moments canted away from the b axis towards the a axis with different canting at z=0 and z=0.5[54]. This canting was based on the magnetic susceptibility anisotropy published on the same paper. In contrast, two other single crystal neutron diffraction studies have shown that collinear antiferromagnetic order is realized with magnetic moments aligned along the b-axis,

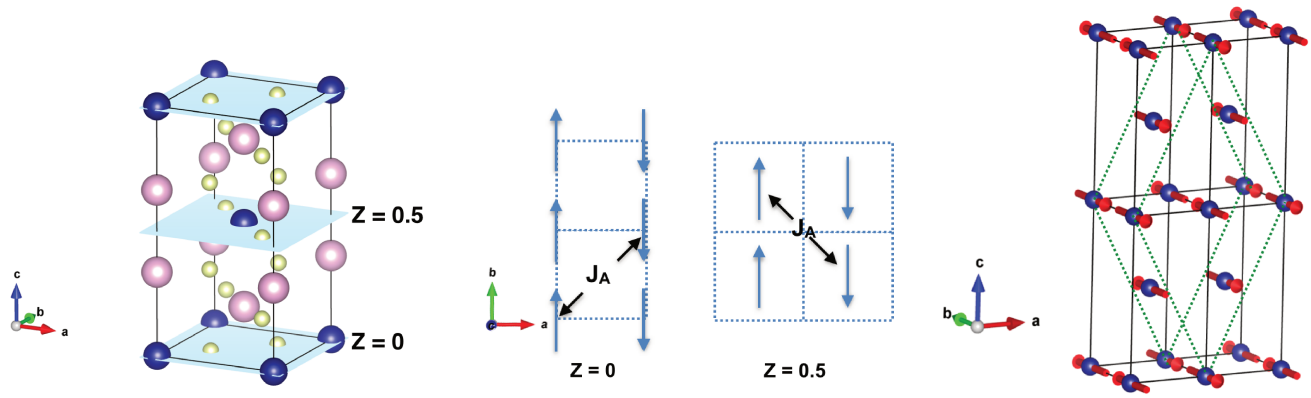

(a) (b) (c)

Fig. 4.1: a) Crystal structure of the α-$CuSb_2O_6$ showing the ab-plane (z=0) and the second Cu^{2+} at z=0.5. b) Correspondent magnetic couplings for z=0 and z=0.5. The superexchange pathway is along the Cu-O-O-Cu bond at z=0 and Cu-O-Cu at z=0.5. c) Magnetic unit cell at zero field at long-range order. [50, 53]

and this is shown in Fig.4.1(c)[50, 53].

Below the Néel temperature T_N, different magnetic susceptibility anisotropies are found in literature. Large decrease of susceptibility is observed when magnetic field is applied along the easy axis reported for the b axis direction[8, 55], a axis direction[49] and for both directions[6, 15, 54]. An abrupt change in the magnetization direction is observed when sufficient strong magnetic field is applied ($H_{SF} = 1.25T$) along both a and b directions, indicating an spin-flop transition. This suggests that both a and b are easy axes in this compound. Thus, one can conclude that the magnetically ordered state is still not completely established yet.

4.1.1 Proposed Orbital Ordering

The calculated band structure within the local (spin) density approximation (L(S)DA) is shown in Fig.4.2[5]. It shows two pair of bands crossing the Fermi level. This is a very unusual result for copper oxide materials, and in the standard cuprate scenario only one band crosses the Fermi level. Projecting the orbitals onto the band structure with a local coordinate system, it is possible to see that the broad pair of bands belongs to the $3d_{3z^2-r^2}$ and the narrow pair belongs to the $d_{x^2-y^2}$. This unusual band structure comes from the fact the CuO_6 octahedra are slightly distorted, as can be seen in Fig.4.2(b), so that the degeneracy in the e_g orbitals are only slightly lifted. The energy difference between the band centers of the out-of-plaquette and in-plaquette are about 0.3 eV, while in the standard cuprates, it is usually 2 eV.

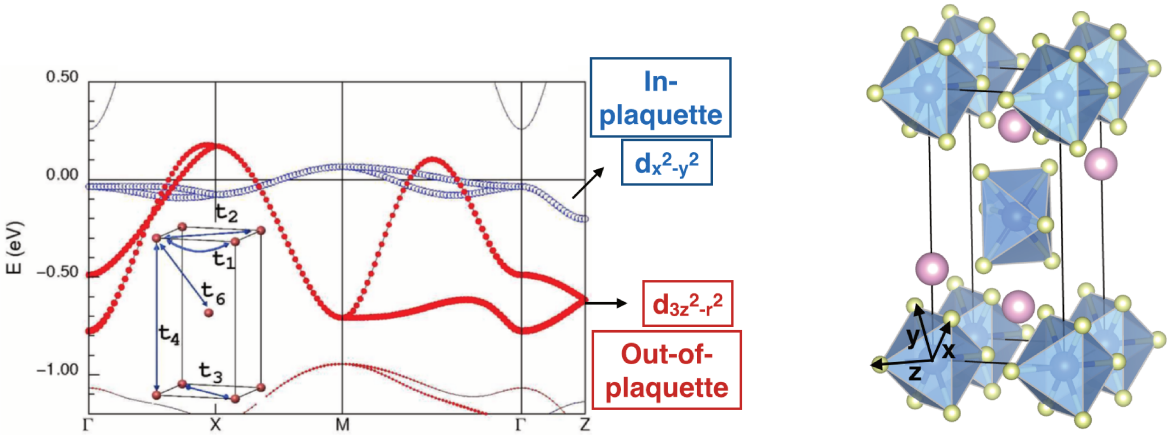

(a) (b)

Fig. 4.2: a) Calculated LDA band structure of the α-$CuSb_2O_6$. Taken from ref. [5] b) Crystal structure showing the local coordinate system: xy-plane is called plaquette.

The electronic calculation is therefore evidencing a strong competition between the two e_g orbitals. There are two possible ways to infer the one-dimensional order in this system:

- Scenario 1: the electronic interaction is mediated via the plaquette oxygens CuO_4, leading to a 1D ordering along the [1 -1 0] direction at z=0;
- Scenario 2: the electronic interaction is mediated by the out-of-plaquette oxygens, leading to 1D ordering along the [1 1 0] direction at z=0.

As pointed out before, we can already have an insight that the second scenario has to be the correct one to be in agreement with the neutron diffraction data. A tight-binding model fit was performed by the authors for both pairs of bands separately. The values of the hopping parameters are shown in Tab.4.1.

(meV)	t_1	t_2	t_3	t_4	t_5	t_6	t_7
$d_{x^2-y^2}$	-20	-	17.5	20.8	3.8	-	-1.86
$d_{3z^2-r^2}$	9.52	-197	-13.1	-3.86	-	-17.9	-
(K)	J_1	J_2	J_3	J_4	J_5	J_6	J_7
$d_{x^2-y_2}$	4.23	-	3.15	4.46	0.15	-	0.04
$d_{3z^2-r^2}$	0.93	400	1.76	0.15	-	3.32	-

Tab. 4.1: Hopping parameters and its correspondent coupling strengths obtained by a two-site-one-band TBM fit. The hopping paths are: t_1 (0 0 0) $\rightarrow$ (1 0 0), t_2 (0 0 0) $\rightarrow$ (1 1 0), t_3 (0 0 0) $\rightarrow$ (-1 1 0), t_4 (0 0 0) $\rightarrow$ (0 0 1), t_5 (0 0 0) $\rightarrow$ (1 0 1), t_6 (0 0 0) $\rightarrow$ $(\frac{1}{2}\frac{1}{2}\frac{1}{2})$, t_7 (0 0 0) $\rightarrow$ $(\frac{3}{2}\frac{1}{2}\frac{1}{2})$. Taken from ref.[5]

The exchange constants are obtained from the hopping integral value using Eq.2.32, where it was used an effective value for the Coulomb integral of $U_{eff} = 4.5$ eV. The hopping parameters obtained for the $d_{x^2-y^2}$ band are all similar in magnitude, implying that the interactions are approximately equal along all the main hopping paths t_1, t_2, t_3 and t_4. This is indicating a three-dimensional magnetic ordering, which is incompatible with the experimental data of magnetic susceptibility and neutron diffraction. The $d_{3z^2-r^2}$ band fit provided an exchange coupling J_2 which is much higher than the other ones, corresponding to hopping path t_2 which is along the [1 1 0] direction and so through the out-of-plaquette oxygens, which is compatible with the experimental neutron diffraction data. The calculated J_2 value is overestimated when compared to the experimental value (by a factor of four) due to possible ferromagnetic contributions.

In summary, the presence of a quite regular octahedra in the crystal structure introduces a competition between the e_g orbitals for the ground state in this compound, as depicted in Fig.4.3-a). Correlations drive the electronic structure to a unique $d_{3z^2-r^2}$ orbital ordering (Fig.4.3-c), which leads to a one-dimensional magnetic ordering.

Although electronic structure calculations and TBM fit performed in ref [5] have revealed an orbital ordering which drives the magnetic correlations to one-dimensional ordering, an experimental evidence of such orbital ordering is still missing in the literature.

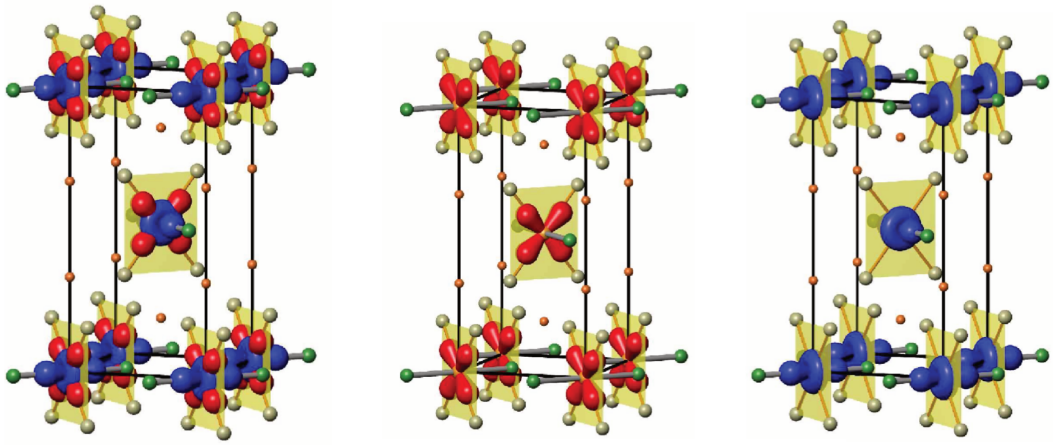

(a) (b) (c)

Fig. 4.3: a) Schematic view of the competition between the $d_{x^2-y^2}$ and $d_{3z^2-r^2}$ orbitals. b) Standard cuprate scenario, where the only orbital crossing the Fermi level is a $d_{x^2-y^2}$. c) Unique orbital ordering in $CuSb_2O_6$. Taken from ref. [5]

4.2 Single crystal growth

The samples were obtained in collaboration with Montana State University (USA) and were grown by the group of Professor John Neumeier and Aaron Christian. For the preparation of polycrystalline $CuSb_2O_6$, mixed powders of starting materials CuO and Sb_2O_3 were ground and pressed into pellets. In the first step, the temperature profile was 950°C for 12 h and in a second step reheated at 1000°C for 12h with intermediate grinding in a solid state reaction. The endothermic chemical vapor transport growth of $CuSb_2O_6$ single crystals with HCl $TeCl_4$ as transport agents was employed: $CuSb_2O_6$ powder and HCl or $TeCl_4$ were mixed and sealed in an evacuated quartz tube. The tube is inserted in a two-zone tube furnace with source-zone temperature of 900°C and growth zone temperature of 800° for 200 hours. The obtained crystals are green in color, indicating insulating behavior and one sample is shown in Fig.4.4.

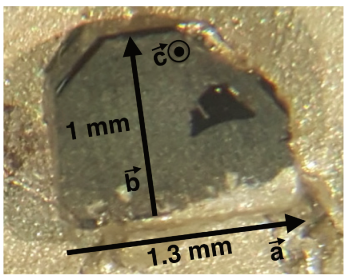

Fig. 4.4: $CuSb_2O_6$ single crystal obtained by the endothermic chemical vapor transport method.

4.3 Results

4.3.1 X-ray diffraction characterization

As mentioned in Section 4.1, characterizing crystals with X-ray diffraction (XRD) is essential to align the sample and for a better understanding of the crystal behavior because of its potential for bicrystallinity. Laue measurements and X-ray diffraction have shown that the sample orientation is the one indicated in Fig.4.4, [0 0 1].

The presence of two crystalline domains was not apparent upon visual inspection. However, it was apparent on polarized Raman scattering studies making it difficult to determine the symmetry of the normal modes. Twinning was observed through Laue images and XRD revealed bicrystallinity, as shown in Fig.4.5.

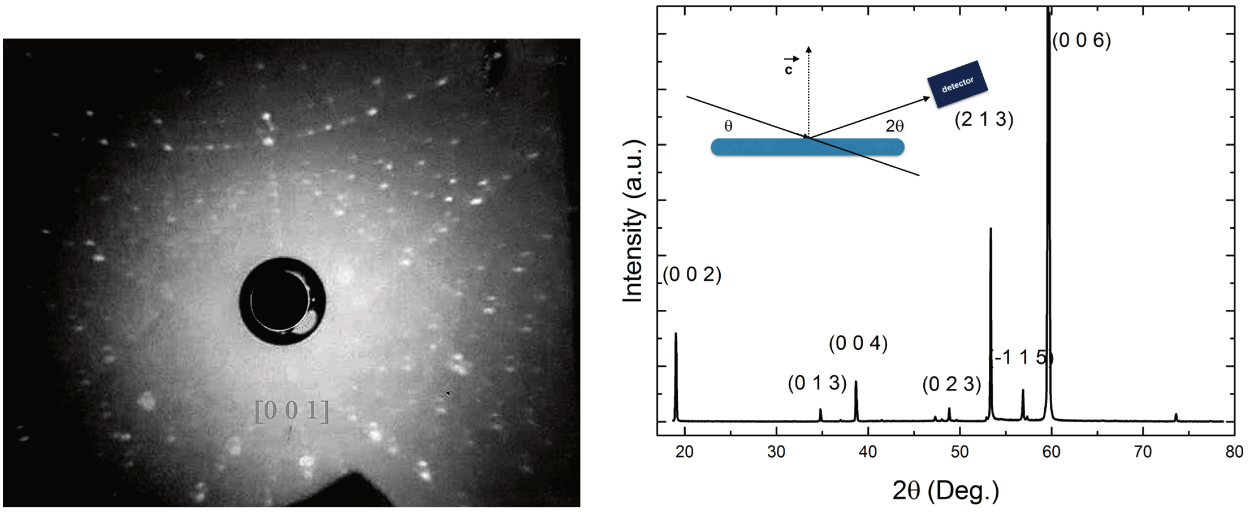

(a) (b)

Fig. 4.5: a) Laue pattern showing the orientation of the single crystal in the $\vec{c}$ direction and indicating twinned crystallites at room temperature, in the monoclinic phase. b) $\theta - 2\theta$ scan showing different domains for the sample.

The formation of two types of twinnings is observed for this compound: growth twinning, present even in the tetragonal phase, and multiple twinning associated with the structural phase transition, occurring as a result of two different choices for elongation of two crystallographic equivalent octahedra in the unit cell. Additionally, the existence of disoriented domains in the monoclinic phase was also observed. Further, the formation of bi-crystals is present as well.

4.3.2 Raman scattering study

Vibrational normal modes

The tetragonal trirutile α-$CuSb_2O_6$ crystal structure belongs to the space group $P4_2/mnm$ (136) and it presents two formula units per unit cell. Therefore, a total of 54 modes are expected to be present. The sites symmetries for Cu is 2a, for Sb is 4e, and for O are 4f and 8j. The factor group analysis is presented in Tab.4.2[1], and it corresponds to the following irreducible representations for the Raman active modes at the center of the Brillouin zone:

$$\Gamma = 4A_{1g} + 2B_{1g} + 4B_{2g} + 6E_g \tag{4.1}$$

Polarization	Raman Active modes	Expected number of phonon modes
-Z(YY)Z	A_{1g}	4
	B_{1g}	2
-Z(XY)Z	B_{2g}	4
-Z(Y'Y')Z	A_{1g}	4
	B_{2g}	4
-Z(X'Y')Z	B_{1g}	2

Tab. 4.2: Polarization rules for α-$CuSb_2O_6$. In this notation, the laser propagation direction at the entrance is -Z and at the exit is Z. The polarizations are indicated inside the parenthesis, and the first indicated value is the polarization at the entrance, while the second is exit polarization. X$||\vec{a}$, Y$||\vec{b}$ e Z$||\vec{c}$, where $\vec{a}, \vec{b}$ and $\vec{c}$ are the lattice vectors. The polarizations X' and Y' indicate 45 ° rotation with respect to the original polarizations X and Y around the Z-axis.

Fig.4.6 displays Raman spectra in different polarizations at 420 K.

[1]Appendix A addresses the selection rules calculations shown in Tab.4.2.

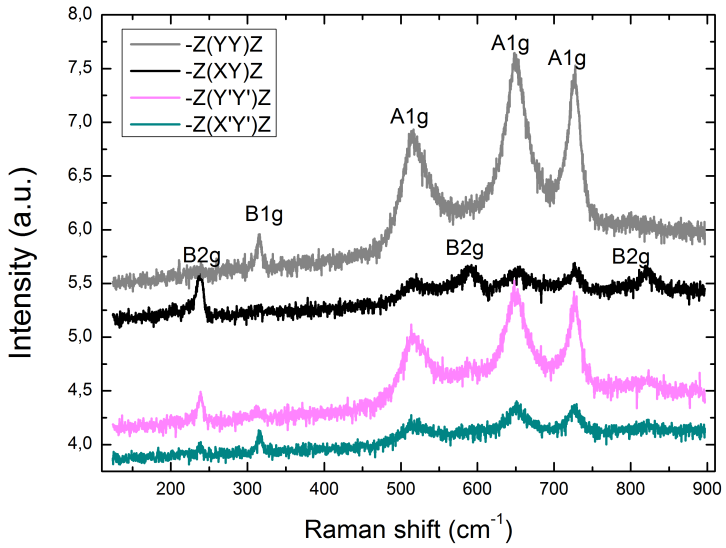

Fig. 4.6: Raman spectra of α-$CuSb_2O_6$ in different polarizations at T = 420 K.

Noticeably, the A_{1g} modes are not completely disappearing for crossed polarizations -Z(XY)Z and -Z(X'Y')Z as expected from the group factor analysis (Tab.4.2). This is ascribed to a twinning of the single crystal on a microscopic level and/or the presence of crystal domains with distinct orientations (bi-crystals), as discussed in Subsection 4.3.1. Nevertheless, it was possible to identify the symmetry of the modes, and a second confirmation is obtained with the simulated Raman Spectra from the lattice dynamical calculations, as it will be addressed in the next Subsection 4.3.2.

Ab-initio Lattice Dynamical calculation

The study of vibrational properties was done using Ab-initio methods of Density Functional Theory (DFT), with the Quantum Espresso code [56]. The electronic wavefunction was described using plane waves with kinetic energy cutoff 50 Ry, and the charge density cutoff was 300 Ry. The atomic inputs for each atomic position was taken from reference [57] and the values for the α-$CuSb_2O_6$ were used for simplicity. Exchange correlation effects were treated within the Generalized Gradient Approximation (GGA) with the functional proposed by Perdew-Burke-Ernzerhof. The Standard Solid State pseudo-potential (SSSP) is employed in this work. The phonon energies were calculated for the Γ point of the Brillouin zone, accessed by our Raman scattering experiment.

The calculations were performed in two steps. First, no relaxation of the structure was

performed and the experimental values for the atomic positions were used. The calculated frequencies for the observed vibrational modes in the first step are shown in Tab.4.3. In a second step, the structure was relaxed to its minimal energy configuration and the vibrational frequencies were calculated again, and they are shown in same table.

Mode symmetry	ω calculated in 1^{st} step	ω calculated in 2^{nd} step	ω Experimental value
A1g	503	456	515
	671	567	652
	744	624	729
B1g	284	290	316
B2g	246	218	240
	688	588	592
	843	703	825

Tab. 4.3: Comparison between the calculated frequencies in steps one and two of the ab-initio lattice dynamical calculations and experimental values.

The calculated frequencies in the first step are generally in better agreement with the experimental value than the ones obtained with relaxed structure, except for the B_{1g} mode and B_{2g} at $\omega_{exp} = 592$ cm^{-1}. The vibrational modes and their correspondent atomic displacements are schematically displayed in Fig.4.7 and Fig.4.8.

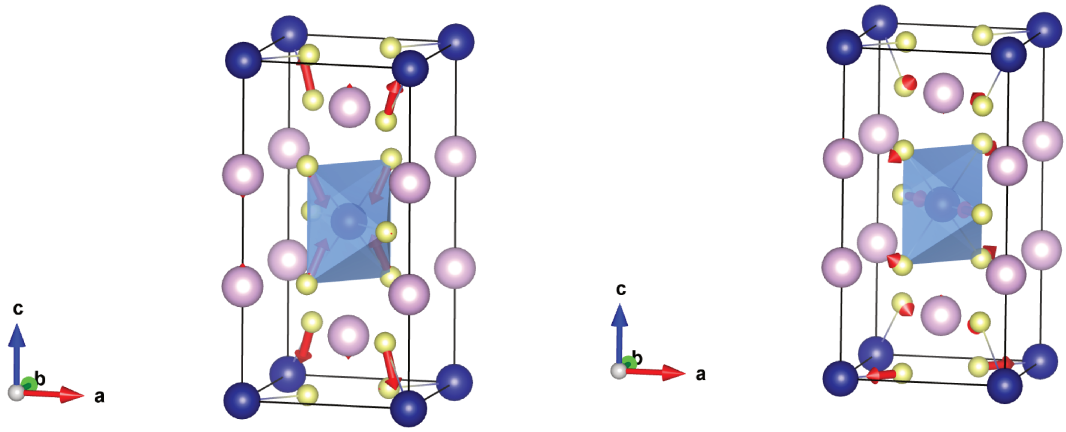

(a) $A_{1g} \sim 515$ cm^{-1} (b) $A_{1g} \sim 652$ cm^{-1}

Fig. 4.7: Schematic representation for each vibration observed in the Raman spectra as obtained within ab-initio lattice dynamical calculation [56].

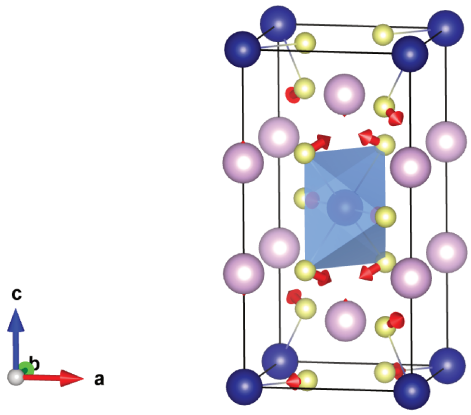

(a) $A_{1g} \sim 729$ cm^{-1}

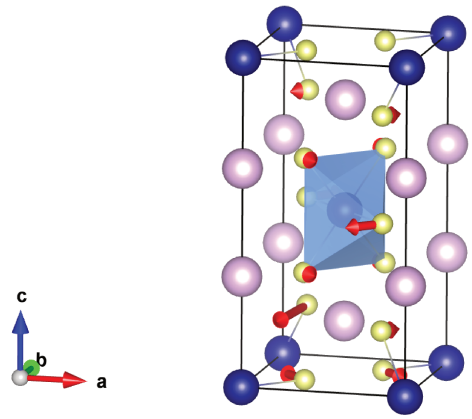

(b) $B_{1g} \sim 316$ cm^{-1}

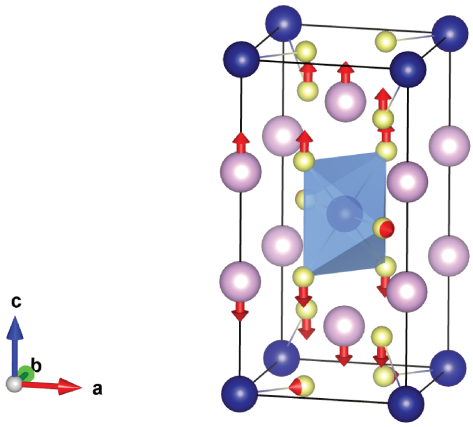

(c) $B_{2g} \sim 240$ cm^{-1}

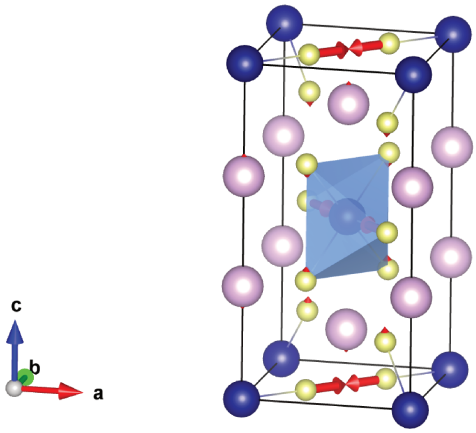

(d) $B_{2g} \sim 592$ cm^{-1}

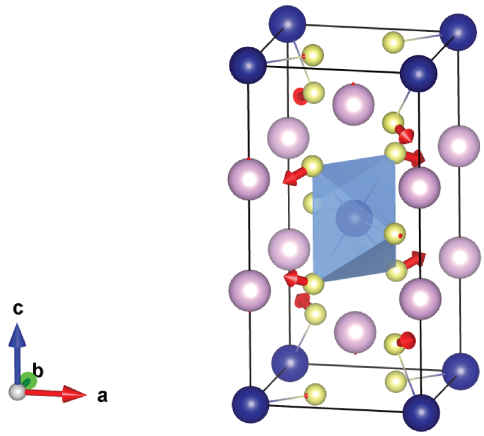

(e) $B_{2g} \sim 825$ cm^{-1}

Fig. 4.8: Schematic representation for each vibration observed in the Raman spectra as obtained within ab-initio lattice dynamical calculation [56].

The A_{1g} mode at ~ 515 cm^{-1} is a stretching vibrational mode of the oxygen atoms against copper in a breathing configuration. In the phonon mode at ~ 652 cm^{-1}, the in-plaquette oxygens vibrate in a different direction than the bonding one, and the upper oxygens vibrates in opposite directions. The out-of-plaquette oxygens vibrates along the bond in this mode. At ~ 729 cm^{-1}, vibrations of the out of plaquette against the Cu ion takes place, as well as upper in-plaquette oxygens vibrating in opposite directions. At ~ 316 cm^{-1}, there is a bending mode, where all oxygens vibrate in a direction different from the bonding. At ~ 240 cm^{-1}, there are Sb vibrations included and the oxygens in intermediary positions between z=0 and z=0.5 are vibrating along the c-direction. The oxygens at z=0 and z=0.5 are vibrating along the bond direction. The vibrational mode at ~ 592 cm^{-1}is a stretching mode where the out-of-plaquette vibrates along the bond direction and there is a small contribution of the in-plaquette oxygens vibrating agains each other in the c-direction. In the vibrational mode observed at ~ 825 cm^{-1}, the out-of-plaquette oxygens are vibrating along the bond and the in-plaquette oxygens vibrate in a direction that is not along their bonding to the copper atom inside the octahedra.

Structural phase transition

At $T_S \approx 397$ K, a second order structural phase transition takes place, and this can be seen in the Raman spectra as the emergence of a new intense peak at ~ 670 cm^{-1} at the β-$CuSb_2O_6$ phase shown in Fig.4.9.

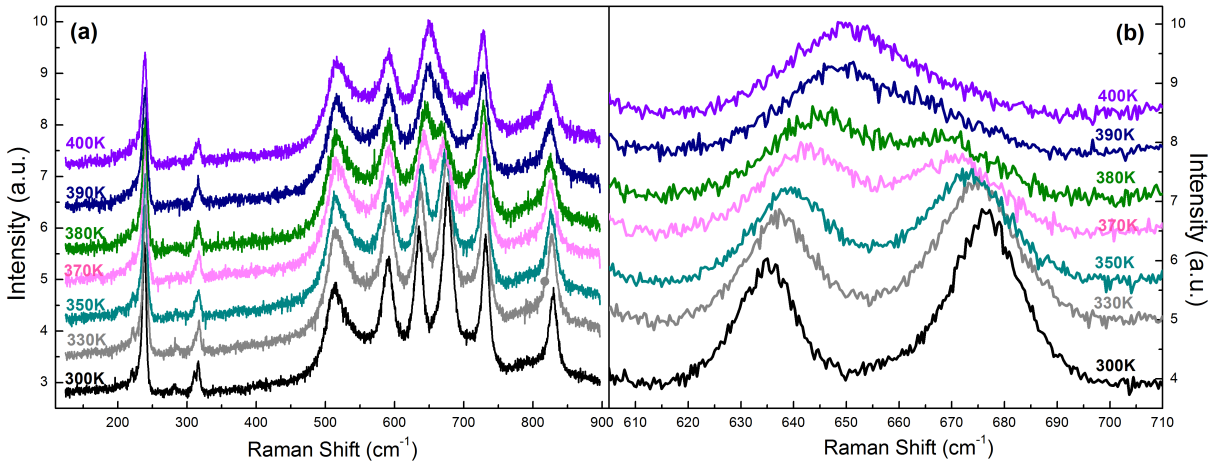

Fig. 4.9: a) Unpolarized Raman spectra at temperatures close to the structural transition α-$CuSb_2O_6 \Rightarrow \beta$-$CuSb_2O_6$. b) Evolution of the ~ 640 cm^{-1} and ~ 670 cm^{-1} modes which are sensitive to the structural lattice distortion.

Phonon frequencies of both peaks at ~ 670 cm^{-1} and ~ 640 cm^{-1} are plotted in Fig.4.10. One can notice that the behavior of these two peaks as a function of temperature indicate that

they are related, getting closer to each other at the transition.

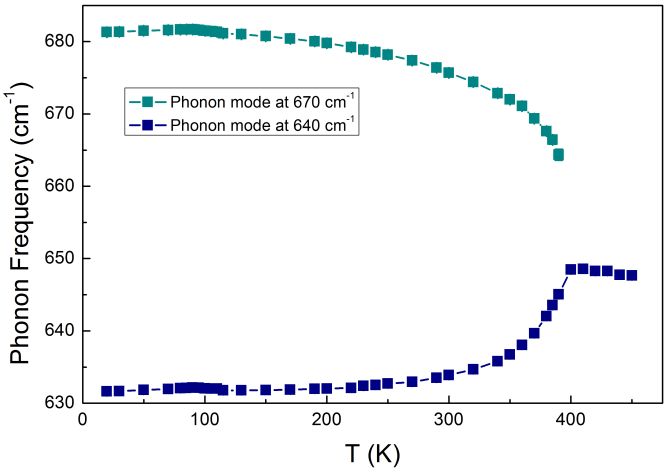

Fig. 4.10: Phonon frequencies of peaks at $\sim$ 670 cm^{-1} and $\sim$ 640 cm^{-1} as a function of temperature indicating that these peaks are correlated.

The intensity of peak $\sim$ 670 cm^{-1} divided by the intensity $\sim$ 640 cm^{-1} is plotted in Fig.4.11. One can note that this value is approaching zero, which indicates that the peak at $\sim$ 670 cm^{-1} is emerging in the Raman spectrum at T_S.

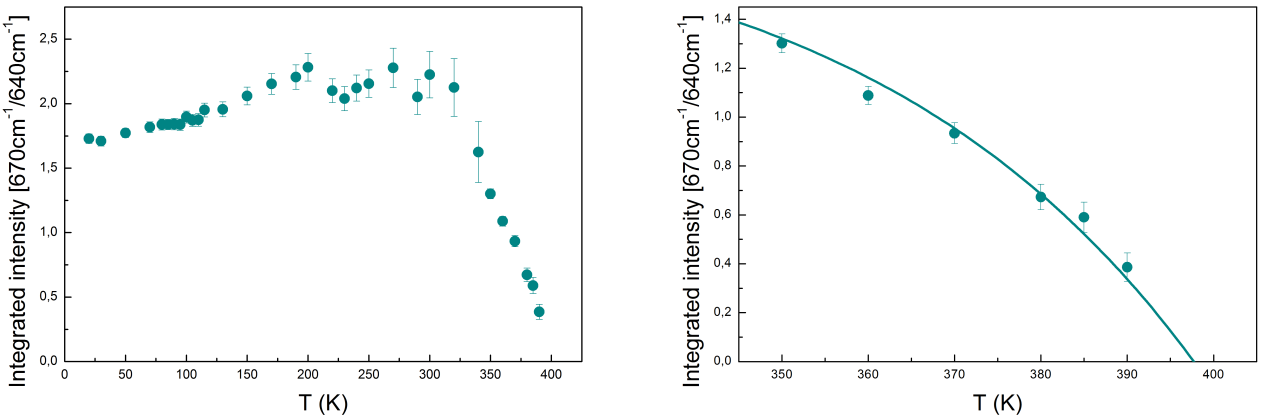

(a) (b)

Fig. 4.11: a) Integrated intensity of peak at $\sim$ 670 cm^{-1} divided by the integrated intensity of peak $\sim$ 640 cm^{-1} as a function of temperature is graphed in order to investigate if peak at $\sim$ 670 cm^{-1} is emerging at the structural phase transition. b) Zoom of Graph depicted in a) showing a transition temperature of $T_S = 397(3)$ K. The solid line is to guide the eye.

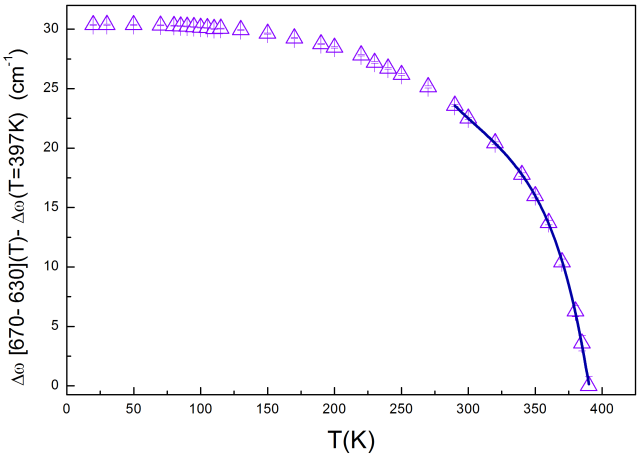

Fig. 4.12: Temperature dependence of the phonon frequency difference of peaks at ~ 670 cm^{-1} and ~ 640 cm^{-1} minus the difference at the phase transition at $T_S \approx 397$ K. The solid line is a polynomial fit. Notice that this quantity is decreasing continuously to zero at the phase transition, emphasizing its second order phase transition feature.

In addition, the temperature dependence of the phonon frequency difference of peaks at ~ 670 cm^{-1} and ~ 640 cm^{-1} minus the difference value at the transition temperature is plotted in Fig.4.12. One can notice that this quantity is rising from zero below the critical temperature $T_S \approx 397$ K and therefore it looks like an order parameter of a second order phase transition.

Temperature dependence of phononic excitations

In order to investigate the spin correlations, as explained in Chapter 3, several spectra in different temperatures were taken and are shown in Fig.4.13. Let us follow the behavior of each peak as a function of temperature.

Upon cooling, several distinctive features show up. First, several new phonon modes become visible in the spectra. At $T \approx 160$ K, a phonon mode at ~ 435 cm^{-1} appears, and at $T \approx 200$ K, we see two additional modes at ~ 658 cm^{-1} and ~ 705 cm^{-1}. In addition, almost all phonon modes become sharper and more intense, as depicted in Fig.4.13 for the phonon mode at 825 cm^{-1}.

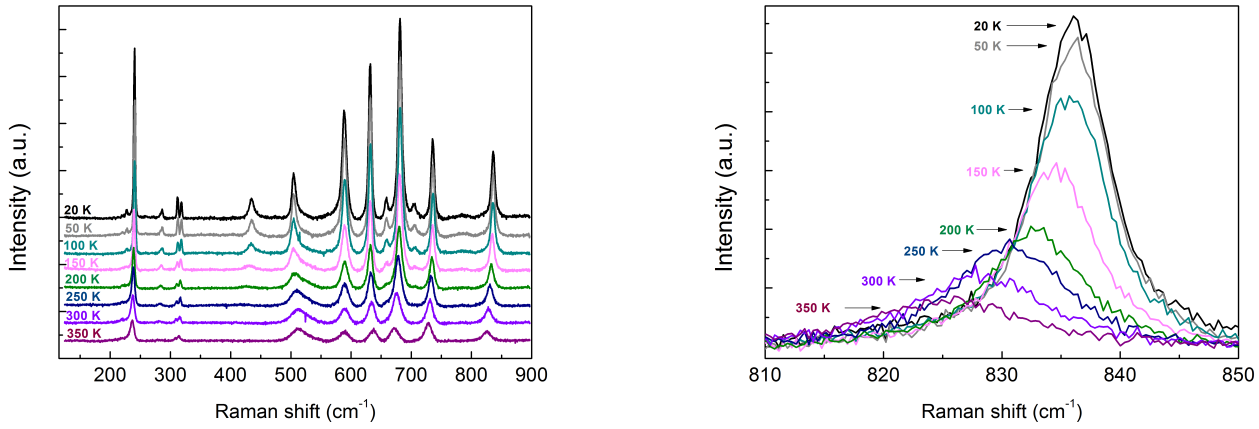

(a) (b)

Fig. 4.13: a) Unpolarized Raman spectra with incident beam direction along $\vec{c}$ crystallographic axis in different temperatures. b) Evolution of the ~ 825 cm^{-1} mode.

Several phonon modes undergo a substantial shift in energy, as depicted for each specific mode in the next graphs. Let us concentrate on the behavior of each phonon as a function of temperature. Each phonon mode is then fitted considering the Pseudovoigt function, which is a combination of the Lorentzian and Gaussian functions. The error bars included in the following graphs are purely statistical and come from the fitting process. The error in temperature can be considered as 1 K and it is not displayed in the figures.

The temperature dependence of the ~ 825 cm^{-1} mode is graphed in Fig.4.14. With decreasing temperature from 350 K, this mode undergoes an appreciable hardening of approximately 10 cm^{-1} and then is saturates around $T \approx 115$ K. Upon cooling, there is a tiny jump at $T \approx 110$ K.

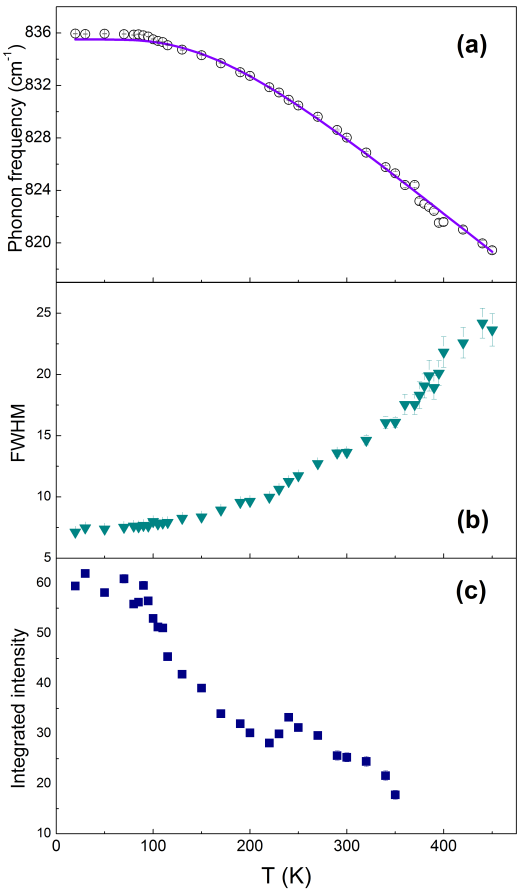

Fig. 4.14: Temperature dependence of (a) the phonon frequency (b) peak width and (c) integrated intensity of the ~ 825 cm^{-1} phonon mode.

The violet line is a fitting down to 115 K and extrapolated to lower temperatures considering the anharmonic decay of optical phonons processes which includes higher order terms involving cubic and quartic anharmonicity[58] rather than Eq.2.63:

$$\omega(T) = \omega_0 + A\left(1 + \frac{2}{e^{\frac{\hbar\omega_0}{2k_BT}} - 1}\right) + B\left[1 + \frac{3}{e^{\frac{\hbar\omega_0}{2k_BT}} - 1} + \frac{3}{(e^{\frac{\hbar\omega_0}{2k_BT}} - 1)^2}\right] \tag{4.2}$$

where ω_o is the phonon frequency, A and B are adjustable parameters.

It is possible to notice that the extrapolation of the fit to lower temperatures is fitting quite well. It is noticeable that there is a considerable broadening of the phonon and a decrease of the integrated intensity as the temperature increases.

The next mode depicted in Fig.4.15 shows the behavior of the vibrational mode at ~ 729 cm^{-1}. Upon cooling, again there is an increase of the phonon frequency until it saturates at about $T \approx 115$ K. Upon further cooling, they slightly soften while showing a tiny jump at 110

K. It should be noted that this softening takes place for temperatures whose energy scale is comparable to the low dimensional exchange constant $J \sim 105$ K and where the Curie law is reported to deviate due to the low dimensional behavior[6]. Such an anomalous evolution of phonon modes has been interpreted in terms of spin-phonon coupling.

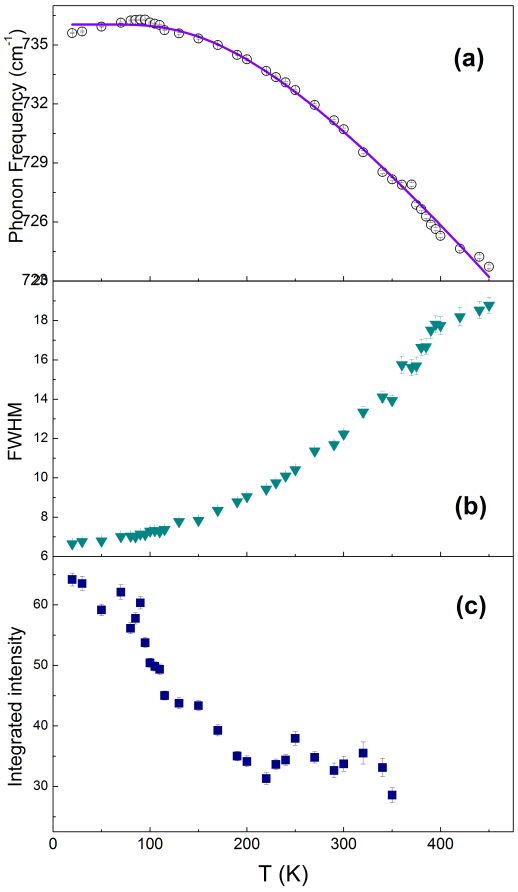

Fig. 4.15: Temperature dependence of (a) the phonon frequency (b) peak width and (c) integrated intensity of the ~ 730 cm^{-1} phonon mode.

A similar behavior is observed for the phonon at ~ 677 cm^{-1}, as shown in Fig.4.16. Notice that this phonon is also sensitive to the structural transition, as discussed in Section 4.3.2.

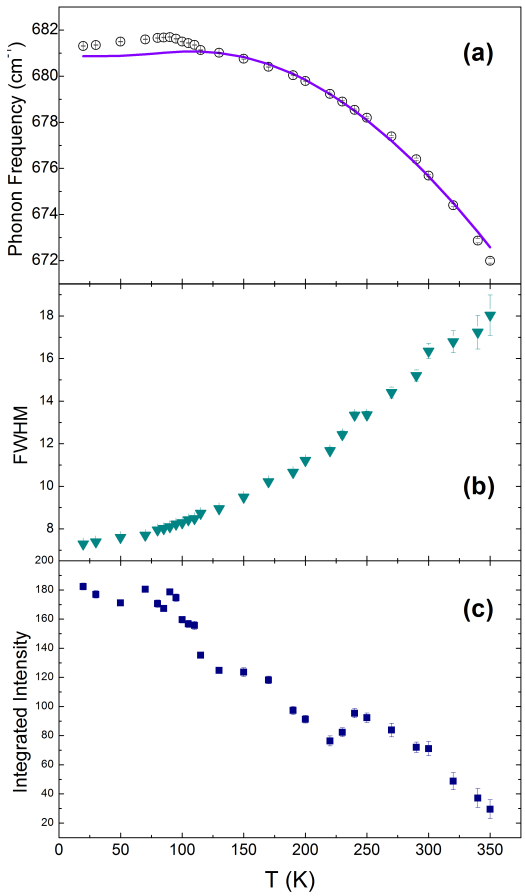

Fig. 4.16: Temperature dependence of (a) the phonon frequency (b) peak width and (c) integrated intensity of the ~ 677 cm^{-1} phonon mode.

The temperature dependence of the frequency for the phonon mode at ~ 635 cm^{-1} shows a softening upon cooling in all the entire measured temperature range. Again, an anomaly associated with the spin-phonon coupling is showing up at $T \approx 110$ K, where the frequency slightly shifts towards a higher value and then it softens more. This is the second mode participating in the structural phase transition. It should be noted that the phonon broadening effect with increasing temperature as well as the decrease in the integrated intensity can be observed for this phonon as well.

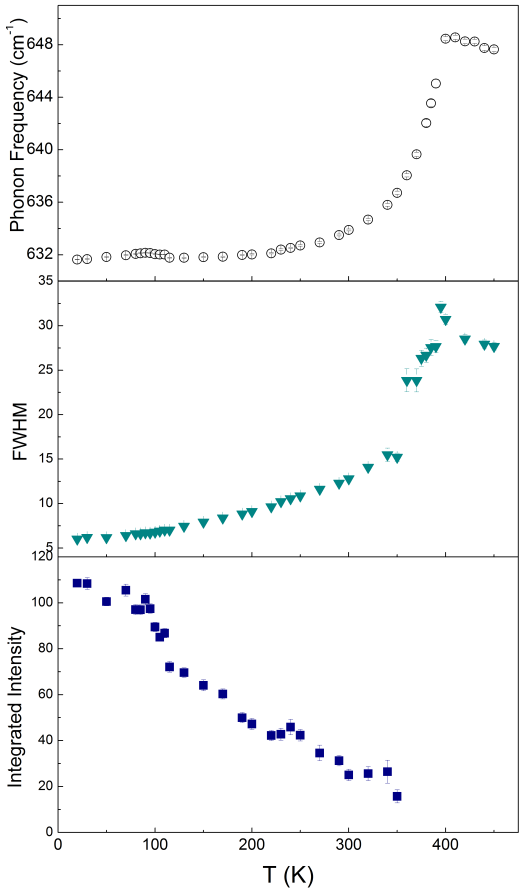

Fig. 4.17: Temperature dependence of (a) the phonon frequency (b) peak width and (c) integrated intensity of the ~ 635 cm^{-1} phonon mode.

The phonon mode at ~ 589 cm^{-1}, shows a tiny hardening upon cooling from 450 K down to 115 K of approximately 1.2 cm^{-1}, where it starts softening after a jump at 110 K. The size of the anomaly associated with the low dimensional behavior compared to the energy size of the anharmonic decay is the highest of spectra. The width is increasing and the integrated intensity is decreasing with increasing temperature.

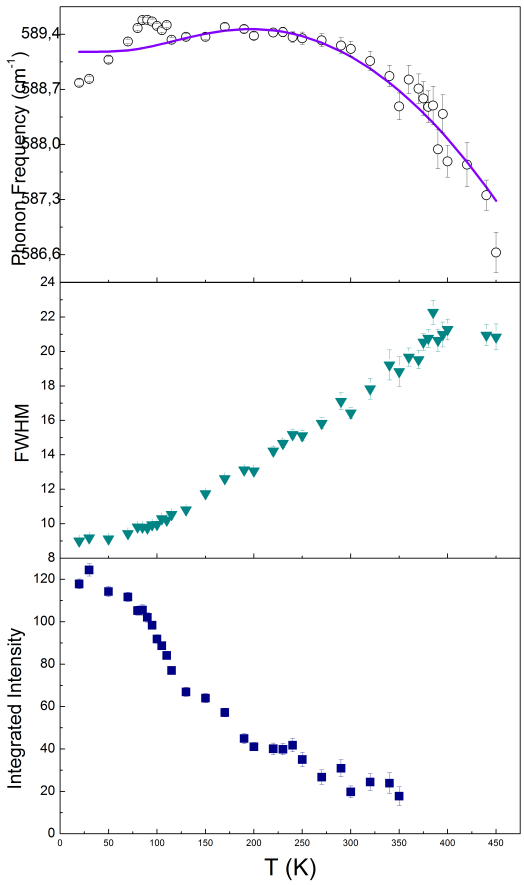

Fig. 4.18: Temperature dependence of (a) the phonon frequency (b) peak width and (c) integrated intensity of the ~ 589 cm^{-1} phonon mode.

An even more intriguing behavior is taking place for the phonon mode at ~ 515 cm^{-1}. Upon cooling, an anomalous softening of the order of 10 cm^{-1} is occurring. At $T \approx 110$ K, a slight increase in frequency is taking place. A pronounced Fano asymmetric line shape is observed for this mode, which suggests an interference between the phonon and the electronic excitations.

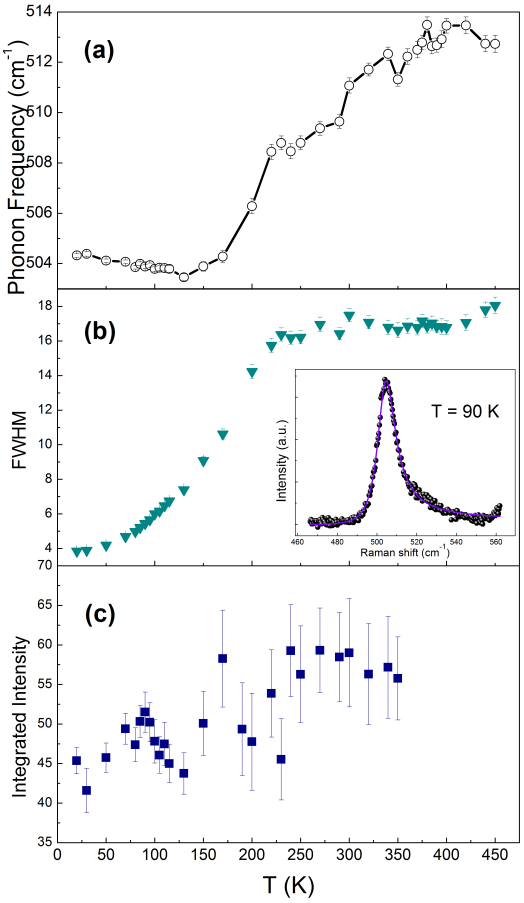

Fig. 4.19: Temperature dependence of (a) the phonon frequency (b) peak width and (c) integrated intensity of the ~ 515 cm^{-1} phonon mode. In the inset of b), a fit of the Fano line shape (violet line) -Eq.4.3 to the phonon mode (circles) for $T = 90$ K.

Therefore, this peak was fitted using a Breit-Wigner Fano line shape[59]:

$$I = I_0 + H\frac{(1 + \frac{\omega-\omega_0}{q\Gamma})^2}{1 + (\frac{\omega-\omega_0}{\Gamma})^2} \tag{4.3}$$

where I_0 is an offset, ω_0 is the phonon frequency, H is height, Γ is the width and q is the asymmetry parameter.

In addition, with increasing temperature, the broadening of the phonon is taking place up to approximately 240 K where it saturates. The temperature where this second anomaly manifested in the phonon width occurs is not associated to spin-phonon coupling and neither to any transition temperature reported in the literature.

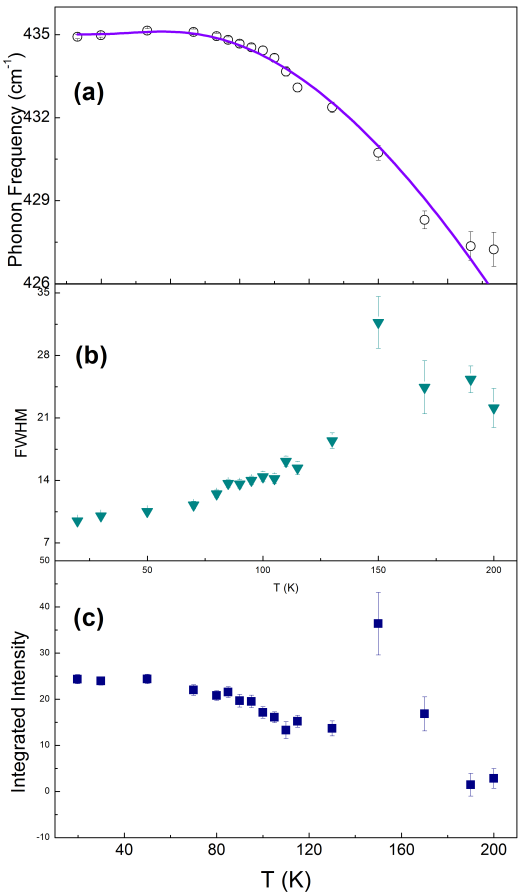

Fig. 4.20: Temperature dependence of (a) the phonon frequency (b) peak width and (c) integrated intensity of the ~ 429 cm^{-1} phonon mode.

Fig.4.20 shows the evolution of the vibration at ~ 429 cm^{-1} as a function of temperature. It is possible to notice that this vibration does not show spin-phonon coupling and the phonon exists until approximately 200 K.

The phonon modes at ~ 311 cm^{-1} and ~ 318 cm^{-1} are depicted in Fig.4.21. These two phonon modes present very similar behavior: spin-phonon coupling occurring for $T < 110$ K, phonon broadening effect and a decrease in the integrated intensity with increasing temperature.

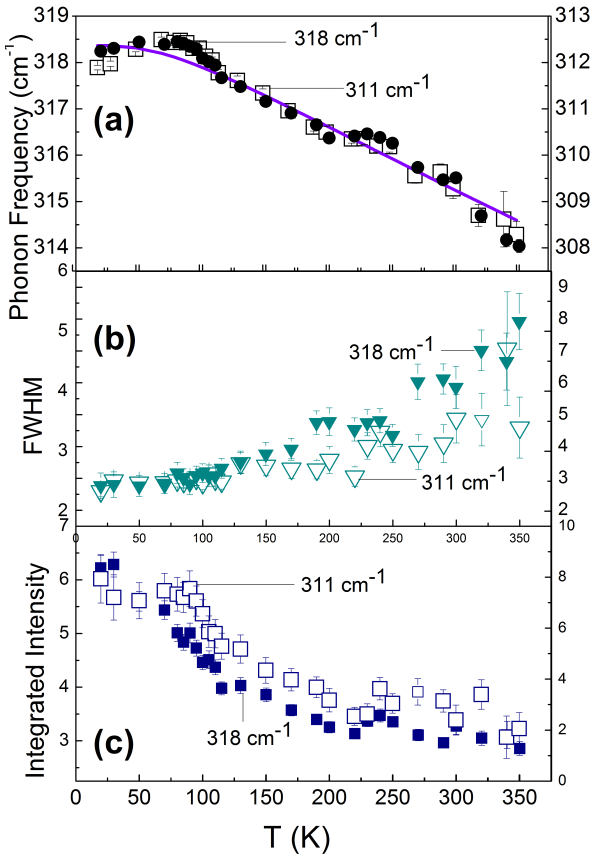

Fig. 4.21: Temperature dependence of (a) the phonon frequency (b) peak width and (c) integrated intensity of the ~ 311 cm^{-1} and ~ 318 cm^{-1} phonon modes.

The phonon mode at ~ 285 cm^{-1} is shown in Fig.4.22. It is possible to notice that at $T \approx 115$ K there is a distinct jump from the anharmonic decay at the temperature associated with the one-dimensional behavior from the magnetic susceptibilities due to the renormalization of the phonon energy via spin-phonon coupling.

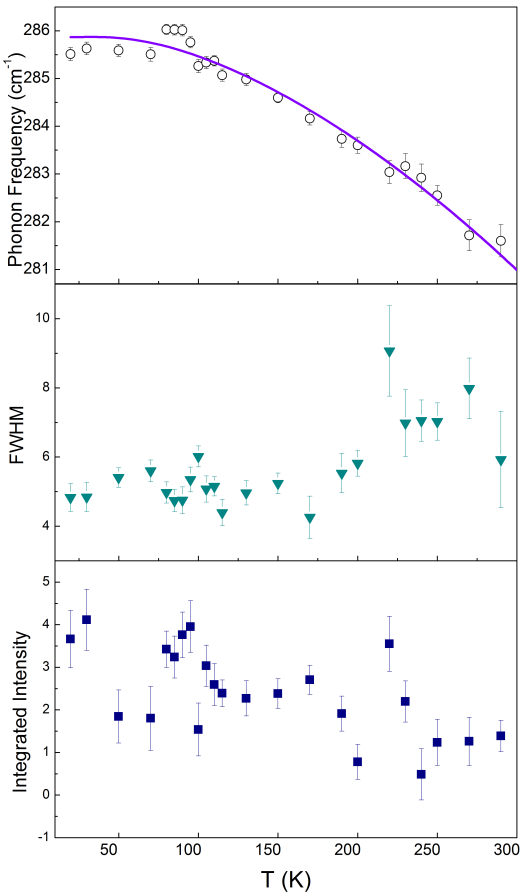

Fig. 4.22: Temperature dependence of (a) the phonon frequency (b) peak width and (c) integrated intensity of the ~ 285 cm^{-1} phonon mode.

The phonon mode at ~ 240 cm^{-1} is depicted in Fig.4.23. Upon cooling, a hardening of approximately 6 cm^{-1} until $T \approx 115$ K is followed by a jump of approximately 1 cm^{-1} and a softening of this jump for lower temperatures. This anomaly is again due to spin-phonon coupling.

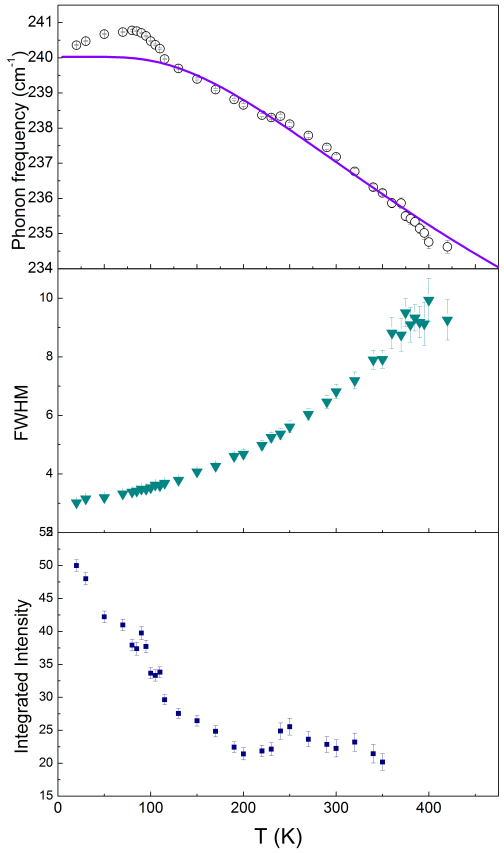

Fig. 4.23: Temperature dependence of (a) the phonon frequency (b) peak width and (c) integrated intensity of the ~ 240 cm^{-1} phonon mode.

4.4 Discussion

The intriguing structural transition signature in the Raman spectra is the emergence of a new phonon mode at ~ 670 cm^{-1} in the β phase ($P2_1/n$). This phonon mode not only appears in this phase due to the symmetry change, but is also related to a previous phonon mode at ~ 640 cm^{-1} (Fig.4.10). Moreover, an explanation stating degenerate modes which would split into two when the symmetry breaks is not satisfactory, because this would in turn lead to equal intensities for the two split peaks close to T_S.However, from Fig.4.11 b), one can see that the phonon mode at ~ 670 cm^{-1} is approaching zero intensity at the phase transition, and thus we can infer the transition temperature as ≈ 397 K.

One possible interpretation to explain this intriguing behavior is depicted in Fig.4.24.

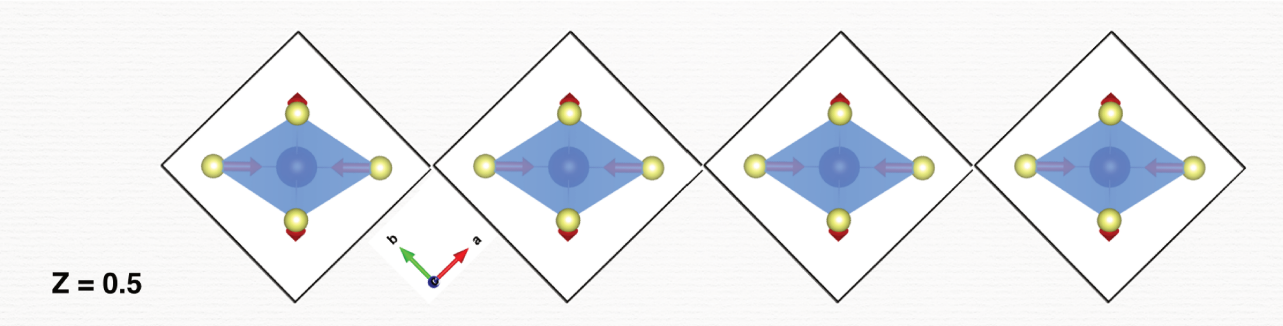

(a) Neighboring octahedra vibrate in phase in the ~ 640 cm^{-1} phonon mode.

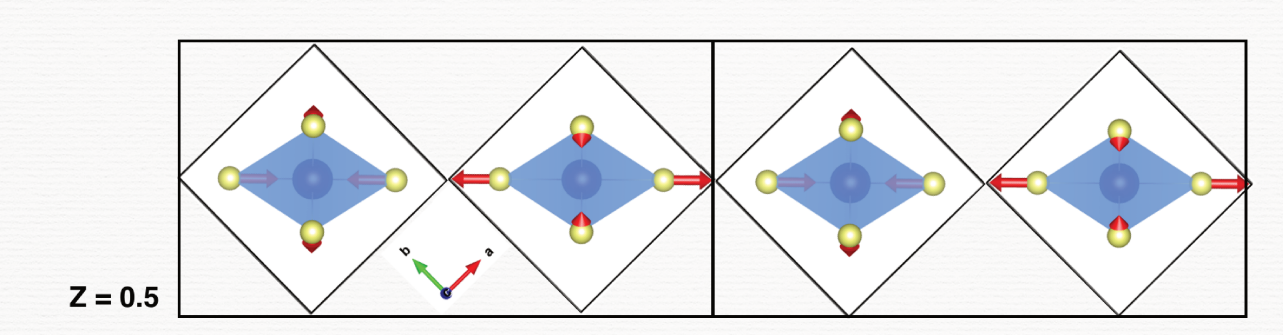

(b) Neighboring octahedra vibrate out of phase in the ~ 670 cm^{-1}.

Fig. 4.24: Tentative asignment of the ~ 670 cm^{-1} peak in the monoclinic phase and its relation with the ~ 640 cm^{-1} mode. According to this picture, both modes belong to the same phonon branch; the ~ 640 cm^{-1} mode is in the center of the Brillouin zone, while the ~ 670 cm^{-1} would be in the edge of the tetragonal Brillouin zone, and therefore would be forbidden for Raman scattering. In the monoclinic phase, the ~ 670 cm^{-1} mode would become zone-center (and Raman-active) due to a possible folding of the Brillouin zone associated with a doubling of the unit cell in the low-symmetry phase.

From lattice dynamical calculations, the phonon mode at ~ 640 cm^{-1} involves a vibration of the out-of-plaquette oxygens against the ion Cu^{2+}, and a small contribution of the in-plaquette oxygens in opposite directions in the ab-plane. A possible explanation to state that the two split phonon modes are related is if their vibrations involve the same type of motion. However, since they are not the same phonon, we propose that in the peak at ~ 640 cm^{-1}, octahedra in neighboring unit cells vibrate in phase, and at ~ 670 cm^{-1}, neighboring octahedra vibrate out-of-phase. The second type of vibration depicted in Fig.4.24 b) would correspond to a phonon mode at the border of the Brillouin zone. As a result, this vibration can only be Raman active if there is a doubling of the unit cell and a consequent folding of the Brillouin zone.

Notice that, if the neighboring CuO_6 octahedra in the [110] direction were entirely independent (i.e., no coupling between neighboring oxygen ions in this direction), the two modes depicted in Fig.4.24 would have exactly the same eigenfrequency, since they would represent

the same CuO_6 molecular vibration. On the other hand, a non-zero harmonic coupling energy between these oxygens leads to a dispersion of this phonon branch and to distinct energies of the modes shown Fig.4.24. Thus, the largely increased energy separation between these two modes in the monoclinic phase (see Fig.4.10) indicates a larger dispersion of this phonon branch for $T < T_S$, which seems to indicate an enhanced connectivity of the Cu-O-O-Cu linear chains. This result may be linked directly to the 1D magnetism observed at lower temperatures, since such enhanced connectivity is most likely the result of the orbital ordering of the Cu $d_{3z^2-r^2}$ electrons below T_S, enhancing the electronic density, hybridization and exchange coupling energy along the Cu-O-O-Cu chain direction. In order to confirm this hypothesis, a perspective for this work is to perform XRD to find superlattice Bragg peaks.

Another intriguing behavior which occurs in this system is the frequency and width anomaly at 240 K for the phonon mode at ~ 515 cm^{-1}. Its Fano line shape indicates that an interference between the phonon and the electronic excitations is taking place. One possible excitation which might be occurring is an orbital flip, since this mode involves a vibration of the in plaquette oxygens against Cu^{2+}, as depicted in Fig.4.25. Further studies are necessary to elucidate the remarkable behavior of this phonon mode.

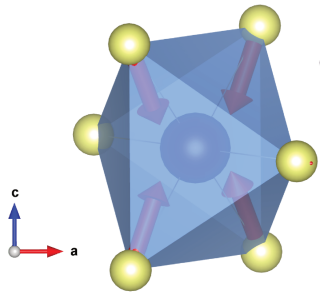

Fig. 4.25: Schematic view of the normal vibration in the octahedra for the phonon mode at ~ 515 cm^{-1}.

4.5 Partial conclusions

In summary, we have presented a Raman scattering study as a microscopic sensitive probe of magnetism on the one-dimensional antiferromagnet $CuSb_2O_6$. Its antiferromagnetically ordered state is still not satisfactorily understood, although a theoretical study proposed that the quasi one-dimensional behavior is being driven by an unusual orbital ordering. An experimental evidence of such orbital ordering was still missing in the literature. Multiple crystallographic twins were detected using both X-ray diffraction and Raman. Despite the twins, it was possible to identify the symmetry of the modes and ab-initio lattice dynamical calculations were

also performed and the calculated frequencies were fairly consistent with the measured values, helping in the mode identification. An structural phase transition from the highest symmetry α-$CuSb_2O_6$ to the lowest symmetry phase β-$CuSb_2O_6$ at $T \approx 397$ K is manifested as the appearance of a new phonon mode at ~ 670 cm^{-1}. Since the emergent peak is not only emerging but is related to its neighboring phonon mode at ~ 640 cm^{-1}, and since they are not degenerate modes, we suggest that they come from the same type of vibration but with central octahedra vibrating out-of-phase for neighboring unit cells. Thus, we suggest a doubling of the unit cell in the monoclinic structure, which remains to be confirmed by X-ray diffraction. Furthermore, we suggest this structural transition is also associated with an orbital ordering of the Cu^{2+} $d_{3z^2-r^2}$ orbital. Indeed, lattice dynamical calculations reveal that this vibration includes a motion of the oxygens out-of-plaquette against the Cu ion. As a perspective for this work, an investigation of superstructure peaks with X-ray diffraction will be performed.

In order to investigate the low dimensional behavior, several spectra were taken at temperatures between 20 K and 450 K. It was possible to observe a softening of some phonon modes at temperatures $T \approx 110$ K whose energy scale is comparable to the low dimensional exchange constant J. Such an anomalous evolution has been interpreted in terms of a renormalization of the phonon energy via spin-phonon coupling. In addition, we observed a width anomaly for a stretching mode at ~ 515 cm^{-1} at $T \approx 210$ K, which could not be attributed to spin-phonon coupling. Since this phonon has a Fano line shape, an interference between the electronic excitations and the phonon is believed to be taking place. As a possible scenario, we suggest this anomaly is associated to an orbital flip from the $d_{3z^2-r^2}$ and $d_{x^2-r^2}$, since the phonon includes a strong vibration of the in-plaquette oxygens against copper. As a perspective, we suggest to apply pressure on this system, since this can possibly flip the balance between the two competing orbitals and decouple the phonon and the orbital excitation.

Our results nicely demonstrate how Raman spectroscopy can be used to investigate magnetic properties of low-dimensional antiferromagnets.

Chapter 5

Spin-$\frac{3}{2}$ system $CoSb_2O_6$

In this chapter, we report Raman scattering measurements of the low-dimensional antiferromagnet $CoSb_2O_6$. Firstly, an introduction to the scientific case will be addressed. In addition, our Raman scattering results will be discussed: polarized Raman spectroscopy was used to identify the symmetry of the phonon modes; temperature dependence measurements and its association to magnetic properties are presented.

5.1 Crystal Structure and magnetic properties

$CoSb_2O_6$ crystallizes in a tetragonal trirutile structure with space group $P4_2/mnm$ and lattice parameters $a = 4.6495$ Å and $c = 9.2763$ Å [14]. It is an electrical insulator and the electrical conductivity is $\leq 10^{-7}(\Omega cm)^{-1}$ at 295 K[60]. Long-range order occurs below Néel temperature $T_N = 13.45$ K, and the magnetic susceptibility data from reference[14] appears consistent with a two-dimensional Ising model. The magnetic structure displays superexchange pathways along the [1 1 0] direction, i.e. along the Co-O-O-Co bonds, and the proposed magnetic structure is similar to the one proposed to $FeTa_2O_6$. However, two different magnetic structures have been proposed for the latter compound[14]. One of the proposed structures is identical to the two-sublattice model described in Chapter 4 - section 4.1, and this is apparently the most appropriate one for $CoSb_2O_6$. In contrast to the two dimensional Ising model from reference[14], anisotropic magnetocaloric effect has revealed the presence of one-dimensional magnetic chains[15], and this seems to be the most widely accepted scenario at present. So far, there are no estimates for $J/J_\perp$ for $CoSb_2O_6$. In contrast to the case of $CuSb_2O_6$, there are no band structure calculations revealing the driving force which leads to one-dimensional chains for $CoSb_2O_6$.

At the ordering temperature, long range AFM phase transition revealed as a rapid drop

in the magnetic susceptibility has been interpreted as a spin-Peierls transition[37], although theory has not provided strong conclusions regarding the existence of this type of transition in $S = \frac{3}{2}$ systems. However, there are qualitative arguments [61] regarding the possible existence of dimers in this kind of systems. The spin gap observed in this compound is roughly the double of the value reported for $CuSb_2O_6$, $\frac{\Delta}{k_B} \approx 34$ K[37].

5.2 Single crystal growth

Dr. Aaron Christian and Prof. John J. Neumeier provided us high quality samples. The single crystal growth process is described in the following. Polycrystalline $CoSb_2O_6$ were obtained using Co_3O_4 and Sb_2O_3, the latter one with additional excess of approximately 5%, to avoid the formation of $Co_7Sb_2O_{15}$. Starting materials were mixed, ground, pelletized, with the temperature profile: warm from 400°C to 1050°C at a rate of 50°C/day, for 3 days. In order to obtain single crystals, $CoSb_2O_6$ powder was placed in a quartz tube along with $TeCl_4$. The tube was evacuated before being sealed. The temperature was 220°C for 1h, then brought to 380°C at a rate of 50°C/h, and held at this temperature for 1 hour. Then, the temperature was increased to 930°C at a rate of 183°C/h and then held there for 200h. Then, the sample was cooled down to room temperature in 15h. Our sample is shown in Fig.5.1.

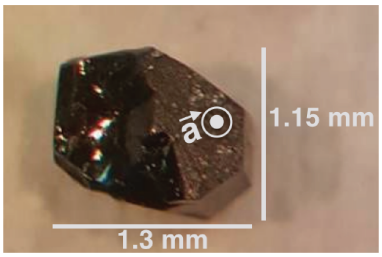

Fig. 5.1: $CoSb_2O_6$ single crystal obtained by the endothermic chemical vapor transport. The polished face is $\perp\vec{a}$.

5.3 Results - Raman scattering study

5.3.1 Vibrational normal modes

$CoSb_2O_6$ has a tetragonal trirutile structure of space group $P4_2/mnm$. The site symmetries for Co, Sb and O are 2a, 4e, 4f and 8j, the two latter belonging to oxygens. 54 Raman modes are expected. The factor group analysis presented in Tab.5.1 yields the following total irreducible representations:

$$\Gamma = 4A_{1g} + 2B_{1g} + 4B_{2g} + 6E_g \tag{5.1}$$

Polarization	Raman Active modes
-X(ZZ)X	A_{1g}
-X(YY)X	A_{1g}, B_{1g}
-X(ZY)X	E_g
-X(Z'Z')X	A_{1g}, B_{1g}, E_g
-X(Z'Y')X	A_{1g}, B_{1g}

Tab. 5.1: Polarization rules for $CoSb_2O_6$. In this notation, the laser propagation direction at the entrance is -X and at the exit is X. The polarizations are indicated inside the parenthesis, and the first indicated value is the polarization at the entrance, while the second is exit polarization. X$||\vec{a}$, Y$||\vec{b}$ e Z$||\vec{c}$, where $\vec{a}, \vec{b}$ and $\vec{c}$ are the lattice vectors. The polarizations X' and Y' indicate 45 ° rotation with respect to the original polarizations X and Y.

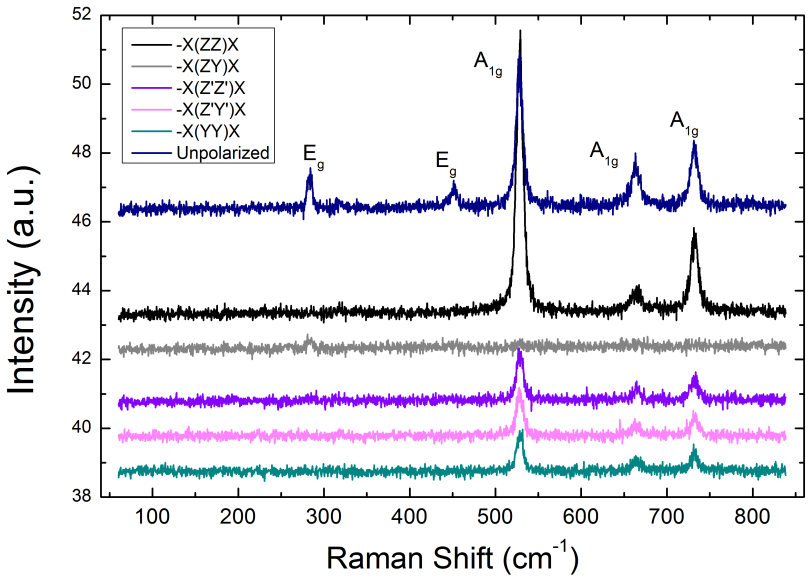

Fig. 5.2: Raman spectra of $CoSb_2O_6$ in different polarizations at room temperature.

Fig.5.2 displays Raman spectra in -X(ZZ)X, -X(ZY)X, -X(Z'Z')X, -X(Z'Y')X, -X(YY)X polarizations and unpolarized. We observed 5 modes at room temperature in the plane, YZ correspondent to the lattice plane $\overline{bc}$. Noticeably, in contrast to α-$CuSb_2O_6$, the modes assignment perfectly followed the factor group analysis, thus enforcing that twinning associated with

the structural phase transition in the previous compound introduced a small component of the A_{1g} modes in all previous spectra.

Since we observe similar spectra for both compounds due to their similar crystal structures, the calculations performed are valid for $CoSb_2O_6$ as well. A schematic representation of the additional vibrations that appear in the spectrum for this compound are shown in Figs.5.3 and Fig.5.4.

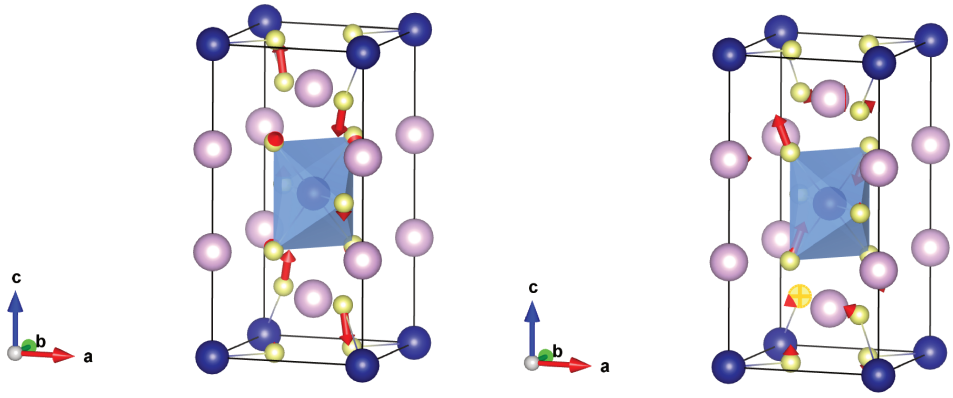

(a) ~ 450 cm^{-1} degenerate $E_g^{(1)}$ (b) ~ 450 cm^{-1} degenerate $E_g^{(2)}$

Fig. 5.3: Schematic representation of vibrations of the degenerate phonon mode E_g at ~ 450 cm^{-1} observed in the Raman spectra calculated within ab-initio lattice dynamical calculation [56].

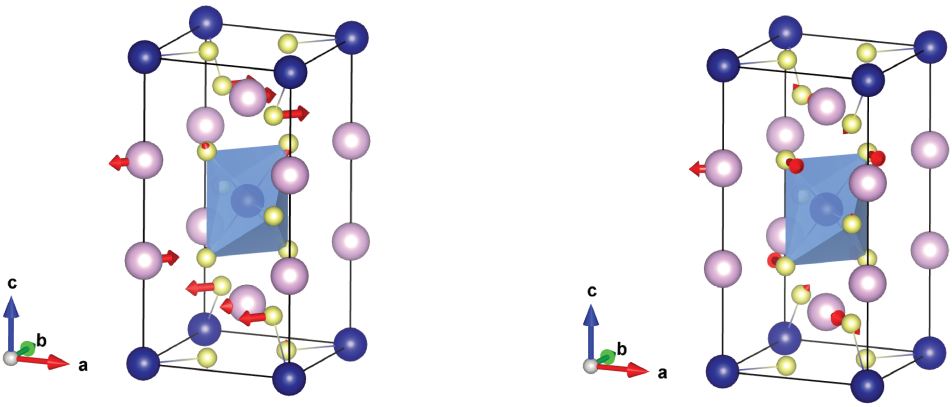

(a) ~ 280 cm^{-1} degenerate $E_g^{(1)}$ (b) ~ 280 cm^{-1} degenerate $E_g^{(2)}$

Fig. 5.4: Schematic representation of each vibration observed in the Raman spectra calculated within ab-initio lattice dynamical calculation [56] for the degenerate E_g phonon modes at ~ 280 cm^{-1}.

For both degenerate E_g mode at ~ 450 cm^{-1}, the in-plaquette oxygens vibrate in a bending mode. For the first mode depicted in Fig.5.4, the out-of-plaquette oxygens vibrate in opposite directions along $\vec{c}$.

The first degenerate E_g mode at ~ 280 cm^{-1}includes contributions of motions on the Sb ions, as well as a bending motion of the in-plaquette oxygens along the $\vec{c}$ direction. The second E_g degenerate mode at ~ 280 cm^{-1} also has contributions of Sb vibrations and a bending motion of in-plaquette oxygens parallel to the $(\overline{ab})$-plane.

5.3.2 Spin correlations investigation

In order to investigate the magnetic correlations, we took several spectra in different temperatures and they are being shown in Fig.5.5.

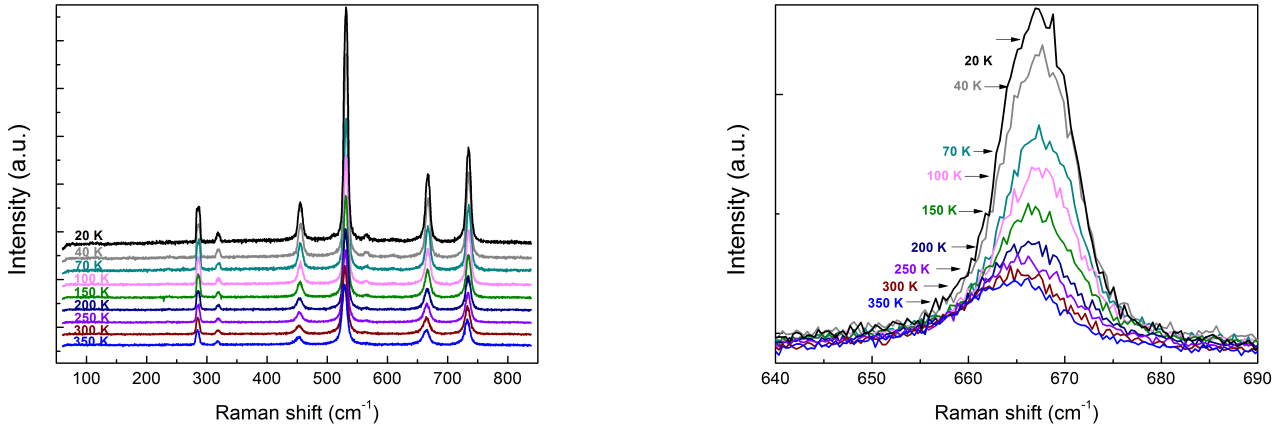

(a) (b)

Fig. 5.5: a) Several unpolarized Raman spectra taken for temperatures between 350 K and 20 K. b) Evolution of the peak at ~ 665 cm^{-1}.

With decreasing temperature, nearly all phonon modes become sharper and more intense. A noticeably shift in energy is detected, as depicted in Fig.4.11 b) for the mode at ~ 665 cm^{-1}. Additionally, at approximately 240 K, a new phonon mode at ~ 560 cm^{-1} is taking place.

Fig.5.6 shows the evolution of the phonon frequency, width and intensity dependence with temperature of the A_{1g} mode around 730 cm^{-1}. This phonon mode exhibits a hardening with decreasing temperature until approximately 80 K. The violet line is a fitting down to 80 K and extrapolated to lower temperatures considering the anharmonic decay of optical phonons processes from Eq.4.2. Upon further cooling from 80 K, a deviation from the anharmonic decay is manifested as a softening of approximately 0.5 cm^{-1}. The anomaly in the phonon frequency

is interpreted in terms of spin-phonon coupling. Moreover, the phonon becomes sharper and more intense with decreasing temperature.

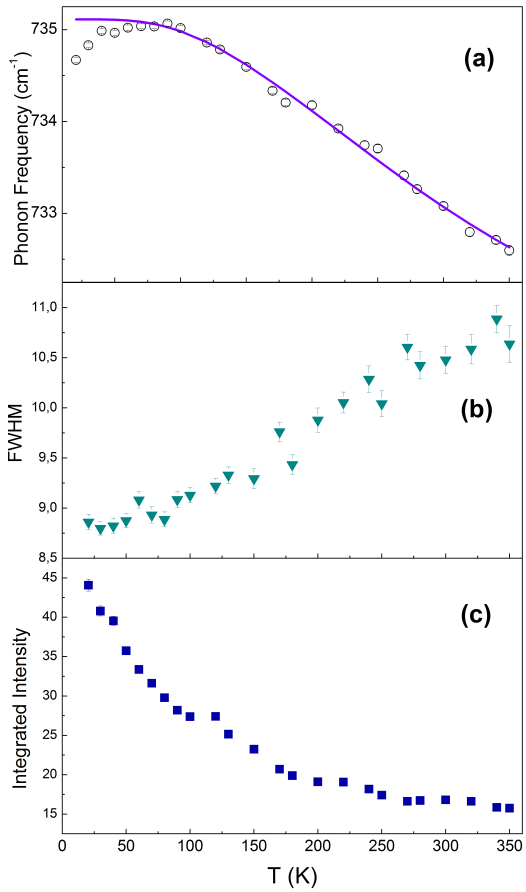

Fig. 5.6: Evolution of a) peak position b) phonon width and c) intensity for the phonon mode at ~ 730 cm^{-1}.

In Fig.5.7, the frequency, phonon width and integrated intensity of the A_{1g} mode around 665 cm^{-1} are plotted as a function of temperature. Upon cooling, this phonon mode undergo approximately 3 cm^{-1} of hardening in energy, and a deviation from the anharmonic decay takes place where the Curie law starts deviating. This is again interpreted in terms of a renormalization of the phonon energy due to spin-phonon coupling. The phonon width decreases and the intensity increases with decreasing temperature.

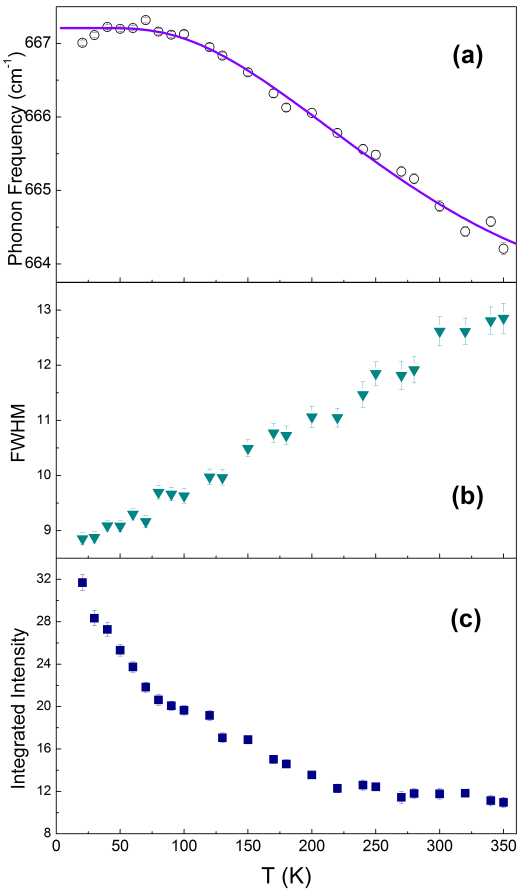

Fig. 5.7: Evolution of a) peak position b) phonon width and c) intensity for the phonon mode at ~ 665 cm^{-1}.

Fig.5.8 shows the temperature dependence of the phonon frequency, width and integrated intensity for the A_{1g} phonon mode at ~ 530 cm^{-1}. A hardening of approximately 2.6 cm^{-1}is taking place upon cooling from 350 K until 80 K. At 70 K, a softening associated with the spin-phonon coupling is taking place. The phonon width is increasing and the integrated intensity is decreasing with increasing temperature. In contrast to the correspondent phonon mode at ~ 515 cm^{-1} of compound $CuSb_2O_6$, notice that here we do not encounter any anomaly in the phonon width, neither this peak has a Fano line shape, neither it presents a softening in all the entire range of temperature.

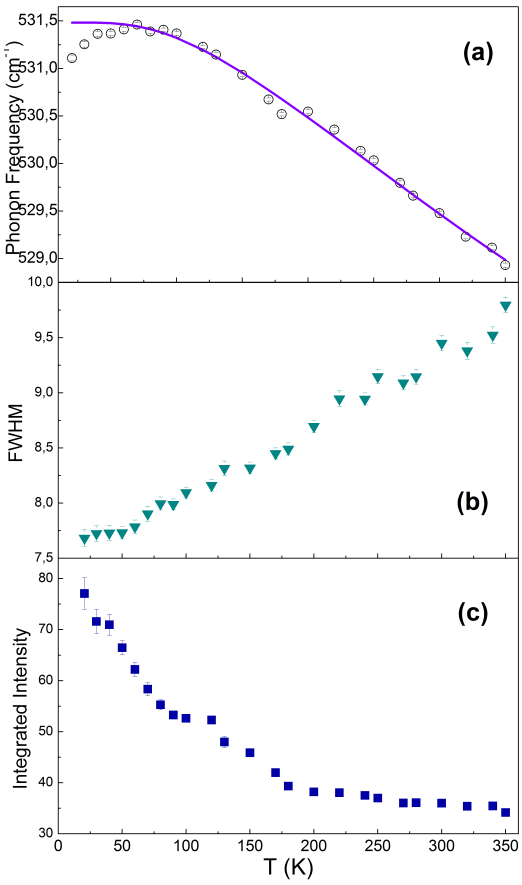

Fig. 5.8: Evolution of a) peak position b) phonon width and c) intensity for the phonon mode at ~ 530 cm^{-1}.

For the E_g phonon mode at ~ 450 cm^{-1}, depicted in Fig.5.9, the spin-phonon coupling below 80 K is extremely tiny, and even imperceptible. Again, the phonon broadening and decrease of intensity is taking place with increasing temperature.

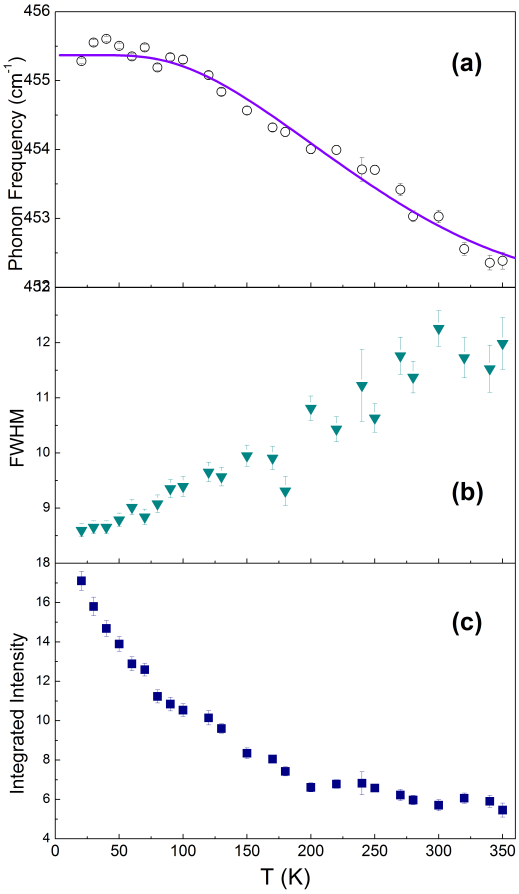

Fig. 5.9: Evolution of a) peak position b) phonon width and c) intensity for the phonon mode at ~ 450 cm^{-1}.

Upon cooling from 350 K to 80 K, the phonon mode at ~ 319 cm^{-1} undergo a hardening of approximately 1.5 cm^{-1}. Upon further cooling, it softens approximately 1 cm^{-1}. The phonon width is almost constant over the entire temperature range, and the intensity slightly increases with decreasing temperature, as it can be seen in Fig.5.10.

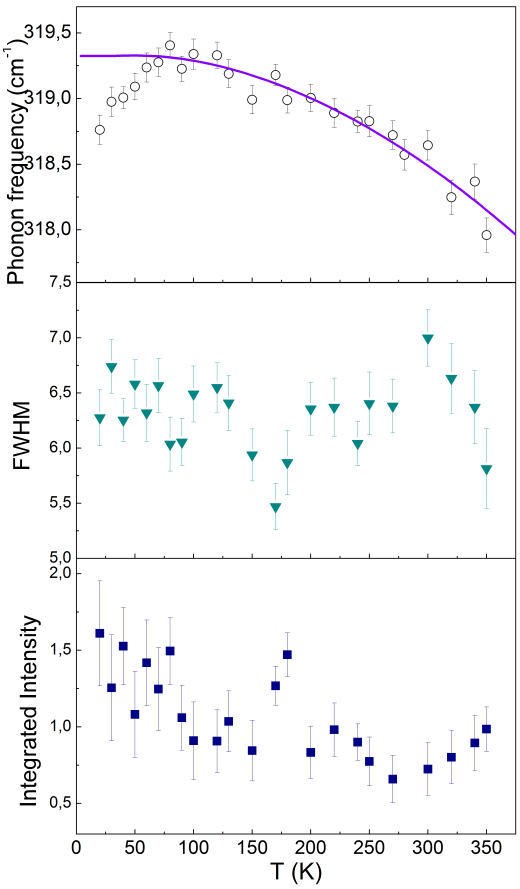

Fig. 5.10: Evolution of a) peak position b) phonon width and c) intensity for the phonon mode at ~ 319 cm^{-1}.

The E_g phonon mode at ~ 285 cm^{-1} is depicted in Fig.5.11 and it shows a hardening of about 1.5 cm^{-1} from 350 K down to 80 K, where it softens approximately 0.6 cm^{-1}. This deviation from the anharmonic decay is interpreted in terms of spin-phonon coupling. The phonon width and intensity are apparently showing a slight decrease with increasing temperature.

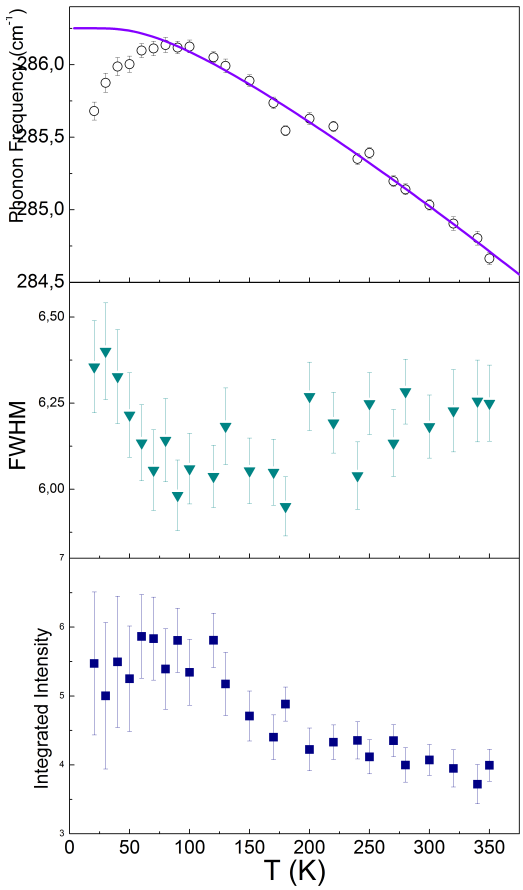

Fig. 5.11: Evolution of a) peak position b) phonon width and c) intensity for the phonon mode at ~ 285 cm^{-1}.

5.4 Discussion

It was possible to observe an anomalous softening for $T < 80$ K, which was attributed to spin-phonon coupling, since this temperature matches to the temperature where the Curie-Weiss law deviates to establish the low-dimensional AFM. Similarly to the case of $CuSb_2O_6$, there are softening for temperatures where the low-dimensional AFM behavior takes place for most observed phonon modes, but for $CoSb_2O_6$, there are no tiny jumps.

Fig.5.12 shows a comparison between the totally symmetric octahedra breathing mode for the compounds $CuSb_2O_6$ and $CoSb_2O_6$. Since the crystal structures for these compounds are very similar, this remarkably confirms that the anomaly observed in the case of the $CuSb_2O_6$ is entirely associated with the electronic structure, thus enforcing the possible scenario discussed in Section 4.4.

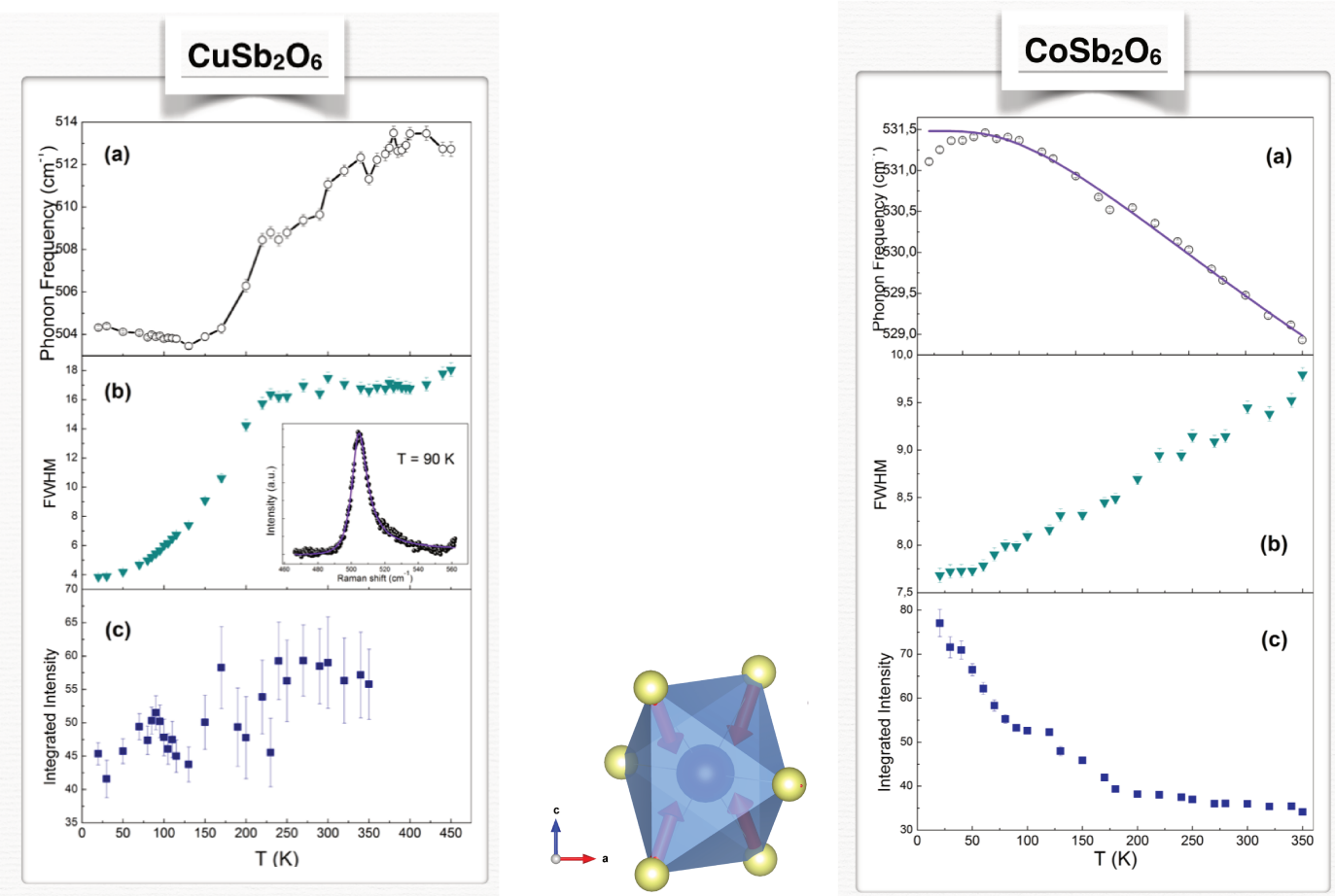

(a) (b) (c)

Fig. 5.12: a) Evolution of correspondent peaks at ~ 515 cm^{-1} for $CuSb_2O_6$ and c) ~ 530 cm^{-1} for $CoSb_2O_6$. b) Schematic representation of the vibrational mode.

5.5 Partial conclusions

To summarize, we have presented Raman scattering data of the low-dimensional spin-$\frac{3}{2}$ system $CoSb_2O_6$. Unambiguous identification regarding their magnetic properties has been challenging, and although a two-dimensional Ising like model has been proposed, the most acceptable one considers a spin-$\frac{3}{2}$ AFM chain. The nature of the transition to the ordered state at $T = 13.5$ K, has been also challenging, since a complete theoretical analysis regarding the existence of spin-Peierls transition in $S = \frac{3}{2}$ is still missing. However, qualitative arguments have been developed concerning its existence in this type of system, and it is believed that it is applicable to interpret the kink in $\chi(T)$. The driving force that leads to the one-dimensional behavior in this system remains unknown at present. Raman spectroscopy measurements in

this compound are reported here, and unlike $CuSb_2O_6$, it was possible to completely identify the symmetry of the modes via polarized Raman spectroscopy. No evidence of twinning neither bicrystallinity were detected with this technique. Furthermore, this compound does not present any structural transition, belonging to the tetragonal $P4_2/mnm$ space group over all the entire range of temperature. In addition, the temperature dependence of phononic excitations have showed a softening of some phonon modes for temperatures below 80 K, and since this temperature scales with the temperature where the one-dimensional behavior starts taking place, we have interpreted this anomaly in terms of a renormalization of the phonon energy via spin-phonon coupling. In addition, the previous anomaly observed in the width at $T \approx 240$ K for the correspondent phonon of $CuSb_2O_6$, was not apparent for $CoSb_2O_6$, evidencing their different electronic structure and magnetic behavior.

Chapter 6

Conclusions and Perspectives

This masters dissertation has addressed the study of low-dimensional spin systems using Raman spectroscopy. The main purpose of this work is to broaden and deepen the understanding of the spin correlations in low dimensional systems, exploring the effects of quantum magnetism. These systems can be characterized by their spin liquid ground state, exotic magnetic excitations and spin-phonon coupling. In particular, we have investigated the systems $M\mathrm{Sb_2O_6}$, M=(Cu, Co) with a spectroscopic technique which was capable of providing us local information about the magnetic correlations between first neighbors. The high sensitivity to spin and lattice dynamics through spin-phonon coupling, as well as its unprecedented energy resolution makes Raman spectroscopy an excellent probe for studying such systems. Finally, let us summarize the main results:

Spin-$\frac{1}{2}$ chain $CuSb_2O_6$

$\mathrm{CuSb_2O_6}$ can be well described as a one-dimensional antiferromagnet spin-$\frac{1}{2}$ Heisenberg chain. A theoretical work has proposed that the quasi one-dimensional behavior is being driven by an unusual orbital ordering. Raman spectra shows a structural transition from tetragonal $P4_2/mnm$ to monoclinic $P2_1/n$ as the emergence of a new phonon mode at ~ 670 cm^{-1} at $T_S = 397(3)$ K. This emergent phonon mode is associated to its neighboring phonon peak at $\sim$ 640 cm^{-1}, although they are not degenerate modes. In fact, lattice dynamical calculations have revealed that the phonon mode at $\sim$ 640 cm^{-1} includes a vibration of the out-of-plaquette oxygens against the ion Cu^{2+} in a breathing configuration. We suggest that this intriguing structural transition is associated with phonon modes which present the same type of vibration, but with central octahedra vibrating out-of-phase for neighboring unit cells for the emergent phonon mode at 670 cm^{-1}. This phonon mode would correspond to a mode at the border of the tetragonal Brillouin zone. In the monoclinic phase, this would become

zone-center and therefore would be Raman active due to a possible folding of the Brillouin zone associated with a doubling of the unit cell. In this way, we are indeed suggesting the presence of superstructure, which still has to be confirmed with X-ray diffraction. Additionally, it was possible to observe anomalies from the anharmonic decay of optical phonons at temperatures $T \approx 110$ K, whose energy scale is comparable to the low-dimensional exchange J. Thus, such anomalous behavior has been interpreted in terms of a renormalization of the phonon energy via spin-phonon coupling. Furthermore, it was possible to observe a phonon width anomaly at 240 K, which could not be attributed to spin-phonon coupling. This phonon has a Fano line shape, which suggests an interference between the phonon and electronic excitation. One possible excitation which might be occurring is an orbital flip, since this vibration involves a totally symmetric octahedra breathing mode configuration where the in-plaquette oxygens vibrate against the Cu^{2+} ion.

Spin-$\frac{3}{2}$ system $CoSb_2O_6$

Unambiguous identification regarding the magnetic properties of $CoSb_2O_6$ has been challenging. Although a two dimensional Ising like has been proposed for this compound, the one-dimensional spin-$\frac{3}{2}$ behavior revealed by anisotropic magnetocaloric effect is the most widely accepted nowadays. This compound does not present any structural transition, belonging to the tetragonal $P4_2/mnm$ space group, with similar crystal structure of α-$CuSb_2O_6$. At $T \approx 13.5$ K, a rapid drop in the magnetic susceptibility has been interpreted in terms of spin-Peierls transition, although a complete understanding of this kind of transition in $S = \frac{3}{2}$ systems has not emerged yet. Our temperature dependence of phononic excitations have shown softening of phonon modes at temperatures below 80 K, which has been interpreted in terms of spin-phonon coupling. Furthermore, we report different behavior for the correspondent phonon modes at ~ 515 cm^{-1} and ~ 530 cm^{-1} of $CuSb_2O_6$ and $CoSb_2O_6$, respectively. For the case of $CoSb_2O_6$, we did not observe the same frequency and width anomaly, which enforces its association with an unique electronic and phononic excitation interference for the previous studied compound. Thus, we could experimentally access the different electronic structures leading to different electronic excitations for these compounds.

Future Perspectives

In general, the structural transition is believed to be associated with an orbital ordering which is believed to be the driving force to the one-dimensional antiferromagnet behavior in $CuSb_2O_6$. Our suggested scenario includes the formation of superstructure in the lowest symmetry phase, which has to be confirmed with X-ray diffraction. In addition, for the same

compound, an intriguing behavior for the phonon mode at ~ 515 cm^{-1} has been interpreted in terms of a resonance between the phonon and an electronic excitation. One possibility for this excitation is an orbital flip, which could be also induced and investigated by the application of pressure. Our results elucidates the different nature of the electronic behavior for both compounds.

Furthermore, an investigation of the long-range ordered states at $T \approx 8$ K and $T \approx 13$ K for $CuSb_2O_6$ and $CoSb_2O_6$ is also a perspective.

Our results nicely demonstrate the viability of Raman spectroscopy to study low-dimensional spin antiferromagnets. By an analysis of the phonon frequency anomalies, one has direct access to the short-range spin-spin correlation $\langle S_i.S_j \rangle$, which is a quantity not easily obtainable by other experimental techniques. In this way, hopefully this work will motivate future works on novel low-dimensional spins systems.

Bibliography

[1] W. Lenz. Beitrag zum verständnis der magnetischen erscheinungen in festen körpern. *Physik. Zeitschr.*, XXI:613–615, 1920.

[2] H. Bethe. Zur theorie der metalle. *Zeitschrift für Physik*, 71(3):205–226, 1931.

[3] S. Thanos. Interpretation of experimental results of spin chains with weak interchain interaction. *Physica A: Statistical Mechanics and its Applications*, 378(2):273 – 282, 2007.

[4] H. J. Mikeska. Magnetic chains in solids. *Journal of Magnetism and Magnetic Materials*, 13(1):35 – 49, 1979.

[5] D. Kasinathan, K. Koepernik, and H. Rosner. Quasi-one-dimensional magnetism driven by unusual orbital ordering in $CuSb_2O_6$. *Phys. Rev. Lett.*, 100:237202, Jun 2008.

[6] A. Rebello, M. G. Smith, J. J. Neumeier, B. D. White, and Yi-Kuo Yu. Transition from one-dimensional antiferromagnetism to three-dimensional antiferromagnetic order in single-crystalline $CuSb_2O_6$. *Phys. Rev. B*, 87:224427, Jun 2013.

[7] J. Voit. One-dimensional fermi liquids. *Reports on Progress in Physics*, 58(9):977, 1995.

[8] M. Heinrich, H. A. Krug von Nidda, A. Krimmel, A. Loidl, R. M. Eremina, A. D. Ineev, B. I. Kochelaev, A. V. Prokofiev, and W. Assmus. Structural and magnetic properties of $CuSb_2O_6$ probed by ESR. *Phys. Rev. B*, 67:224418, Jun 2003.

[9] S.M. Eicher, J.E. Greedan, and K.J. Lushington. The magnetic properties of $FeTa_2O_6$. magnetic structure and low-dimensional behavior. *Journal of Solid State Chemistry*, 62(2):220 – 230, 1986.

[10] R.K. Kremer and J.E. Greedan. Magnetic ordering in $CoTa_2O_6$ and $NiTa_2O_6$. *Journal of Solid State Chemistry*, 73(2):579 – 582, 1988.

[11] B. Mason A. Bystrom, B. Hok. *Ark. Kemi Mineral. Geol.*, 15B:1, 1941.

[12] M. Herak, D. Žilić, D. Matković Čalogović, and H. Berger. Torque magnetometry study of magnetically ordered state and spin reorientation in the quasi-one-dimensional $S = \frac{1}{2}$ Heisenberg antiferromagnet $CuSb_2O_6$. *Phys. Rev. B*, 91:174436, May 2015.

[13] J. C. Bonner and M. E. Fisher. Linear magnetic chains with anisotropic coupling. *Phys. Rev.*, 135:A640–A658, Aug 1964.

[14] J.N. Reimers, J.E. Greedan, C.V. Stager, and R. Kremer. Crystal structure and magnetism in $CoSb_2O_6$ and $CoTa_2O_6$. *Journal of Solid State Chemistry*, 83(1):20 – 30, 1989.

[15] A. B. Christian, S. H. Masunaga, A. T. Schye, A. Rebello, J. J. Neumeier, and Yi-Kuo Yu. Magnetic field influence on the néel, dimer, and spin-liquid states of the low-dimensional antiferromagnets $NiTa_2O_6$ and $CoSb_2O_6$. *Phys. Rev. B*, 90:224423, Dec 2014.

[16] Stephen Blundell. *Magnetism in Condensed Matter (Oxford Master Series in Physics)*. Oxford University Press, USA, 1 edition, December 2001.

[17] N.W. Ashcroft and N.D. Mermin. *Solid State Physics*. Cengage Learning, 2011.

[18] G. E. Kimball. Directed valence. *The Journal of Chemical Physics*, 8(2):188–198, 1940.

[19] H. A. Jahn and E. Teller. Stability of polyatomic molecules in degenerate electronic states. i. orbital degeneracy. In *Proceedings of the Royal Society of London A: Mathematical, Physical and Engineering Sciences*, volume 161, pages 220–235. The Royal Society, 1937.

[20] J. Hubbard. Electron correlations in narrow energy bands. In *Proceedings of the royal society of london a: mathematical, physical and engineering sciences*, volume 276, pages 238–257. The Royal Society, 1963.

[21] J. Hubbard. Electron correlations in narrow energy bands. ii. the degenerate band case. In *Proceedings of the Royal Society of London A: Mathematical, Physical and Engineering Sciences*, volume 277, pages 237–259. The Royal Society, 1964.

[22] J. Hubbard. Electron correlations in narrow energy bands. iii. an improved solution. In *Proceedings of the Royal Society of London A: Mathematical, Physical and Engineering Sciences*, volume 281, pages 401–419. The Royal Society, 1964.

[23] J. Hubbard. Electron correlations in narrow energy bands. iv. the atomic representation. In *Proceedings of the Royal Society of London A: Mathematical, Physical and Engineering Sciences*, volume 285, pages 542–560. The Royal Society, 1965.

[24] J. Hubbard. Electron correlations in narrow energy bands. v. a perturbation expansion about the atomic limit. In *Proceedings of the Royal Society of London A: Mathematical, Physical and Engineering Sciences*, volume 296, pages 82–99. The Royal Society, 1967.

[25] J. Hubbard. Electron correlations in narrow energy bands. vi. the connexion with many-body perturbation theory. In *Proceedings of the Royal Society of London A: Mathematical, Physical and Engineering Sciences*, volume 296, pages 100–112. The Royal Society, 1967.

[26] M. Born and R. Oppenheimer. Zur quantentheorie der molekeln. *Annalen der Physik*, 389(20):457–484, 1927.

[27] P. W. Anderson. New approach to the theory of superexchange interactions. *Phys. Rev.*, 115:2–13, Jul 1959.

[28] N. D. Mermin and H. Wagner. Absence of ferromagnetism or antiferromagnetism in one- or two-dimensional isotropic Heisenberg models. *Phys. Rev. Lett.*, 17:1133–1136, Nov 1966.

[29] E. J. Neves and J. F. Perez. Long range order in the ground state of two-dimensional antiferromagnets. *Physics Letters A*, 114(6):331 – 333, 1986.

[30] I. Affleck, D. Gepner, H. J. Schulz, and T. Ziman. Critical behavior of spin-S Heisenberg antiferromagnetic chains: analytic and numerical results. *Journal of Physics A: Mathematical and General*, 22(5):511, 1989.

[31] F. J. Dyson, E. H. Lieb, and B. Simon. *Phase Transitions in Quantum Spin Systems with Isotropic and Nonisotropic Interactions*, pages 163–211. Springer Berlin Heidelberg, Berlin, Heidelberg, 2004.

[32] T. Giamarchi. *Quantum Physics in One Dimension*. International Series of Monographs on Physics. Clarendon Press, 2003.

[33] E. Lieb, T. Schultz, and D. Mattis. Two soluble models of an antiferromagnetic chain. *Annals of Physics*, 16(3):407–466, 1961.

[34] J. des Cloizeaux and J. J. Pearson. Spin-wave spectrum of the antiferromagnetic linear chain. *Phys. Rev.*, 128:2131–2135, Dec 1962.

[35] F. D. M. Haldane. Nonlinear field theory of large-spin Heisenberg antiferromagnets: semiclassically quantized solitons of the one-dimensional easy-axis néel state. *Physical Review Letters*, 50(15):1153, 1983.

[36] E. Pytte. Peierls instability in Heisenberg chains. *Phys. Rev. B*, 10:4637–4642, Dec 1974.

[37] A. B. Christian, A. Rebello, M. G. Smith, and J. J. Neumeier. Local and long-range magnetic order of the spin $-\frac{3}{2}$ system $CoSb_2O_6$. *Phys. Rev. B*, 92:174425, Nov 2015.

[38] M. T. Dove. *Structure and dynamics: an atomic view of materials*, volume 1. Oxford University Press, 2003.

[39] E. K. U. Gross, J. F. Dobson, and M. Petersilka. *Density functional theory of time-dependent phenomena*, pages 81–172. Springer Berlin Heidelberg, Berlin, Heidelberg, 1996.

[40] P. Hohenberg and W. Kohn. Inhomogeneous electron gas. *Phys. Rev.*, 136:B864–B871, Nov 1964.

[41] W. Kohn and L. J. Sham. Self-consistent equations including exchange and correlation effects. *Phys. Rev.*, 140:A1133–A1138, Nov 1965.

[42] D. R. Hartree. The wave mechanics of an atom with a non-coulomb central field. part i. theory and methods. In *Mathematical Proceedings of the Cambridge Philosophical Society*, volume 24, pages 89–110. Cambridge Univ Press, 1928.

[43] R. O. Jones and O. Gunnarsson. The density functional formalism, its applications and prospects. *Rev. Mod. Phys.*, 61:689–746, Jul 1989.

[44] J. P. Perdew and Y. Wang. Accurate and simple analytic representation of the electron-gas correlation energy. *Phys. Rev. B*, 45:13244–13249, Jun 1992.

[45] J. R. Ferraro. *Introductory Raman spectroscopy*. Academic press, 2003.

[46] M. V. Klein and M. Cardona. Light scattering in solids. *Topics in Applied Physics*, 8:148, 1975.

[47] E. Granado. Estudos de propriedades ópticas e magnéticas de manganitas., 2000.

[48] Baltensp. W. and J. S. Helman. Influence of magnetic order in insulators on optical phonon frequency. *Helvetica physica acta*, 41(6-7):668, 1968.

[49] A. V. Prokofiev, F. Ritter, W. Assmus, B. J. Gibson, and R. K. Kremer. Crystal growth and characterization of the magnetic properties of $CuSb_2O_6$. *Journal of crystal growth*, 247(3):457–466, 2003.

[50] E. M. da Silva Wheeler. *Neutron Scattering from Low-Dimensional Quantum Magnets*. 2007.

[51] A. Nakua, H. Yun, J.N. Reimers, J.E. Greedan, and C.V. Stager. Crystal structure, short range and long range magnetic ordering in $CuSb_2O_6$. *Journal of Solid State Chemistry*, 91(1):105–112, 1991.

[52] A.M. Nakua and J.E. Greedan. Confirmation of long-range magnetic order in $CuSb_2O_6$. *Journal of Solid State Chemistry*, 118(1):199–201, 1995.

[53] M. Kato, A. Hatazaki, K. Yoshimura, and K. Kosuge. One-dimensional magnetic behavior of $CuSb_2O_6$. *Physica B: Condensed Matter*, 281:663–664, 2000.

[54] B.J. Gibson, R.K. Kremer, A.V. Prokofiev, W. Assmus, and B. Ouladdiaf. Elastic neutron diffraction study of long-range antiferromagnetic order in the S=$\frac{1}{2}$ quantum chain system $CuSb_2O_6$. *Journal of Magnetism and Magnetic Materials*, 272-276, Part 2:927–928, 2004. Proceedings of the International Conference on Magnetism (ICM 2003).

[55] V. I. Torgashev, V. B. Shirokov, A. S. Prokhorov, B. Gorshunov, P. Haas, M. Dressel, B. J. Gibson, R. K. Kremer, A. V. Prokofiev, and W. Assmus. Polar phonons in the antiferromagnetic $s = \frac{1}{2}$ spin-chain system $CuSb_2O_6$. *Phys. Rev. B*, 67:134433, Apr 2003.

[56] P. Giannozzi et al. Quantum espresso: a modular and open-source software project for quantum simulations of materials. *Journal of Physics: Condensed Matter*, 21(39):395502 (19pp), 2009.

[57] E. O. Giere, A. Brahimi, H. J. Deiseroth, and D. Reinen. The geometry and electronic structure of the Cu^{2+} polyhedra in trirutile-type compounds $Zn(Mg)_{1-x}Cu_xSb_2O_6$ and the dimorphism of $CuSb_2O_6$: a solid state and EPR study. *Journal of solid state chemistry*, 131(2):263–274, 1997.

[58] M. Balkanski, R. F. Wallis, and E. Haro. Anharmonic effects in light scattering due to optical phonons in Silicon. *Phys. Rev. B*, 28:1928–1934, Aug 1983.

[59] J. W. Ager III, W. Walukiewicz, M. McCluskey, M. A. Plano, and M. I. Landstrass. Fano interference of the raman phonon in heavily boron-doped diamond films grown by chemical vapor deposition. *Applied Physics Letters*, 66(5):616–618, 1995.

[60] C. R. Michel, A. H. Martínez, and S. Jiménez. Gas sensing response of nanostructured trirutile-type $CoSb_2O_6$ synthesized by solution-polymerization method. *Sensors and Actuators B: Chemical*, 132(1):45–51, 2008.

[61] D. Guo, T. Kennedy, and S. Mazumdar. Spin-Peierls transitions in S $> \frac{1}{2}$ Heisenberg chains. *Phys. Rev. B*, 41:9592–9595, May 1990.

Appendix A

Raman Tensors and Selection Rules

$P4_2/mnm$

The active polarizability Raman tensors for the tetragonal crystal structure with space group $P4_2/mnm$ are given by:

$$A_{1g} = \begin{bmatrix} a & 0 & 0 \\ 0 & a & 0 \\ 0 & 0 & b \end{bmatrix} B_{1g} = \begin{bmatrix} c & 0 & 0 \\ 0 & -c & 0 \\ 0 & 0 & 0 \end{bmatrix} B_{2g} = \begin{bmatrix} 0 & d & 0 \\ d & 0 & 0 \\ 0 & 0 & 0 \end{bmatrix} E_g^{(1)} = \begin{bmatrix} 0 & 0 & 0 \\ 0 & 0 & e \\ 0 & e & 0 \end{bmatrix} E_g^{(2)} = \begin{bmatrix} 0 & 0 & -e \\ 0 & 0 & 0 \\ -e & 0 & 0 \end{bmatrix}$$

The polarization selection rules given by Eq.3.9 are calculated by multiplying incoming light polarization times the Raman tensor times the out coming light polarization, as depicted in Fig.A.1.

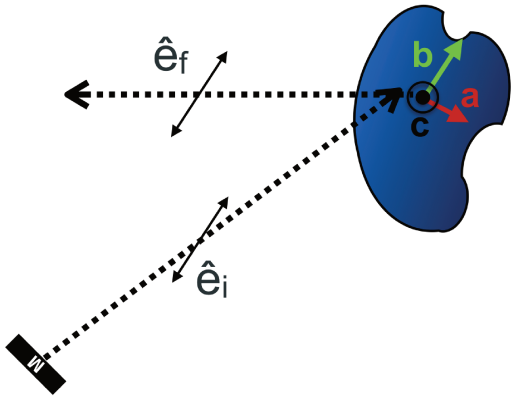

Fig. A.1: Schematic representation of the parallel polarization -Z(YY)Z. The Poyinting vector is along the Z (or approximately $\vec{c}$ crystallographic direction) and the incoming and outcoming polarizations are along the $\vec{b}$ crystallographic direction.

For example, for the polarization $-Z(XX)Z$, the A_{1g} mode is active:

$$\begin{bmatrix} 1 & 0 & 0 \end{bmatrix} \begin{bmatrix} a & 0 & 0 \\ 0 & a & 0 \\ 0 & 0 & b \end{bmatrix} \begin{bmatrix} 1 \\ 0 \\ 0 \end{bmatrix} = a$$

In contrast, the $E_g^{(1)}$ mode is forbidden:

$$\begin{bmatrix} 1 & 0 & 0 \end{bmatrix} \begin{bmatrix} 0 & 0 & 0 \\ 0 & 0 & e \\ 0 & e & 0 \end{bmatrix} \begin{bmatrix} 1 \\ 0 \\ 0 \end{bmatrix} = 0$$

Therefore, by performing the matrices calculations, one can arrive at the selection rules showed in Tab.4.2 and Tab.5.1.